DENSITY- AND TEMPERATURE-DEPENDENCE OF THE STATIC AND THE DYNAMIC STRUCTURE FACTOR IN LIQUID ARGON MEASURED BY THERMAL NEUTRON SCATTERING

PROEFSCHRIFT

TER VERKRIJGING VAN DE GRAAD VAN DOCTOR IN DE TECHNISCHE WETENSCHAPPEN AAN DE TECHNISCHE HOGESCHOOL DELFT, OP GEZAG VAN DE RECTOR MAGNIFICUS, PROF. DR. J.M. DIRKEN, IN HET OPENBAAR TE VERDEDIGEN TEN OVERSTAAN VAN HET COLLEGE VAN DEKANEN OP 9 MEI 1985 TE 16.00 UUR

DOOR

PETER VERKERK

geboren te Neustadt an der Weinstrasse,
doctorandus in de wiskunde en natuurwetenschappen

BIBLIOTHEEK TECHNISCHE UNIVERSITEIT
Prometheusplein 1
DELFT

1985

Offsetdrukkerij Kanters B.V.,
Alblasserdam

TR diss
1435

Dit proefschrift is goedgekeurd door de promotoren:

PROF. DR. IR. L.A. DE GRAAF
PROF. DR. J.J. VAN LOEF

voor Margreet

Contents

1. Introduction	5
2. Summary of theory	9
3. Experimental set-up	13
3.1. Spectrometer	13
3.2. Sample	15
3.3. Measurements	18
4. Corrections	23
4.1. Calibration	24
4.2. Correction of the argon measurements for container scattering	25
4.3. Multiple scattering	25
4.4. Deconvolution	31
5. Results	32
6. Analysis of the 844-bar data	48
7. Density- and temperature-dependence of S(k) and S(k,ω)	56
7.1. Density dependence	56
7.1.1. Density derivatives of S(k)	56
7.1.2. Density derivative of S(k,ω)	63
7.2. Temperature dependence	66
8. Conlusions	71
Appendix A	73
Appendix B	76
Appendix C	77
References	79
Paper I: High pressure sample container for thermal neutron spectroscopy and diffraction on strongly scattering fluids	83
Paper II: Calculation of the dynamic structure factor from thermal-neutron time-of-flight spectra	92
Paper III: Resolution correction: a simple and efficient algorithm with error analysis	119
Samenvatting	140

1. Introduction

To cope with the intractable large number of degrees of freedom of an N-particle system (N is of the order of 10^{23}), it is very convenient to describe the structure and dynamics in terms of static and time-dependent correlation functions. For instance the density-density correlation function describes density fluctuations on a microscopic scale but also yields the thermodynamics and transport coefficients.

X-ray and thermal-neutron scattering provide a probe to study experimentally the static density-density correlation function, because the wavelength of the photons and of thermal neutrons is of the order of interparticle distances in dense systems (gases at high densities, liquids, solids, glasses). The study of the time-dependent correlation functions requires a probe that can measure energy transfers of the order of the thermal energy of the particles of the system, which is usually in the meV-range. Hot, thermal and cold neutrons meet these requirements and the energy transfer in neutron scattering is relatively large and can easily be measured. Light also has the required energy, but since the wavelength is large compared to interparticle distances (except in very low density gases), light scattering provides information on the dynamics in the hydrodynamic regime. When using X-rays to study the dynamics, extreme resolution is required (of the order 10^{-6}), which might be reached with the next generation of synchrotrons in combination with perfect monochromators.

Additional advantages of neutrons are: the absence of an electrical charge, the neutrons are being scattered by the nuclei, the scattering is spin dependent and different for different isotopes, and neutrons penetrate easily the walls of the sample containment and cryostat. An important disadvantage is the relatively low intensity of the presently available neutron sources, even so at large installations as nuclear reactors or particle accelerators.

In recent years our understanding of the dynamics on a microscopic scale in simple (i.e. without internal degrees of freedom) fluids has increased considerably thanks to the combined efforts of neutron scattering experiments, theoretical studies and computer simulations. Nevertheless, several problems have not yet fully been solved, such as the dependence of the dynamics on the shape of the potential, the origin of collective motions at short wavelength, and the existence of a metastable state in super-cooled liquids.

Because the dynamics depends upon the interparticle potential, knowledge of the potential is necessary to understand the dynamics. Among the simple liquids, that can be used for neutron scattering experiments, the rare gases have the best known interaction potential: the two-particle interaction potential is known very accurately and the three-particle potential, the influence of which can certainly not be neglected in dense gases and liquids, is fairly

well known [1]. On the other hand the two-particle potential for liquid metals is known less accurately and the three-particle potential not at all. Nevertheless much attention has recently been paid to liquid metals, partly because the shape of the two-particle potential differs considerably from the one in noble gases and partly because collective density fluctuations have been found at a much shorter wavelength than in liquefied noble gases. However, recently the existence of collective density fluctuations at wavelengths at least as short as in liquid metals has been demonstrated experimentally in liquid argon [2].

From the aforegoing it follows that neutron scattering experiments on noble gases at high density are of interest. The relevant information about the dynamics is hidden in subtle details of the shape of the spectrum of scattered neutrons; hence the neutron scattering measurements must be carried out with the utmost care and all instrumental effects must be properly accounted for, so that highly accurate data result. After the successful experiments of Sköld et al. in 1972 on liquid argon near the triple point [3], a few more inelastic neutron scattering measurements on rare gases have been reported. Postol and Pelizzari [4] performed an experiment on argon at room temperature and 456 bar (particle number density ρ=10.1 nm^{-3}), Groome et al. [5] measured xenon at room temperature and several pressures between 52 and 73 bar (ρ=1.85 - 4.58 nm^{-3}) and Egelstaff et al. [6] measured krypton at room temperature and 12 pressures between 181 and 942 bar (ρ=6 - 14 nm^{-3}). The only data in the liquid state are for neon by Buyers et al. [7] at 26.9 K and vapour pressure (ρ=36.1 nm^{-3}) and by Bell et al. [8] who measured at several conditions in the liquid and gaseous state (T = 26.5 - 70 K, ρ = 10.1 - 35.8 nm^{-3}). Bell et al. focus their attention on the transition towards the hydrodynamic regime. The work on helium is not included in this list.

In this thesis are presented the results of inelastic thermal neutron scattering measurements on liquid ^{36}Ar at 120 K and three pressures: 19.5, 267 and 844 bar (corresponding to particle number densities of 17.6, 19.5 and 21.6 nm^{-3}) (see fig.1). The experiments were performed with a rotating-crystal spectrometer at the 2 MW swimming-pool reactor of our institute. The purpose of the measurements was to obtain not only dynamic structure factors but their density dependence as well. Preliminary results are given by Verkerk [9]. Note that the highest of the three densities is approximately equal to the triple-point density (21.3 nm^{-3}) (fig.1). Thus not only the density dependence of the dynamic structure factor along the 120 K-isotherm is measured, but also the temperature dependence along an isochore by combining the present results at 844 bar with the data by Sköld et al. [3]. The temperature dependence of the static structure factor can be determined from the combination of the present results with the diffraction data by Yarnell et al. [10] on liquid argon near the triple point. The isothermal density derivative of the

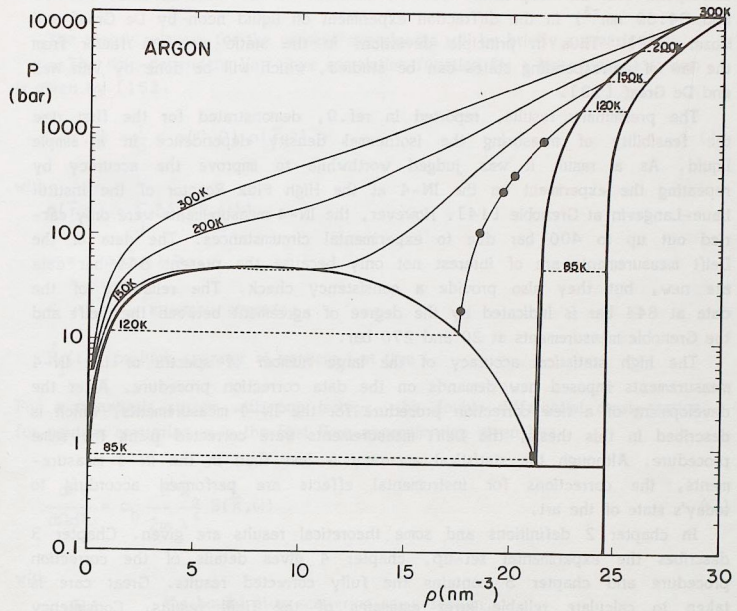

Fig.1. Isotherms of fluid argon at a few temperatures. The vapour-liquid, the liquid-solid and the vapour-solid coexistence regions are indicated. Note that the vertical axis has a logarithmic scale. The five dots indicate the thermodynamic states of the experiments performed on the RKS-1 in Delft and on the IN-4 at the ILL, the square represents the experiment by Sköld et al. [3].

two-point density correlation function is related to the three-point density correlation function, whereas the temperature derivative at constant density is related to the density-density-energy correlation function [11]. Both derivatives provide additional tests for liquid state theories. A different approach is also possible: if the temperature is increased (at constant density) the repulsive part of the interaction potential becomes relatively more important. Thus one obtains information on the influence of the shape of the potential on the dynamics. Varying the density may provide information for instance on the importance of correlated collisions in hard-spheres theories.

Furthermore the temperature and the two lower densities have been chosen to

correspond with the temperature (35 K) and two of the three densities (31.69 and 34.69 nm^{-3}) in the diffraction experiment on liquid neon by De Graaf and Mozer [12]. Thus in principle deviations in the static structure factor from the law of corresponding states can be studied, which will be done by Van Well and De Graaf [13].

The preliminary results, reported in ref.9, demonstrated for the first time the feasibility of measuring the isothermal density dependence in a simple liquid. As a result it was judged worthwhile to improve the accuracy by repeating the experiment on the IN-4 at the High Flux Reactor of the Institut Laue-Langevin at Grenoble [14]. However, the IN-4 measurements were only carried out up to 400 bar due to experimental circumstances. The data of the Delft measurements are of interest not only because the present 844 bar data are new, but they also provide a consistency check. The reliability of the data at 844 bar is indicated by the degree of agreement between the Delft and the Grenoble measurements at 20 and 270 bar.

The high statistical accuracy of the large number of spectra of the IN-4 measurements imposed new demands on the data correction procedure. After the development of a new correction procedure for the IN-4 measurements, which is described in this thesis, the Delft measurements were corrected using the same procedure. Although the statistical accuracy is less than in the IN-4 measurements, the corrections for instrumental effects are performed according to today's state of the art.

In chapter 2 definitions and some theoretical results are given. Chapter 3 describes the experimental set-up, chapter 4 gives details of the correction procedure and chapter 5 contains the fully corrected results. Great care is taken to calculate reliable error estimates of the final results. Consistency with rigorous theoretical results and with the IN-4 measurements is checked. In chapter 6 the experimental data at 844 bar are being analysed and chapter 7 treats the density and temperature dependence of the dynamic structure factor. Chapter 8 contains final conclusions. Three previously published papers are part of this thesis. The first paper gives details of the high pressure sample container used in the measurements, the second one deals with the data correction procedure, and the third one presents the method of resolution correction used in the data analysis.

2. Summary of theory

The theory relevant for the present experiments will be briefly summarized:

The time-dependent Van Hove correlation function for a homogeneous system is given by [15]:

$$G(\vec{r},t) = \frac{1}{\rho} < \rho(0,0)\ \rho(\vec{r},t) > , \qquad (1)$$

with

$$\rho(\vec{r},t) = \sum_j \delta(\vec{r} - \vec{R}_j(t)) ,$$

$$\rho = < \rho(\vec{r},t) > ,$$

$< \ldots >$: ensemble average,

$\vec{R}_j(t)$: position operator of particle j at time t.

For a monatomic system with one isotope, the double differential cross-section for neutron scattering is in the first Born approximation given by:

$$\frac{d^2\sigma}{d\Omega d\lambda} = \sigma_b \frac{h}{2m} \frac{\lambda}{\lambda_0^4} S(\vec{k},\omega) . \qquad (2)$$

with

σ_b: the bound atom scattering cross-section,
h: Planck's constant,
m: the neutron mass,
λ_0: wavelength of the incident neutrons,
λ: wavelength of the scattered neutrons,
Ω: solid angle into which the neutrons are scattered,
$S(\vec{k},\omega)$: the dynamic structure factor, defined by:

$$S(\vec{k},\omega) = \frac{1}{2\pi} \int_{-\infty}^{\infty} dt \int_V d\vec{r}\ G(\vec{r},t)\ \exp i(\vec{k}\cdot\vec{r} - \omega t) , \qquad (3)$$

with

$\hbar\vec{k}$: the momentum transfer and
$\hbar\omega$: the energy transfer from the neutron to the sample in the scattering event ($\hbar = h/2\pi$),
V: volume of the sample.

In the remainder of this paper we will be concerned only with isotropic systems: $S(\vec{k},\omega) = S(k,\omega)$ and $G(\vec{r},t) = G(r,t)$ with $k = |\vec{k}|$ and $r = |\vec{r}|$.

For three limiting cases $S(k,\omega)$ or $G(r,t)$ can be calculated exactly:

(1) If k becomes very large, density fluctuations of very short wavelength $\lambda = 2\pi/k$ are being observed and if λ becomes small compared to the distances between the particles, the interaction potential plays no role and $S(k,\omega)$ is given by the free-gas expression:

$$\lim_{k\to\infty} S(k,\omega) = S_f(k,\omega) = \frac{1}{k}\left\{\frac{M}{2\pi k_B T}\right\}^{\frac{1}{2}} \exp\left\{-\frac{M}{2k_B T k^2}\left(\omega - \frac{\hbar k^2}{2M}\right)^2\right\} \quad (4)$$

with M : the particle mass,
k_B: Boltzmann's constant,
T : the temperature of the sample.

(2) If the wavelength of the density fluctuations is large compared to the interparticle distances, the continuum approximation applies and linearized hydrodynamics yields the well known Landau-Placzek triplet:

$$\lim_{k\to o} S(k,\omega) = S_h(k,\omega) = \frac{S(k)}{\pi\gamma}\left\{(\gamma-1)\frac{ak^2}{\omega^2+(ak^2)^2} + \tfrac{1}{2}\frac{\Gamma_s k^2+(\omega+c_s k)b_s k}{(\omega+c_s k)^2+(\Gamma_s k^2)^2} + \tfrac{1}{2}\frac{\Gamma_s k^2-(\omega-c_s k)b_s k}{(\omega-c_s k)^2+(\Gamma_s k^2)^2}\right\} \quad (5)$$

with $S(k)$: the static structure factor defined by $S(k) = \int_{-\infty}^{\infty} S(k,\omega)d\omega$,
$\gamma = C_p/C_v$, the ratio of the specific heats,
$a = \lambda/(\rho C_p)$, thermal diffusivity,
λ: thermal conductivity,
Γ_s: sound damping factor,
c_s: adiabatic speed of sound,
$b_s = [(\gamma-1)a+\Gamma_s]/c_s$.

With neutron scattering one observes density fluctuations with a wavelength between these two limits.

(3) The intermediate scattering function $F(k,t)$, defined as

$$F(k,t) = \int_V d\vec{r}\, \exp(i\vec{k}\cdot\vec{r})\, G(r,t) = \int_{-\infty}^{\infty} dt\, \exp(i\omega t)\, S(k,\omega)$$

can be expanded in a Taylor series at t=o and the coefficients are given by the frequency moments of $S(k,\omega)$. A few lower order moments can be calculated and they determine the short time behaviour of $F(k,t)$ (or $G(r,t)$):

$$\begin{aligned}
\langle\omega^n\rangle &= \int_{-\infty}^{\infty} \omega^n S(k,\omega)d\omega \ , \\
\langle\omega^0\rangle &= S(k) \ , \\
\langle\omega\rangle &= \omega_R = \hbar k^2/2M \ , \\
\langle\omega^2\rangle &= \frac{k_B T}{M} k^2 + O(\hbar^2) \ ,
\end{aligned} \quad (6)$$

with $\hbar\omega_R$ the recoil energy. For a system with an additive two-particle potential $\varphi(r)$, the third [16] and fourth [17] moment are given by:

$$\begin{aligned}
\langle\omega^3\rangle &= \omega_R\left\{\omega_R(\omega_R+4\omega_K)+\Omega^2(k)\right\} \ , \\
\langle\omega^4\rangle &= \langle\omega^2\rangle\left\{3\langle\omega^2\rangle+\Omega^2(k)\right\}+O(\hbar^2) \ .
\end{aligned} \quad (7)$$

$\hbar\omega_K$ is the average kinetic energy per particle and

$$\Omega^2(k) = \frac{\rho}{M}\int (1-\cos kz)\frac{d^2\varphi(r)}{dz^2} g(r)\, d\vec{r} \ .$$

The three limiting cases mentioned are theoretically exactly known, but for arbitrary values of k and t only approximate theories exist.

The isothermal density derivative of Van Hove's correlation function is given by [11]:

$$\chi_T\left[\frac{\partial}{\partial\rho}\left\{\rho G(r,t)\right\}\right]_T = \frac{1}{k_B T}\int d\vec{r}\,'\left[\frac{\langle\rho(\vec{o},o)\rho(\vec{r},t)\rho(\vec{r}\,',t')\rangle}{\rho^2} - G(\vec{r},t)\right] , \quad (8)$$

with $\chi_T = \frac{1}{\rho}\left[\frac{\partial\rho}{\partial P}\right]_T$ the isothermal compressibility.

The temperature derivative at constant density is given by [11]:

$$k_B T^2 \left[\frac{\partial G(r,t)}{\partial T} \right]_\rho$$

$$= \int d\vec{r}' \left[\frac{\langle \rho(\vec{0},0)\rho(\vec{r},t)u(\vec{r}',t')\rangle}{\rho^2} - \langle u \rangle G(r,t) \right]$$

$$- \chi_T k_B T \left[\frac{\partial \langle u \rangle}{\partial \rho} \right]_T \left[\frac{\partial}{\partial \rho} \left\{ \rho G(r,t) \right\} \right]_T \qquad (9)$$

with $u(\vec{r},t) = \sum_{i=1}^{N} \frac{p_i^2}{2M} \delta(\vec{r}-\vec{R}_i(t)) + \frac{1}{2} \sum_{\substack{i=1 \\ j \neq i}}^{N} \varphi(R_{ij}) \delta(\vec{r}-\vec{R}_i(t))$,

$\vec{p}_i$: the momentum of particle i at time t,

$\langle u \rangle$: the internal energy density.

Note that eqs.8 and 9 do not provide a means to determine experimentally the triplet correlation functions, but models of the triplet correlation function can be tested against the experimental data.

All the sophisticated theories, which have recently been applied to simple liquids, are purely classical (with the exception of theories specifically developed for helium). Eqs.(8) and (9) also have been derived for a classical system. Non-zero uneven frequency moments (eqs.6 and 7) and the detailed balance relation,

$$S(k,-\omega) = e^{-\hbar\omega/k_B T} S(k,\omega) \ , \qquad (10)$$

are a direct consequence of quantum effects. In classical systems $S(k,\omega)$ is an even function of ω. It has been shown [18] that

$$S_{cl}(k,\omega) \approx \exp \left\{ - \frac{\hbar\omega}{2k_B T} + \frac{\hbar k^2}{8Mk_B T} \right\} S(k,\omega) \ , \qquad (11)$$

which is exact for a system of non-interacting particles (see eq.4). We use eq.11 to calculate approximately the classical $S(k,\omega)$ from the experimental data. In the remainder of this thesis the classical approximation eq.11 is used for $S(k,\omega)$.

The Fourier transform of the longitudinal current-current correlation function $C_l(k,\omega)$ is in a simple way related to $S(k,\omega)$:

$$C_l(k,\omega) = \omega^2 S(k,\omega) / k^2 \ . \qquad (12)$$

3. Experimental set-up

3.1. Spectrometer

The measurements were performed with the rotating-crystal time-of-flight spectrometer RKS-1 in our institute. Details are given in table 1. The neutron wavelength was calculated from the known spacing of the (111) planes of lead and the Bragg angle. The calculated wavelength was consistent with a measurement of the time-of-flight between the two monitors (see table 1). The nominal distance between the detectors and the sample was 1200 mm. However, from time-of-flight measurements on an elastically scattering sample (vanadium) it appeared that the actual length of the flight path from sample to detector varied from detector to detector between 1182 and 1200 mm. This was due partly to a poor positioning of one of the detector boxes containing two ^{3}He-tubes, and partly to an accidental shift of the sample of approximately 1 cm towards

Table 1
Properties of the rotating-crystal spectrometer RKS-1.

monochromator	Pb single crystal of cylindrical shape
diameter	40 mm
length	50 mm
rotation axis	[211]
rotational speed	13584 rpm constant to within 1 in 10^4
reflection planes	(111)
spacing, d	0.28582 nm
Bragg angle θ_B	45.5^0
wavelength monochromatic beam, λ_0	0.408 nm
energy monochromatic beam, E_0	4.92 meV
flux at sample position	1.5×10^3 cm^{-2}s^{-1}
beam size at sample position	40 x 50 mm^2
detectors	aluminium tubes, filled with 4 bar ^{3}He, 25.4 mm diameter
range of scattering angles	4^0-100^0
flight path	1.20 m
for $0 < \varphi \leq 22.5^0$	1.0 m helium, 0.1 m air } 0.1 m vacuum
$26.5^0 < \varphi \leq 92^0$	0.5 m helium, 0.6 m air } in cryostat
monitor 1 } (BF_3 tubes)	126.5 mm in front of the sample position
monitor 2 } (BF_3 tubes)	812.0 mm behind the sample position

Table 2
Detector groups

group number	number of tubes	sensitive length (mm)	average scattering angle (deg)	FWHM angular resolution (deg)	$k(\omega=0)$ (nm^{-1})
1	4	200	11.8	5	3.2
2	4	200	19.7	5	5.3
3	2	200	27.2	3.5	7.3
4	2	300	35.2	3.5	9.3
5	2	300	43.1	3.5	11.3
6	2	300	51.1	3.5	13.3
7	2	300	59.1	3.5	15.2
8	1	300	65.8	3	16.7
9	1	300	67.0	3	17.0
10	1	300	68.2	3	17.3
11	1	300	73.8	3	18.5
12	1	300	76.2	3	19.0
13	1	300	81.6	3	20.2
14	1	300	82.8	3	20.4
15*	1	300	84.0	3	20.7
16	1	300	89.8	3	21.8
17	1	300	91.0	3	22.0
18	1	300	92.2	3	22.2

* detector group nr 15 broke down during 844-bar experiment.

the detector at 90^0 scattering angle. This situation remained unchanged during the experiment and the differences in the length of the flight path were taken into account in the data reduction.

Because of the limited memory space in the multi-channel analyser it was impossible to measure the spectra of the 29 ^{3}He detectors separately. The detectors were combined in 18 groups, each consisting of either 4, 2 or 1 detector tube, as indicated in table 2. The average scattering angle for the different detector groups is calculated from the nominal angle, the finite length of the detector tubes, and the number of detectors per group.

The angular resolution is calculated from the dimensions of the detector and of the sample and from the collimator divergence. The arrangement of the

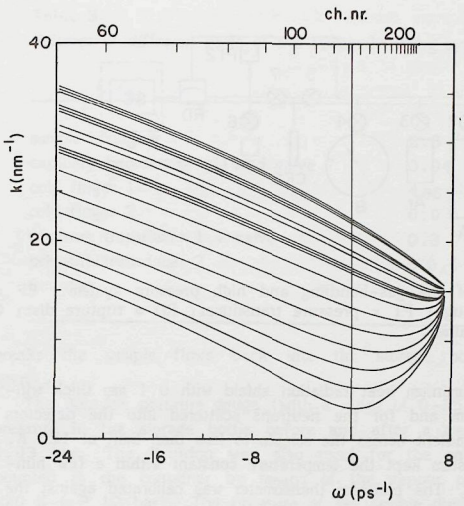

Fig.2. k as function of ω for all detector angles. Upper horizontal axis gives the time-of-flight channels corresponding to the frequency transfer on the lower horizontal axis.

detector groups indicated in table 2 was chosen in order to increase (at the expense of angular resolution) the counting rate at small scattering angles, where the structure factor of liquid argon is small and relatively flat, and to have a better angular resolution at the larger scattering angles, where the structure factor is expected to exhibit a pronounced structure. Fig.2 gives k, the momentum transfer divided by $\hbar$, as function of ω, the energy transfer divided by $\hbar$, for all the detector angles.

3.2. Sample

^{36}Ar was used because of its very large coherent scattering cross section for thermal neutrons. The sample which was obtained from Mound Laboratory, Miamisburg(Ohio), consisted of 99.6 mol% ^{36}Ar with mainly H_2, N_2 and O_2 as impurities. The container was made of 5052 aluminium alloy capillary with inner diameter 0.75 mm, and wall thickness 0.25 mm. This capillary was bent into 38 parallel sections with their center lines 1.3 mm apart, forming a plane of 50x50 mm^2. The capillary is mounted in an aluminium frame containing a NTC resistor as sensor for temperature control and a platinum resistor as thermometer. A detailed description of the container is given in paper I.

The container was mounted in a liquid nitrogen cryostat with an angle of 45^0 between the neutron beam and the normal of the plane of the container (see

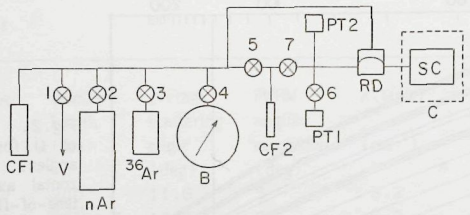

Fig.3. Schematic diagram of the gas-handling and high pressure system. CF = cold finger; B = Bourdon gauge; PT = pressure transducer; RD = rupture disc; C = cryostat; SC = sample container.

fig.3 in paper I). An aluminium heat radiation shield with 0.1 mm thick windows for the neutron beam and for the neutrons scattered into the detectors reduced the temperature gradient across the sample to less than 5mK at 120 K. The temperature control system kept the temperature constant within a few hundredth of a degree Kelvin. The platinum thermometer was calibrated against the vapour pressure of natural argon near 120 K. Thus the absolute temperature was accurate within 0.05 K, which is mainly determined by the accuracy by which the vapour pressure of argon as function of temperature is known.

The gas handling system to load the container and to retrieve the precious ^{36}Ar is indicated in fig.3. The volumes of the different parts are given in table 3. To reduce the risk of ^{36}Ar losses due to a leakage the system was made as tight and as simple as possible. The total volume was kept to a minimum, because there was only 4 liter ^{36}Ar STP available.

The ^{36}Ar is normally stored in a 0.5 l bottle at approximately 8 bar. To transfer ^{36}Ar to the sample container the cold fingers (see fig.3) are used. The internal volume of cold finger 1 is approximately equal to the volume of the total amount of ^{36}Ar in solid state.

The pressures of 20 and 270 bar at 120 K could be generated in the sample container using cold finger 1. To generate 850 bar at 120 K the volume of this cold finger is too large. Therefore, the container was cooled to a temperature slightly above the freezing point of argon and cold finger 2 was used repeatedly to build up the desired density in the sample container. Then, after closing valve 7, the container was heated to 120 K.

In case of a failure of the temperature control system and a consequential warming up of the sample container, the pressure might increase beyond the tolerance of the container. To prevent loss of the ^{36}Ar and of the container a rupture disk was mounted in the high pressure part of the system. If the disk

Table 3
Volumes of different parts of the sample handling system (fig.3) in cm^3.

sample container	2.6
capillary between sample and valve 7	0.04
cold finger 1	4
cold finger 2	0.9
pressure transducer 1 + valve	0.3
pressure transducer 2	< 0.1
Bourdon	10

breaks the sample flows back into the storage bottle (provided valve 3 is open).

The Bourdon pressure gauge (with a range of 0-35 bar) was used to check the pressure in the storage bottle before and after a measurement. The accuracy is 0.03 bar. The Bourdon was also used for the calibration of the thermometer mounted in the container by means of the vapour pressure of natural argon at 120 K (≈ 12 bar). The pressure of the sample during a measurement was monitored by means of the pressure transducers. Their internal volume is small compared to the volume of the sample and causes only small density fluctuations (see below) in the sample container if their temperature varies a few degrees. Two pressure transducers of different type were mounted: one with a range of 350 bar and 0.8 bar accuracy, used for the measurements at 19.5 and 267 bar and a second one with a 1000 bar range and 1 bar accuracy for the 844 bar measurement. During the 844 bar measurement valve 6 remained closed.

Because the ^{36}Ar had to serve future experiments too, some care was taken to avoid pollution of the sample with impurities. Before the ^{36}Ar was released from the storage bottle, the entire system was three times flushed with natural argon and evacuated. The natural argon was cleaned of possible water contamination by leading it through a coiled capillary immersed in a mixture of solid carbon dioxide and acetone (195 K). Once water gets into the 5m long capillary of the container it is very hard to get it out again and it might lead to an obstruction (particularly in the narrow steel capillary connecting the container with the gas handling system outside the cryostat). During a measurement the pressure transducer and the rupture disk remained connected with the sample.

The volume of the capillary connecting the pressure transducer with the sample must be small enough to keep density fluctuations in the sample container due to temperature fluctuations in the capillary within acceptable lim-

its. On the other hand the inner diameter should not be so small that evacuating the sample container to 0.1 bar takes too much time. We chose for an inner diameter of 0.2 mm. The volume of the capillary is then 0.04 cm^3, which is small compared to the volume of the container (table 3), and evacuating from 1 to 0.1 bar takes approximately 20 minutes.

It can be calculated that the contamination of the ^{36}Ar with the natural argon used for flushing is less than 10^{-4}, if at least a few hours is pumped on the entire gas system before the ^{36}Ar is let in.

The estimated total non-thermostated volume, connected to the sample container during a measurement, was 0.4 cm^3 using pressure transducer 1 and 0.2 cm^3 using pressure transducer 2. A temperature variation of 1 K of this volume leads to relative density variations of less than 10^{-4}.

3.3. Measurements

Apart from the three measurements on ^{36}Ar at different pressures also the scattering from the empty container and from vanadium was measured. The vanadium serves to determine the time-of-flight resolution of the spectrometer and

Table 4
Some properties of vanadium

number density ρ	69.8 nm^{-3} (at 300 K)
	70.2 nm^{-3} (at 120 K)
bound atom scattering cross section σ_s	4.98 b
coherent scattering cross section σ_c	0.02 b
absorption cross section σ_a	11.5 b (for E_o = 4.92 meV)
lattice constant	0.303 nm
linear thermal expansion coefficient	$\leq 8 \times 10^{-6} K^{-1}$ (120-300 K)
Debije-Waller coefficient B	33.5 x 10^{-6} nm^2 (at 300 K)
	11x10^{-6} nm^2 (at 120 K)

References:
W. Dilg, Nucl.Instr.Meth. **122**(1974)343.
M. Kamal, S.S. Malik and D. Rorer, Phys.Rev.B **18**(1978)1609.
V.F. Sears, Thermal-Neutron Scattering Lengths and Cross Sections for Condensed-Matter Research, AECL-8490 (Atomic Energy Canada Ltd., Chalk River, Ontario, 1984).
D.I. Bolef, R.E. Smith and J.G. Miller, Phys.Rev. B3(1971)4100.

Table 5
The measurements in chronological order. One run usually took 24 hours. All measurements are at 120 K.

number	sample	number of runs
1	empty container	9
2	^{36}Ar, 20 bar	10
3	^{36}Ar, 270 bar	7
4	empty container	4
5	vanadium	5
6	empty container	5
7	empty container	4
8	vanadium	9
9	empty container	3
10	^{36}Ar, 844 bar	9

to calibrate the efficiency of the detectors for elastically scattered neutrons. For these purposes the elastic peak has to be separated from the inelastic part in the vanadium spectrum.

The relevant properties of vanadium are summarized in table 4. In the present case coherent scattering can be neglected because it is less than 1% of the total scattering and the first Bragg peak occurs at a scattering angle of 144° which is beyond the largest scattering angle in the measurements

We chose to measure the vanadium at 120 K and not at room temperature to reduce the correction for inelastic scattering. At k = 20 nm^{-1} the Debije-Waller factor exp $(-2Bk^2)$, with B the Debije-Waller coefficient given in table 4, increases from 0.974 at room temperature to 0.991 at 120 K. Two 1 mm thick plates were mounted on either side of the empty ^{36}Ar container in the same cryostat and in the same position as in the argon measurements. Thus no additional background measurement is needed for correction of the vanadium measurement.

The different measurements are given in table 5 in chronological order. Due to experimental circumstances there is a time lag of several months between the measurements at the two lower pressures and the 844 bar measurements. Therefore the vanadium and empty container measurements were repeated. Each measurement is the sum of a number of runs, which are stored separately, in

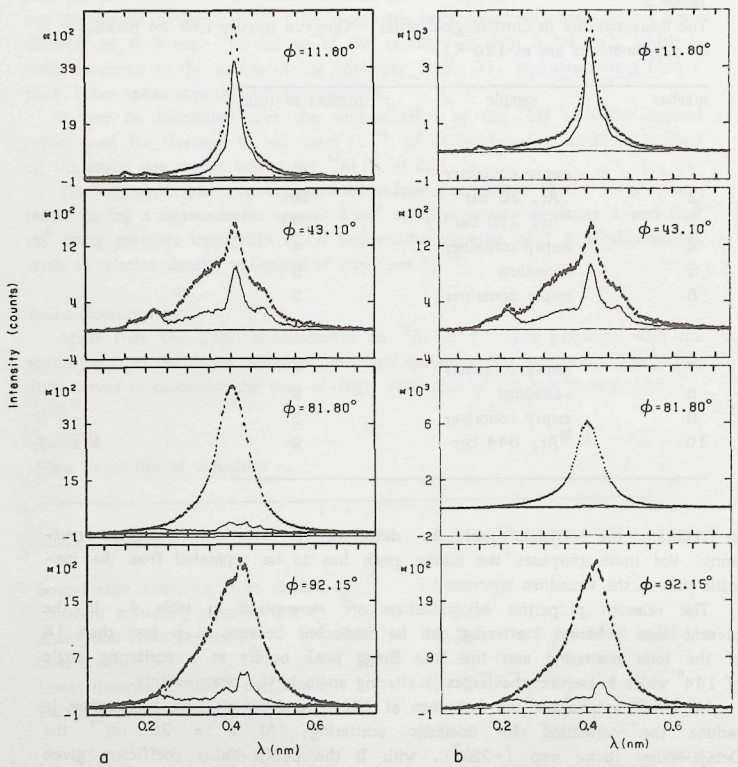

Fig.4. Spectra at four scattering angles for the argon (a: 20 bar; b: 270 bar; c: 844 bar) and vanadium (d) measurements (error bars) together with the background (measurement with empty container) (solid lines) after subtraction of the constant background level. The vertical axis is in arbitrary units, but all measurements are normalized to the same incident neutron intensity.

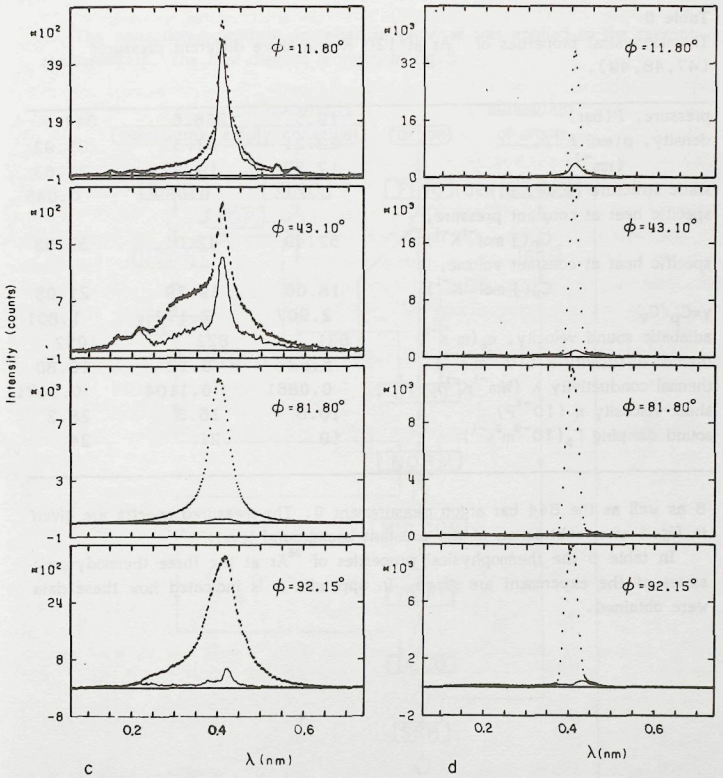

the first place to avoid losing the data of a whole measurement in case something goes wrong and in the second place to detect by means of statistical checks deviations caused by drift, interference, etc.

As an additional check the empty container measurements were repeated. Indeed measurements 1 and 4 are consistent, but 4 and 6 differ a few percent, probably due to dismounting and opening the cryostat before and after the vanadium measurement (nr. 5). Measurements 7 and 9 are again consistent. We used nr. 1 to correct the argon measurements 2 and 3, the sum of 4 and 6 to correct the first vanadium measurement 5, and the sum of 7 and 9 to correct

Table 6
Thermophysical properties of ^{36}Ar at 120 K and three different pressures [47,48,49].

pressure, P(bar)	19.5	266.6	844
density, ρ(mol ℓ^{-1}),	29.21	32.37	35.92
(nm^{-3})	17.59	19.49	21.63
static structure factor, S(k=0)	0.202	0.089	0.045
specific heat at constant pressure, C_p(J $mol^{-1}K^{-1}$)	52.49	42.01	37.93
specific heat at constant volume, C_v(J $mol^{-1}K^{-1}$)	18.06	19.29	21.05
$\gamma=C_p/C_v$	2.907	2.177	1.801
adiabatic sound velocity, c_s(m s^{-1})	631	822	1052
thermal diffusivity a ($10^{-8}m^2s^{-1}$)	5.62	8.12	10.80
thermal conductivity λ ($Wm^{-1}K^{-1}$)	0.0861	0.1104	0.1471
shear viscosity η (10^{-4}P)	10.8	16.3	28.2
sound damping Γ_s($10^{-8}m^2s^{-1}$)	19	21	24

8 as well as the 844 bar argon measurement 9. The measured spectra are given in fig.4 after subtraction of the constant background level.

In table 6 the thermophysical properties of ^{36}Ar at the three thermodynamic states of the experiment are given. In appendix A is indicated how these data were obtained.

4. Corrections

The correction procedure described in paper II was applied to the present measurements. The flow diagram is given in fig.5.

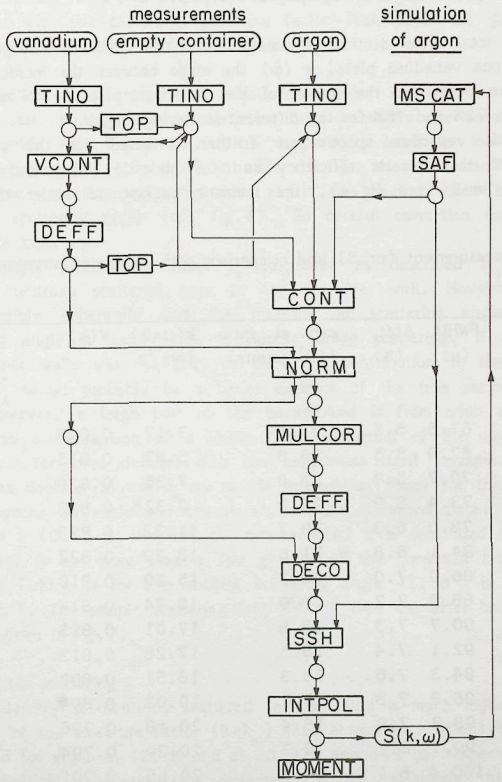

Fig.5. Flow diagram of the correction procedure applied to the measurements. The names in rectangular boxes refer to computer programs explained in paper II, except VCONT which is a simple program to correct the vanadium measurement for background according to section 4.1.

4.1. Calibration

The empty container measurements were subtracted from the vanadium measurements with an angle dependent attenuation factor $f_v(\varphi)$ according to:

$$f_v(\varphi) = \exp [- \rho\sigma_R d \{1/\cos\psi + 1/\cos(\psi-\varphi)\}] ,$$

with σ_R the total cross section of vanadium for the incident energy, d the thickness of one vanadium plate, ψ (φ) the angle between the incident (scattered) neutron beam and the normal of the vanadium plates. The attenuation varies between 72% and 76% for the different scattering angles.

The elastic vanadium spectra are further corrected for the wavelength dependence of the detector efficiency and for inelastic background. Because the latter is small (see fig.4), the inelastic background under the elastic

Table 7

Vanadium measurement (nr.5) and comparison with calculated structure factor V(k).

det.angle (^{0})	FWHM (μs)	$\Delta t/t_0$ (%)	exp. el. int. (10^4 counts)	k(ω=0) (nm^{-1})	V(k)
11.8	67.6	5.5	35.4	3.17	0.807
19.7	67.9	5.5	38.8	5.27	0.815
27.2	70.7	5.7	23.0	7.25	0.820
35.2	73.4	5.9	28.3	9.32	0.823
43.1	78.0	6.3	29.7	11.32	0.823
51.1	84.1	6.8	21.8	13.29	0.822
59.1	86.9	7.0	26.3	15.20	0.819
65.8	88.8	7.2	18.0	16.74	0.814
67.0	90.7	7.3	18.8	17.01	0.813
68.2	92.1	7.4	18.5	17.28	0.812
73.8	94.3	7.6	18.3	18.51	0.807
76.2	96.3	7.8	8.6	19.02	0.804
81.8	98.3	7.9	18.4	20.18	0.796
82.8	99.7	8.1	18.3	20.39	0.794
84.2	100.4	8.1	14.2	20.66	0.791
89.8	102.4	8.3	16.9	21.76	0.780
91.0	103.7	8.4	16.9	21.98	0.777
92.2	105.5	8.5	16.5	22.20	0.774

peak is determined by fitting a straight line to the wings of the measured peak. We chose 7 adjacent time-of-flight channels on either side of the peak, four times the Full Width at Half Maximum (FWHM) away from the top. The two averages of each series of 7 channels determined the straight line.

The detectors were calibrated by comparing the intensity in the vanadium measurement with the calculated structure factor (see paper II) given in table 7. Also the time-of-flight resolution is given.

4.2. Correction of the argon measurements for container scattering

In contrast to the isotropic scattering from vanadium the coherent scattering by liquids well below the critical temperature leads to low intensity at small scattering angles (cf. S(0) in table 6). On the other hand the scattering from the container walls and from air in the neutron beam increases with decreasing scattering angle (cf. fig.4). So careful correction for background scattering is important.

The sample attenuation factor f_s calculated as described in paper II is valid for neutrons scattered once in the container wall. However, aluminium scatters mainly coherently and the intensity at scattering angles below the first Bragg angle is mainly due to double Bragg scattering. If scattering by the container walls was the only or the main contribution to the total background, f_s^2 would probably be a better estimate of the true sample attenuation factor. However, a large part of the background is from other sources. This follows from a comparison of a Monte Carlo simulation of the experiment (see section 4.3 for more details) with the experiment itself (compare figs.6 and 4). It was decided to use f_s as sample attenuation factor for the background. This introduces an additional uncertainty in the corrected data, but since f_s is close to 1 (0.96 in the 844 bar measurement) it is concluded that this systematic error is not more than a few percent of the corrected intensity in the worst case (which is for the smallest scattering angle -11.8^0- in the 844 bar measurement). The sample scattering from ^{36}Ar at 844 bar after background correction is given in fig.7.

4.3. Multiple scattering

The intensity of neutrons scattered from a liquid is much higher around the main peak of the structure factor ($k=k_m$) than at small k: $S(k_m)/S(o)$ is 9.1, 23 and 53 for argon at 120 K and at 20,270 and 844 bar respectively. Consequently multiple scattering is expected to be relatively high at small scattering angles, especially in the 844 bar measurement. In order to correct for multiple scattering the experiment was simulated by means of the Monte Carlo computer program MSCAT [19]. Since multiple scattering depends on the form of $S(k,\omega)$ (see paper II), the model $S(k,\omega)$ used in the simulations with MSCAT was refined iteratively as described in paper II. As a first trial for

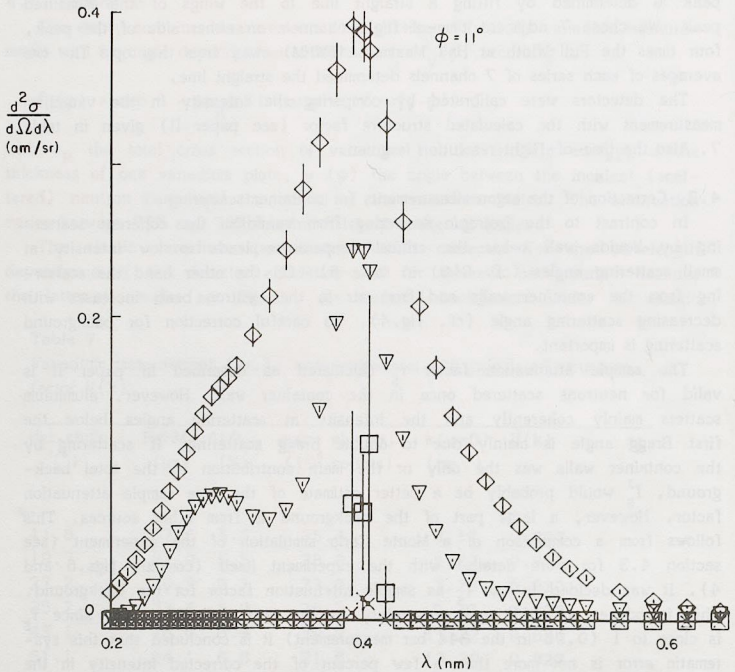

Fig.6. Double differential cross section of single scattering by the sample (triangles), multiple scattering by the sample (diamonds), single scattering by the container walls (crosses), and multiple scattering by the container walls (squares), for a scattering angle of 11°. (1 am = 10^{-18}m) The graph results from a simulation by means of MSCAT with 4000 neutron histories.

$S(k,\omega)$ we used linearized hydrodynamics for $k < 3.3$ nm^{-1} (with the data from table 6) and Kurkijärvi's model [20] for $k \geq 3.3$ nm^{-1}. The latter expresses the dynamic structure factor $S(k,\omega)$ in terms of its self part $S_s(k,\omega)$, the static structure factor $S(k)$, and the second and fourth frequency moments of $S(k,\omega)$. $S_s(k,\omega)$ is the Fourier transform of eq.1, if $\rho(\vec{r},t)$ is replaced by $\rho_1(\vec{r},t) = \delta(\vec{r}-\vec{R}_1(t))$, and Lovesey's [21] model was used to evaluate S_s.

The Monte Carlo simulations were performed for 16 detectors and 50

time-of-flight channels. Container scattering was included in the simulation (using the data in paper I) as well as time-of-flight resolution.

In MSCAT the resolution is determined by the position of the zero-covariance point (ZCP), the spread in velocity and the spread in time-of-arrival of the neutron pulse at ZCP (see section 3.2.1. of paper II). ZCP was chosen at a distance of 1.40 m behind the monochromator, approximately coincident with the

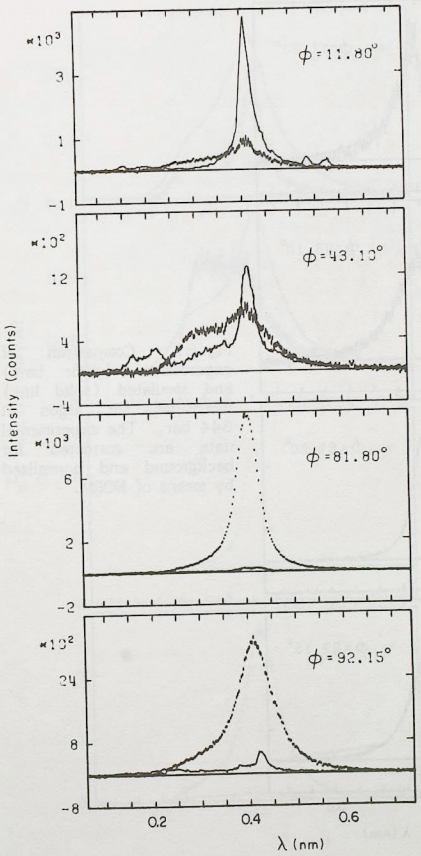

Fig.7. Experimental spectra for argon at 844 bar after background subtraction (error bars), together with the background (solid line).

focussing point of the rotating crystal, given by $L = 2v/(\omega_M tg\theta_B)$. v is the average neutron velocity (971 m s^{-1}), ω_M the angular velocity of the rotating crystal (1422.5 rad s^{-1}), and θ_B the Bragg angle (45.5°). From the observed neutron pulse width at the two monitors the spread in time-of-arrival at ZCP and the spread in inverse velocity were estimated to be 17 μs and 17 μs m^{-1}, respectively.

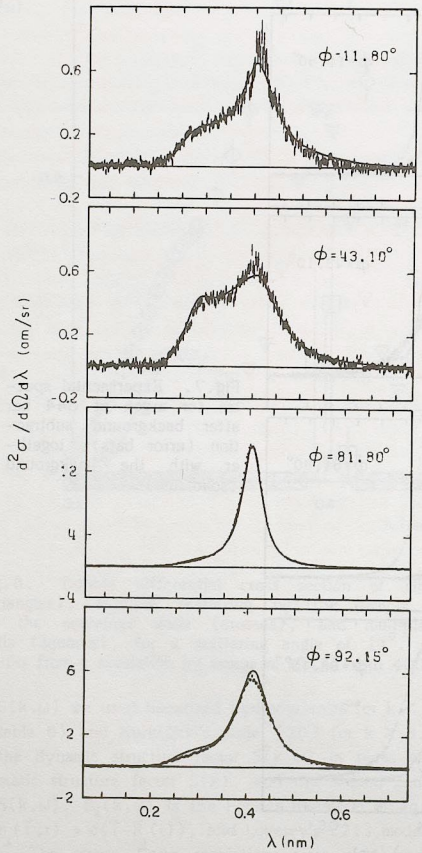

Fig.8. Comparison of experimental (error bars) and simulated (solid line) intensities for argon at 844 bar. The experimental data are corrected for background and normalized by means of NORM.

The results from the third iteration (with 4000 neutron histories simulated) are given in figs.8 and 9 and compared with the measured spectra. Fig.8 demonstrates the excellent agreement between the measured and simulated (single + multiple scattering from sample) intensity. At small scattering angles the multiple scattering exceeds the single scattering !

The correction for multiple scattering was executed using the factor method

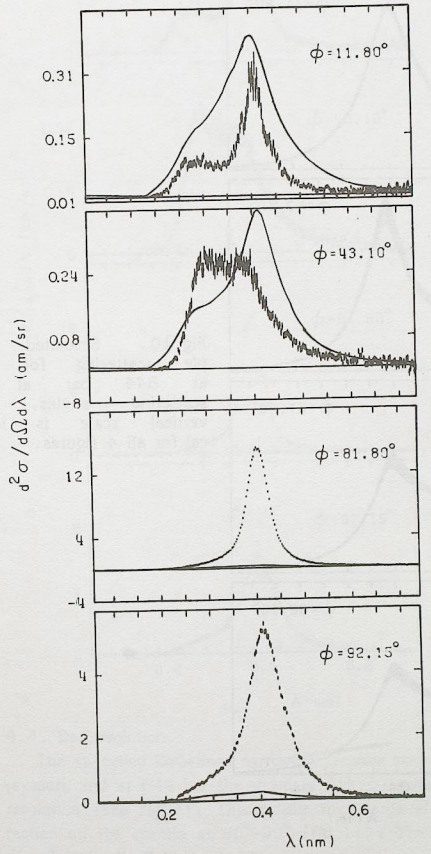

Fig.9. Experimental spectra for argon at 844 bar corrected for multiple scattering (error bars) and the simulated multiple scattering (solid line).

(see paper II). It is interesting to note that the multiple scattering is not isotropic, but decreases considerably between 43^0 and 90^0 scattering angle (see fig.10) ! It is also clear from fig.10 that duty-cycle overlap should not be neglected in the present case.

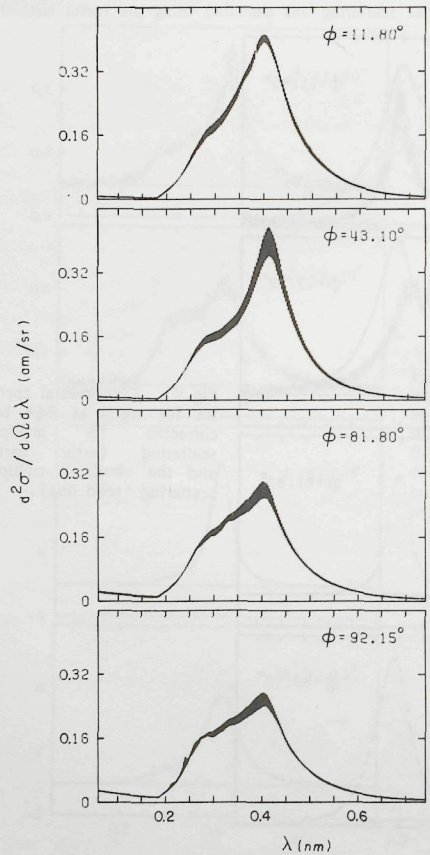

Fig.10. Simulated multiple scattering for argon at 844 bar at four scattering angles. The vertical scale is identical for all 4 figures.

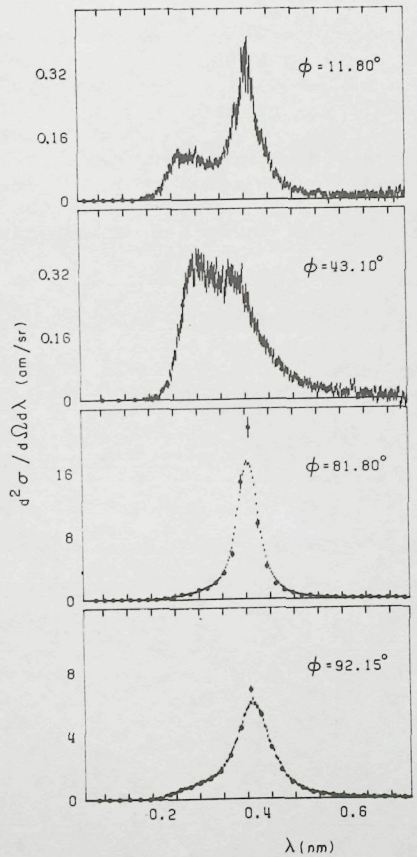

Fig.11. Experimental spectra for argon at 844 bar before (error bars) and after (dots with error bars) correction for time-of-flight resolution.

4.4. Deconvolution.

The so-called DeGennes narrowing becomes more pronounced with increasing pressure and at 844 bar the width of $S(k,\omega)$ comes close to the width of the resolution (see fig.4). This results in a large effect of the resolution correction on the spectra at 80^0-90^0 (fig.11). The method of deconvolution is described in detail in paper III.

5. Results

The fully corrected $S(k,\omega)$ from the 844 bar measurement is given in fig.12 at a few values of ω and all detector angles. There is a discrepancy between the energy-gain and energy-loss data at ω=0.4 ps^{-1} around the main peak of the structure factor. This can also be seen from the quality factor $Q^2(\omega)$ i.e. Q^2_{ij} averaged over all k and over ω-intervals of 1 ps^{-1} (Q^2_{ij} is defined by eq.22 in paper II), which is displayed in fig.13 for the data at the three pressures. Clearly this discrepancy at small ω is much smaller for the data at lower pressure. A possible explanation is that the DeGennes narrowing around the main peak of the structure factor (at k ~ 20 nm^{-1}) becomes less pronounced with decreasing pressure (see figs.14 and 15). Consequently the correction for

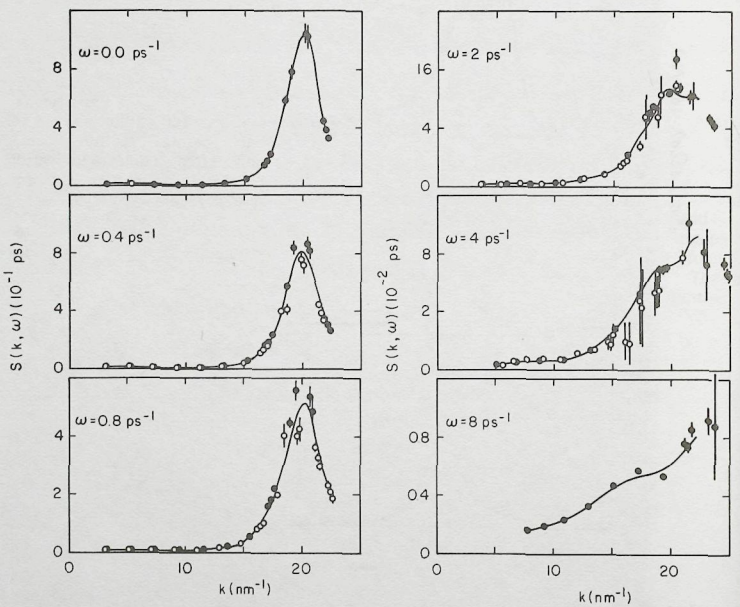

Fig.12. Fully corrected $S(k,\omega)$ plotted as function of k from the RKS-1 measurements on liquid ^{36}Ar at 120 K an 844 bar. Dots: energy-gain; open circles: energy-loss; solid line: average calculated from the two sets of data according to paper II, section 3.3.1. At ω = 8 ps^{-1} energy loss is impossible.

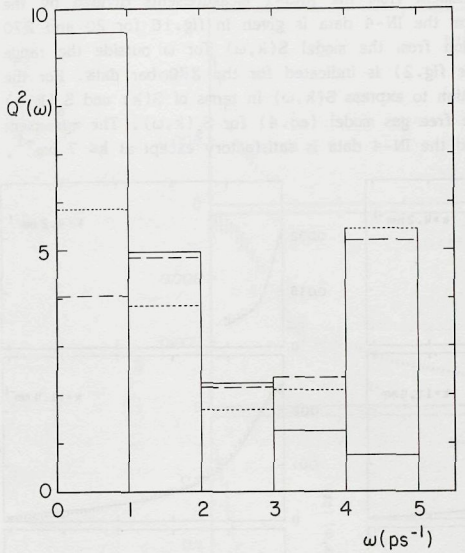

Fig.13. Q^2 for the RKS-1 data at 20 (broken line), 270 (dashed line), and 844 bar (solid line) (see eq.22 in paper II).

resolution is more difficult to apply to the data at the higher pressure, resulting in a less accurate knowledge of the exact shape of $S(k,\omega)$ at φ = 81.8° around ω = 0 (see fig.11). Apparently the spline interpolation deviates significantly from the true $S(k,\omega)$ in this (k,ω)-area due to the relatively wide spacing of the data after the resolution correction by DECO. The error is partly compensated for by taking the (weighted) average of the energy-gain and energy-loss data and the difference is accounted for in the estimated error of $S(k,\omega)$ on the rectangular (k,ω)-grid (see section 3.3.1 of paper II).

$S(k,\omega)$ as function of ω at constant k is given for all three pressures in figs.14 and 15. In fig.14 the $S(k,\omega)$-data at 20 and 270 bar measured with the RKS-1 are compared with the corresponding IN-4 data [14]. On the average the consistency appears to be satisfactory, which stresses the reliability of both the IN-4 data and the RKS-1 data, and reinforces the credibility of the present data at 844 bar. Note that in fig.15 the vertical scale for k = 19.8 nm^{-1} is 100 x increased with respect to the scale for k = 11.4 nm^{-1}.

The zeroth frequency moment from the RKS-1 measurements divided by the zeroth frequency moment from the IN-4 data is given in fig.16 for 20 and 270 bar. The relative contribution from the model $S(k,\omega)$ for ω outside the range covered by the RKS-1 (see fig.2) is indicated for the 270 bar data. For the model Skold's [22] prescription to express $S(k,\omega)$ in terms of $S(k)$ and $S_s(k,\omega)$ was used, together with the free gas model (eq.4) for $S_s(k,\omega)$. The agreement between the RKS-1 data and the IN-4 data is satisfactory except at $k \lesssim 7$ nm^{-1},

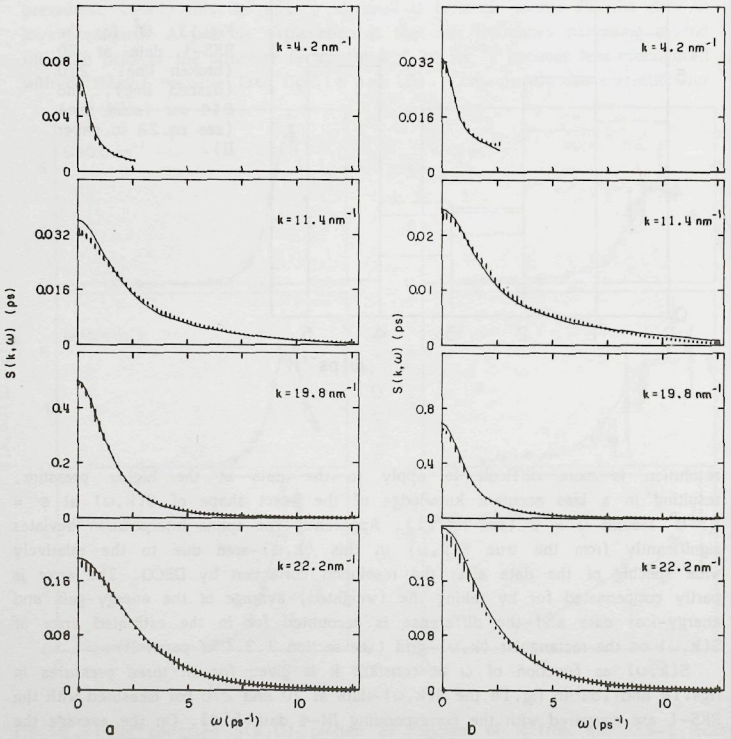

Fig.14. Comparison of the data from the RKS-1 (error bars) and from the IN-4 (solid line) for (a) 20 and (b) 270 bar.

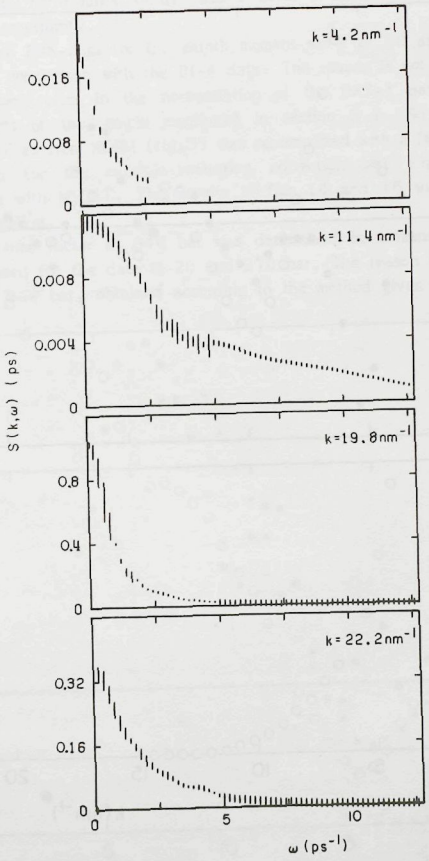

Fig.15. $S(k,\omega)$ at 844 bar.

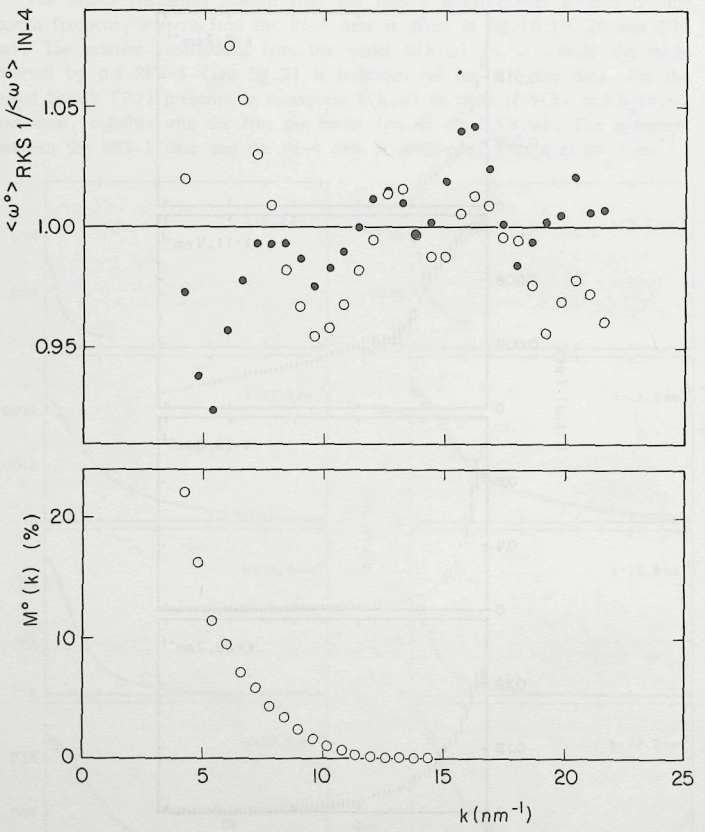

Fig.16. S(k) obtained from RKS-1 measurements divided by S(k) obtained from IN-4 measurements at 20 (dots) and 270 (open circles) bar. The contribution from the model S(k,ω) at large ω is indicated separately in the lower graph.

where the model contribution to the RKS-1 data, $M^0(k)$, is 8-20 %, leading to an increased uncertainty.

Initially the RKS-data for the zeroth moment $<\omega^0>$ at 20 and 270 bar were 10 % high in comparison with the IN-4 data. The reason is not known, but it is ascribed to some error in the normalization of the RKS-1 data related to the accidental shift of the sample mentioned in section 3.1. So the output from INTPOL as well as from NORM (fig.5) was renormalized with a factor 0.9 and the iteration loop for the multiple-scattering correction was executed one more time, starting with MSCAT. The results in figs.14 and 16 were obtained after this renormalization.

The structure factor at 844 bar was determined in a manner different from the method used for the data at 20 and 270 bar. The reason is that the resulting S(k) at 844 bar, obtained according to the method given above, seemed at

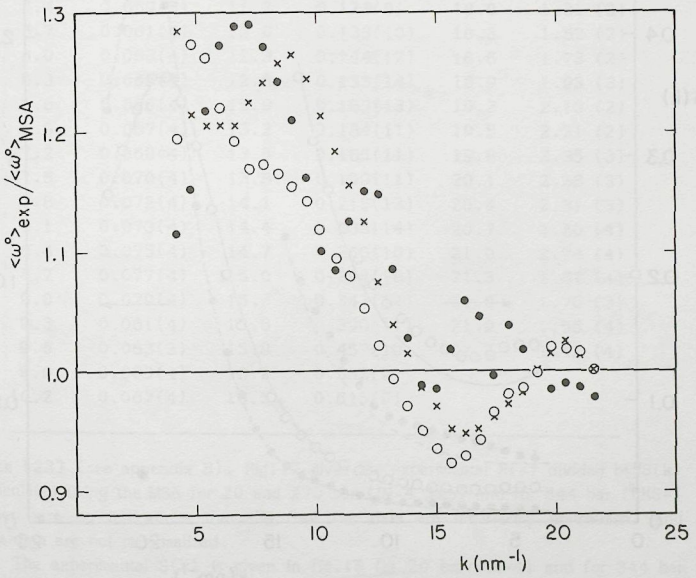

Fig.17. Experimental S(k) divided by S(k) calculated using MSA. The experimental data are from IN-4 measurements at 20 (open circles) and 270 bar (crosses) and from RKS-1 measurement at 844 bar (dots).

small k to be inconsistent with S(0) obtained from the equation of state. However if S(k) is determined from a least squares fit of a sum of three Lorentzians to the experimental $S(k,\omega)$ (see next section for details), the results are consistent with S(0). This might be due to the fact that the width of $S(k,\omega)$ at $k \leq 15$ nm^{-1} increases with pressure so that the contribution to S(k) outside the spectrometer range increases and $M^0(k)$ becomes more important.

To check the normalization of the 844 bar data, the experimental S(k) is compared with the Mean Spherical Approximation (MSA) according to Madden and

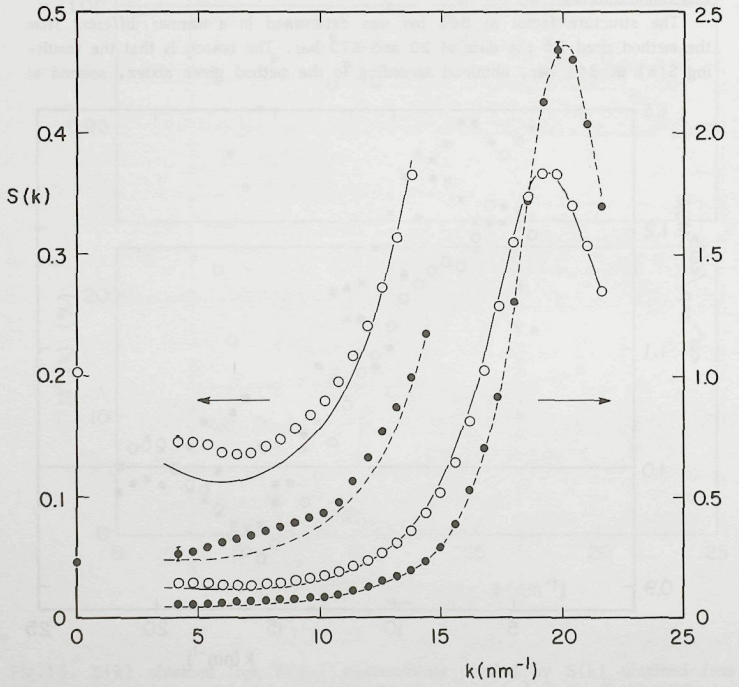

Fig.18. Experimental and model S(k) at 20 and 844 bar. Open circles: IN-4 data, 20 bar; dots: RKS-1 data, 844 bar; solid line: MSA 20 bar; dashed line MSA 844 bar. The estimated uncertainty is indicated at a few points with error bars.

Table 8

The static structure factor S(k) of liquid argon at 120 K and 844 bar. The density is 21.6 nm^{-3}. The estimated accuracy of the last figures is indicated in parentheses.

k (nm^{-1})	S(k)	k (nm^{-1})	S(k)	k (nm^{-1})	S(k)
4.2	0.053(4)	10.5	0.091(4)	16.8	0.705(9)
4.5	0.054(4)	10.8	0.096(7)	17.1	0.82 (2)
4.8	0.055(3)	11.1	0.104(7)	17.4	0.92 (4)
5.1	0.057(3)	11.4	0.113(8)	17.7	1.10 (3)
5.4	0.059(3)	11.7	0.123(9)	18.0	1.31 (2)
5.7	0.061(4)	12.0	0.133(10)	18.3	1.52 (2)
6.0	0.063(4)	12.3	0.144(12)	18.6	1.73 (2)
6.3	0.065(4)	12.6	0.155(14)	18.9	1.93 (3)
6.6	0.066(4)	12.9	0.163(13)	19.2	2.13 (2)
6.9	0.067(4)	13.2	0.184(11)	19.5	2.21 (2)
7.2	0.069(4)	13.5	0.186(11)	19.8	2.35 (3)
7.5	0.070(4)	13.8	0.199(11)	20.1	2.38 (3)
7.8	0.072(4)	14.1	0.215(13)	20.4	2.31 (3)
8.1	0.073(4)	14.4	0.235(14)	20.7	2.20 (4)
8.4	0.075(4)	14.7	0.260(16)	21.0	2.04 (4)
8.7	0.077(4)	15.0	0.294(18)	21.3	1.87 (4)
9.0	0.079(4)	15.3	0.347(14)	21.6	1.70 (3)
9.3	0.081(4)	15.6	0.390(11)	21.9	1.55 (4)
9.6	0.083(3)	15.9	0.457(10)	22.2	1.42 (4)
9.9	0.085(4)	16.2	0.532(9)		
10.2	0.087(4)	16.5	0.615(9)		

Rice [23] (see appendix B). Fig.17 gives the experimental S(k) divided by S(k) calculated using the MSA for 20 and 270 bar (IN-4 data) and for 844 bar (RKS-1 There are no indications that the 844 bar data are incorrectly normalized, and the data are not renormalized.

The experimental S(k) is given in fig.18 for 20 bar (IN-4) and for 844 bar (RKS-1). There is a considerable decrease at small k of more than a factor 2. The height of the main peak increases by about 30% and its position shifts from k = 19.5 nm^{-1} to k = 20.2 nm^{-1} upon increasing the density. The relatively simple MSA is in good agreement with the data. The experimental data for S(k) at 844 bar are given in table 8.

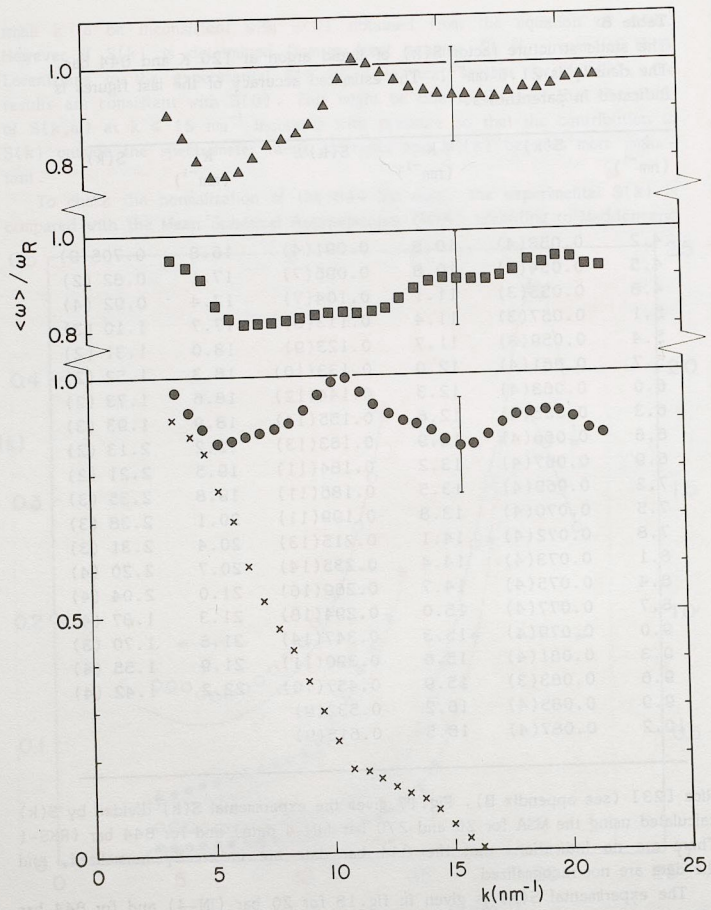

g.19. $\langle\omega\rangle.(\hbar k^2/2M)^{-1}$ for the RKS-1 measurements at 20 (triangles), 270 squares) and 844 (dots) bar. The estimated uncertainty is indicated at k = 5.6 nm^{-1}. The contribution from the model $S(k,\omega)$ at large ω for 844 bar is dicated by crosses.

The first frequency moment $\langle\omega\rangle$ divided by the exact theoretical value $\hbar k^2/2M$ is given in fig.19 for the RKS-1 measurements at the three pressures. At small k the result is nearly completely determined by the model $S(k,\omega)$ for ω outside the experimentally covered region (in all three cases Sköld's model). At larger k, where the contribution of the model is small, the deviation of $\langle\omega\rangle$ from $\hbar k^2/2M$ is not larger than its estimated experimental error as indicated in fig.19.

The fully corrected $S(k,\omega)$ at 844 bar is given in table 9 and compared with $S(k,\omega)$ at 20 bar in fig.20. The difference is considerable for a density change of only ~ 20 %.

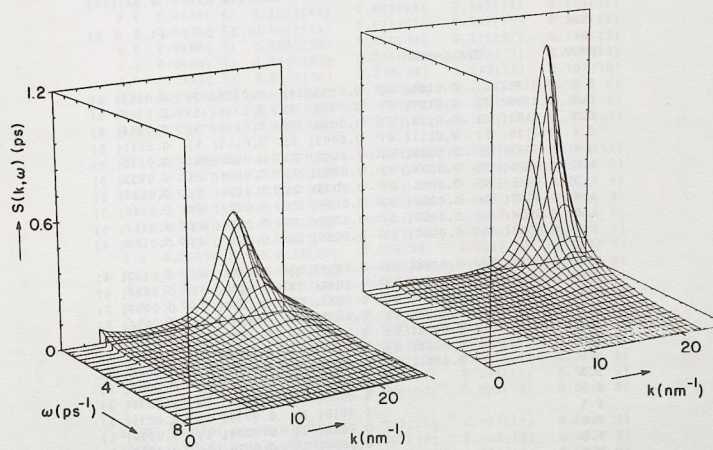

Fig.20. 3-dimensional view of $S(k,\omega)$ at 20 (left) and 844 (right) bar.

Table 9.

$S(k,\omega)$(in ps) of liquid argon at 120K and 844 bar (ρ=21.6 nm^{-3}) as function of $k(nm^{-1})$ and $\omega(ps^{-1})$, and the derived quantities S(k), FWHM (ps^{-1}), OMM=ω_M (ps^{-1}), and CLM=$C_\ell(k,\omega_M)(10^{-4}nm^2ps^{-1})$. Numbers in parentheses indicate the estimated standard deviation in the last figures of each entry.

K	4.2	6.0	8.4	11.4	12.0
S(K)	0.053(4)	0.063(4)	0.075(4)	0.113(8)	0.134(10)
FWHM	1.57 (21)	1.76 (14)	4.44 (34)	5.87 (46)	5.56 (38)
OMM				9.96 (37)	9.67 (22)
CLM				14.2 (7)	13.4 (6)
OMEGA	S(K,OMEGA)				
0.0	0.0191(11)	0.0165(8)	0.0099(4)	0.0116(7)	0.0146(8)
0.2	0.0179(7)	0.0157(5)	0.0098(3)	0.0116(5)	0.0146(5)
0.4	0.0152(6)	0.0136(5)	0.0096(3)	0.0114(5)	0.0144(5)
0.6	0.0120(5)	0.0111(4)	0.0093(2)	0.0113(5)	0.0141(5)
0.8	0.0093(5)	0.0089(4)	0.0088(2)	0.0110(5)	0.0138(5)
1.0	0.0076(5)	0.0074(3)	0.0082(2)	0.0108(5)	0.0133(5)
1.2	0.0066(5)	0.0065(3)	0.0075(2)	0.0104(5)	0.0127(5)
1.4	0.0060(6)	0.0060(3)	0.0069(2)	0.0099(4)	0.0120(5)
1.6	0.0054(5)	0.0057(3)	0.0062(2)	0.0094(4)	0.0114(5)
1.8	0.0047(3)	0.0052(2)	0.0056(2)	0.0090(4)	0.0108(4)
2.0	0.0039(2)	0.0046(2)	0.0052(2)	0.0085(4)	0.0102(4)
2.5	0.0030(2)	0.0037(2)	0.0046(2)	0.0070(3)	0.0082(4)
3.0		0.0027(5)	0.0041(2)	0.0052(7)	0.0063(7)
3.5		0.0025(2)	0.0036(2)	0.0047(8)	0.0056(8)
4.0		0.0023(2)	0.0032(5)	0.0041(5)	0.0048(5)
4.5		0.0022(2)	0.0029(6)	0.0038(4)	0.0044(8)
5.0		0.0021(2)	0.0025(2)	0.0039(2)	0.0046(2)
5.5			0.0023(1)	0.0037(1)	0.0043(2)
6.0			0.0021(1)	0.0034(1)	0.0039(2)
6.5			0.0020(1)	0.0030(1)	0.0035(1)
7.0			0.0018(1)	0.0028(1)	0.0032(1)
7.5			0.0017(1)	0.0026(1)	0.0029(1)
8.0			0.0017(1)	0.0025(1)	0.0027(1)
8.5			0.0016(1)	0.0023(1)	0.0025(1)
9.0				0.0022(1)	0.0023(1)
9.5				0.0020(1)	0.0021(1)
10.0					
11.0				0.0018(1)	0.0019(1)
12.0				0.0015(1)	0.0016(1)
13.0				0.0011(1)	0.0012(1)
				0.0008(1)	0.0009(1)

Table 9 (continued)

K	12.6	16.2	19.2	19.8	22.2
S(K)	0.154(14)	0.532(9)	2.13 (2)	2.35 (3)	1.42 (4)
FWHM	5.21 (34)	3.19 (25)	1.69 (12)	1.63 (25)	
OMM	9.32 (17)	5.95 (34)	3.35 (69)	3.23 (67)	
CLM	12.7 (8)	13.1 (31)	15.1 (16)	16.3 (13)	
OMEGA	S(K,OMEGA)				
0.0	0.0183(8)	0.1090(23)	0.858(20)	1.023(19)	
0.2	0.0182(6)	0.1075(25)	0.807(93)	0.979(47)	0.341(18)
0.4	0.0179(6)	0.1034(44)	0.685(99)	0.849(94)	0.323(25)
0.6	0.0174(6)	0.0969(54)	0.571(82)	0.662(99)	0.288(22)
0.8	0.0168(6)	0.0883(58)	0.461(37)	0.511(87)	0.250(21)
1.0	0.0160(5)	0.0785(60)	0.346(41)	0.398(7)	0.217(19)
1.2	0.0151(5)	0.0692(56)	0.278(38)	0.293(14)	0.192(15)
1.4	0.0142(5)	0.0613(41)	0.228(19)	0.221(25)	0.173(6)
1.6	0.0134(5)	0.0545(29)	0.168(19)	0.192(34)	0.156(9)
1.8	0.0127(5)	0.0482(32)	0.133(3)	0.172(5)	0.139(14)
2.0	0.0118(5)	0.0429(33)	0.117(20)	0.139(11)	0.122(15)
2.5	0.0092(4)	0.0334(11)	0.087(20)	0.094(7)	0.091(6)
3.0	0.0081(4)	0.0257(59)	0.066(5)	0.072(6)	0.074(6)
3.5	0.0066(3)	0.0216(83)	0.045(3)	0.049(3)	0.055(4)
4.0	0.0058(3)	0.0191(51)	0.035(4)	0.036(4)	0.051(6)
4.5	0.0052(5)	0.0167(5)	0.027(3)	0.028(3)	0.039(4)
5.0	0.0055(3)	0.0137(23)	0.020(20)	0.022(19)	0.025(9)
5.5	0.0051(2)	0.0114(23)	0.016(20)	0.017(19)	0.020(9)
6.0	0.0046(2)	0.0096(23)	0.013(20)	0.014(19)	0.017(9)
6.5	0.0041(2)	0.0083(23)	0.011(20)	0.011(19)	0.014(9)
7.0	0.0037(1)	0.0070(23)	0.009(20)	0.009(19)	0.012(9)
7.5	0.0033(1)	0.0058(23)	0.007(20)	0.007(19)	0.010(9)
8.0	0.0030(1)	0.0049(23)	0.006(20)	0.006(19)	0.008(9)
8.5	0.0027(1)	0.0040(23)	0.005(20)	0.005(19)	0.007(9)
9.0	0.0025(1)	0.0033(23)	0.004(20)	0.004(19)	0.005(9)
9.5	0.0022(1)	0.0027(23)	0.003(20)	0.003(19)	0.004(9)
10.0	0.0020(1)	0.0023(23)	0.003(20)	0.003(19)	0.004(9)
11.0	0.0016(1)	0.0016(23)	0.002(20)	0.002(19)	0.003(9)
12.0	0.0012(1)	0.0012(23)	0.001(20)	0.001(19)	0.002(9)
13.0	0.0009(1)	0.0009(23)	0.001(20)	0.001(19)	0.001(9)
14.0	0.0006(1)	0.0006(23)	0.000(20)	0.000(19)	0.001(9)
15.0	0.0004(1)	0.0004(23)	0.000(20)	0.000(19)	0.000(9)

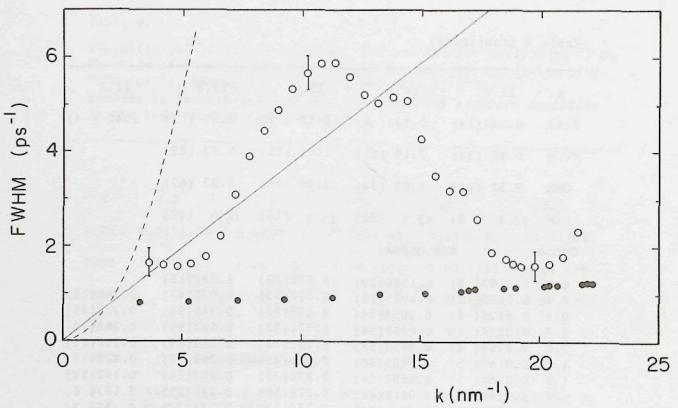

Fig.21. FWHM of $S(k,\omega)$ at 844 bar (open circles), of the experimental resolution function (dots), of $S_f(k,\omega)$ (solid line) and of $S(k,\omega)$ in the hydrodynamic limit (dashed line).

The Full Width at Half Maximum (FWHM) of $S(k,\omega)$ is given in fig.21, together with the FWHM of the resolution on ω-scale. At $k \sim 5$ nm^{-1} and at $k \sim 20$ nm^{-1} the two quantities are approximately equal and consequently the resolution correction is important around these values of k. Within the k-range of the spectrometer the measured FWHM deviates from its hydrodynamic limit, which is equal to $2ak^2$, since the contribution of the sound modes to the FWHM is negligible in this limit (a is the thermal diffusivity; see eq.5 and table 6). Around $k \approx 10$ nm^{-1} the FWHM exceeds significantly the value for the free gas. The measured FWHM divided by the free-gas value is given in fig.22 and compared with the results from the IN-4 measurements at 20 bar. The variation of FWHM with k increases if pressure is applied.

The value at $\omega = o$ is given in fig.12. The result of dividing $S(k,\omega=o)$ at 844 bar by the structure factor $S(k)$ and by $S(k,\omega=o)$ for the free gas is given in fig.22 and compared with this quantity obtained from the IN-4 measurement at 20 bar. Very large differences occur around $k \approx 10$ nm^{-1} (decrease of 40% with respect to 20 bar) and around $k \approx 20$ nm^{-1} (increase of 60% with respect to 20 bar).

Fig.22. FWHM of $S(k,\omega)$ divided by FWHM of $S_f(k,\omega)$ at 20 bar (IN-4 data; dots) and at 844 bar (RKS-1 data; open circles); value at $\omega=0$ of $S(k,\omega)$ divided by $S(k)$ and by $S_f(k,\omega=0)$ at 20 bar (dots) and at 844 bar (open circles).

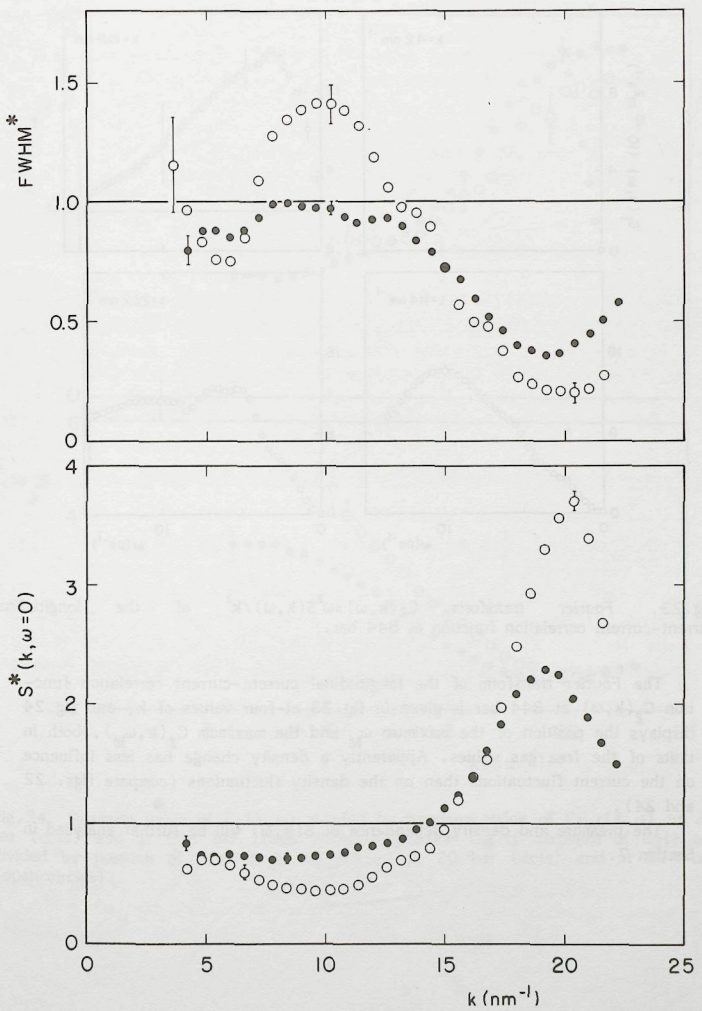

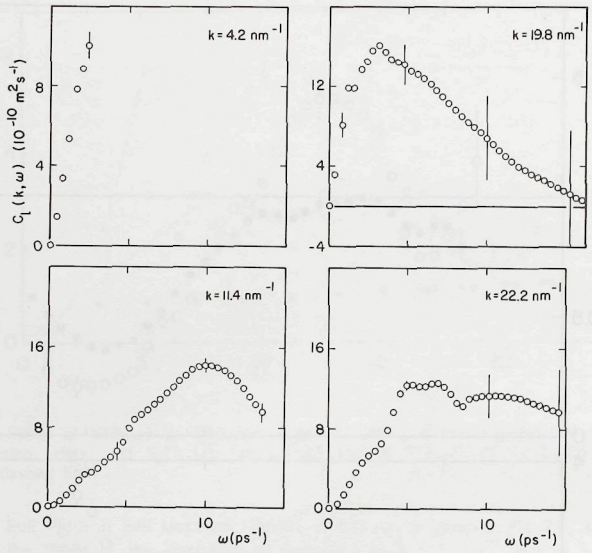

Fig.23. Fourier transform $C_\ell(k,\omega)=\omega^2 S(k,\omega)/k^2$ of the longitudinal current-current correlation function at 844 bar.

The Fourier transform of the longitudinal current-current correlation function $C_\ell(k,\omega)$ at 844 bar is given in fig.23 at four values of k, and fig.24 displays the position of the maximum ω_M and the maximum $C_\ell(k,\omega_M)$, both in units of the free gas values. Apparently a density change has less influence on the current fluctuations than on the density fluctuations (compare figs. 22 and 24).

The pressure and density dependence of $S(k,\omega)$ will be further analysed in Section 7.

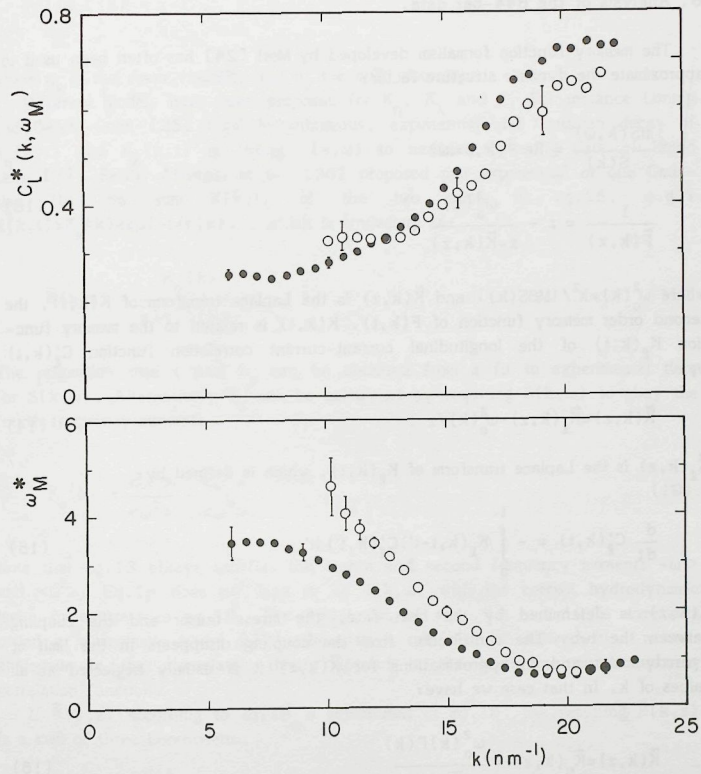

Fig.24. Maximum value of $C_\ell(k,\omega)$ divided by maximum value of $C_{\ell,f}(k,\omega)$ at 20 bar (dots) and at 844 bar (open circles); position ω_M of maximum of $C_\ell(k,\omega)$ divided by position of maximum of $C_{\ell,f}(k,\omega)$ at 20 bar (dots) and at 844 bar (open circles).

6. Analysis of the 844-bar data.

The memory function formalism developed by Mori [24] has often been used to approximate the dynamic structure factor:

$$\frac{\pi S(k,\omega)}{S(k)} = \mathrm{Re}\,\tilde{F}(k,z=i\omega)$$

$$\frac{1}{\tilde{F}(k,z)} = z + \frac{\omega_0^2(k)}{z+\tilde{K}(k,z)} , \qquad (13)$$

where $\omega_0^2(k)=k^2/(M\beta S(k))$ and $\tilde{K}(k,z)$ is the Laplace transform of $K(k,t)$, the second order memory function of $F(k,t)$. $K(k,t)$ is related to the memory function $K_\ell(k,t)$ of the longitudinal current-current correlation function $C'_\ell(k,t)$ by:

$$\tilde{K}(k,z)=\tilde{K}_\ell(k,z)-\omega_0^2(k)/z . \qquad (14)$$

$\tilde{K}_\ell(k,z)$ is the Laplace transform of $K_\ell(k,t)$, which is defined by:

$$\frac{d}{dt} C'_\ell(k,t) = -\int_0^t K_\ell(k,t-t')C'_\ell(k,t')dt' . \qquad (15)$$

$\tilde{K}(k,z)$ is determined by the heat flux, the stress tensor and the coupling between the two. The contribution from the coupling disappears in the limit of hydrodynamics and in approximations for $\tilde{K}(k,z)$ it is usually neglected at all values of k. In that case we have:

$$\tilde{K}(k,z)=\tilde{K}_\eta(k,z) + \frac{\omega_0^2(k)\Gamma(k)}{z+\tilde{K}_\lambda(k,z)} \qquad (16)$$

and $S(k,\omega)$ has the correct hydrodynamic limit (eq.5) if

$$\lim_{z\to 0}\lim_{k\to 0}\frac{\tilde{K}_\eta(k,z)}{k^2} = \frac{\frac{4}{3}\eta_s+\eta_v}{M\rho} ,$$

$$\lim_{z\to 0}\lim_{k\to 0}\frac{\tilde{K}_\lambda(k,z)}{k^2} = \gamma a = \frac{\lambda}{\rho C_v} , \qquad (17)$$

$$\lim_{k\to 0}\Gamma(k) = \gamma-1 ,$$

where η_s is the shear viscosity and η_v the bulk viscosity.

Different models have been proposed for K_η, K_λ and Γ. For instance Lonngi and García-Colín [25] tried instantaneous, exponential and Gaussian decay of $K_\eta(k,t)$ and $K_\lambda(k,t)$ in fitting $S(k,\omega)$ to neutron scattering data of liquid neon [7]. Earlier Ailawadi et al. [26] proposed one exponential or one Gaussian for the sum $K(k,t)$ of the two terms in eq.16, e.g.: $K(k,t)=K_0(k)\exp\{-t/\tau(k)\}$, which is equivalent to:

$$\tilde{K}(k,z) = \frac{K_0(k)}{z+\tau^{-1}(k)} . \qquad (18)$$

The relaxation time τ and K_0 can be obtained from a fit to experimental data for $S(k,\omega)$. Alternatively K_0 can be calculated by requiring $S(k,\omega)$ to obey the fourth frequency moment:

$$K_0(k) = \frac{\langle\omega^4\rangle}{\langle\omega^2\rangle} - \frac{\langle\omega^2\rangle}{\langle\omega^0\rangle} . \qquad (19)$$

Note that eq.13 always satisfies the zeroth and second frequency moments $\langle\omega^0\rangle$ and $\langle\omega^2\rangle$. Eq.18 does not lead to an $S(k,\omega)$ with the correct hydrodynamic limit, in contrast to eq.16. The combination of eqs. 18 and 19 is sometimes called a viscoelastic model [27], because it can also be derived in a manner analogous to the viscoelastic theory applied to the transverse current-current correlation function.

If $\tilde{K}(k,z)$ according to eq.18 is substituted in eq.16, the resulting $\tilde{F}(k,z)$ is a sum of three Lorentzians:

$$\tilde{F}(k,z) = \sum_{j=0,\pm 1} \frac{A_j}{z+w_j} , \qquad (20)$$

with A_0 and w_0 real and A_{+1} and w_{+1} either real or complex conjugated pairs: $A_{-1}=A^*_{+1}$ and $w_{-1}=w^*_{-1}$. Identifying eq.20 with eq.13, where eq.18 has been substituted, leads to the following relations between the parameters:

$$w_0+w_{-1}+w_{+1} = \tau^{-1} ,$$

$$w_0w_{-1}+w_0w_{+1}+w_{-1}w_{+1} = \omega_0^2+K_0 ,$$

$$w_0w_{-1}w_{+1} = \omega_0^2\tau^{-1} ,$$

$$A_0+A_{-1}+A_{+1} = 1 , \qquad (21)$$

$$A_0(w_{-1}+w_{+1}) + A_{-1}(w_0+w_{+1}) + A_{+1}(w_0+w_{-1}) = \tau^{-1} ,$$

$$A_0 w_{-1}w_{+1} + A_{-1} w_0w_{+1} + A_{+1}w_0w_{-1} = K_0 .$$

If the last two equations are replaced by:

$$A_0w_0 + A_{-1}w_{-1} + A_{+1}w_{+1} = 0 ,$$

$$A_0w_0^3 + A_{-1}w_{-1}^3 + A_{+1}w_{+1}^3 = 0 , \qquad (21a)$$

the resulting set of six equations has the same solution for w_j and A_j, $j = 0, \pm 1$. This means that a sum of three Lorentzians is equivalent with the simple exponential model eq.18, if this sum satisfies the sum rules:

$$\sum_j A_j w_j^n = 0 \text{ for } n = 1,3 .$$

Consequently, $S(k,\omega)$ according to the simple exponential model (eq.18) satisfies the zeroth and second frequency moment and has zero first and third sum rule (see also ref. 2), which reduces the number of six independent parameters in eq.20 to only two. The same result has been derived by Lovesey in a somewhat different manner [28].

Eq. 20 is identical to a model proposed by de Schepper and Cohen [29]. This model is consistent with the limit of linear hydrodynamics if the restriction of a zero third sum rule (second relation in eq.21a) is removed. A non-zero third sum rule implies a divergent fourth frequency moment. If we require $S(k,\omega)$, following from eq.20, to have the correct limit of hydrodynamics and correct frequency moments up to and including the fourth, eq.20 must be extended with two terms: $A_{\pm 2}/(z+w_{\pm 2})$.

Eq. 20 was fitted by means of the weighted least squares method to the present data for $S(k,\omega)$ of liquid argon at 120 K and 844 bar with respectively 4, 3 and 2 sum rules:

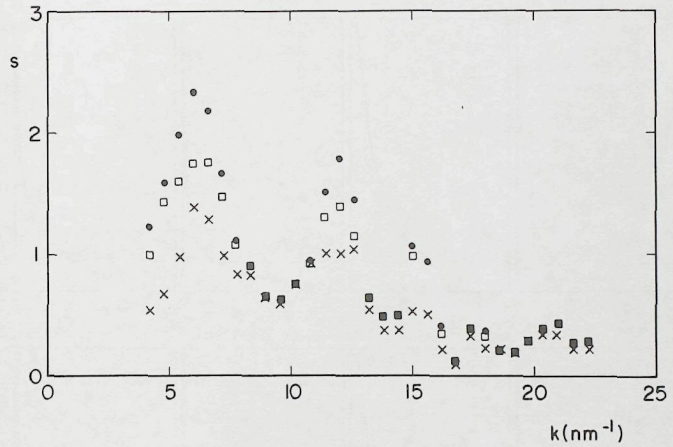

Fig.25. Root mean square error of least squares fit of sum of three Lorentzians to experimental data at 844 bar. Dots: four sum rules (n=1-4); squares: three sum rules (n=1-3); crosses: two sum rules (n=1,2).

model 1 satisfying $\sum_j A_j w_j = 0$,

$$\sum_j A_j w_j^2 = -\omega_0^2 ,$$

$$\sum_j A_j w_j^3 = 0 ,$$

$$\sum_j A_j w_j^4 = \langle\omega^4\rangle / S(k) ,$$

which is identical to the simple exponential model with $K_0(k)$ determined by $\langle\omega^4\rangle$, which was calculated as indicated in appendix B;
model 2 satisfying the first three of the sum rules mentioned above and
model 3 satisfying the first two.
Only model 3 is consistent with linear hydrodynamics. $S(k)$ was regarded as an adjustable parameter in all three models. More details of the fitting procedure are given in appendix C.

The root mean square error s resulting from these three fits is given in fig.25. s is defined by:

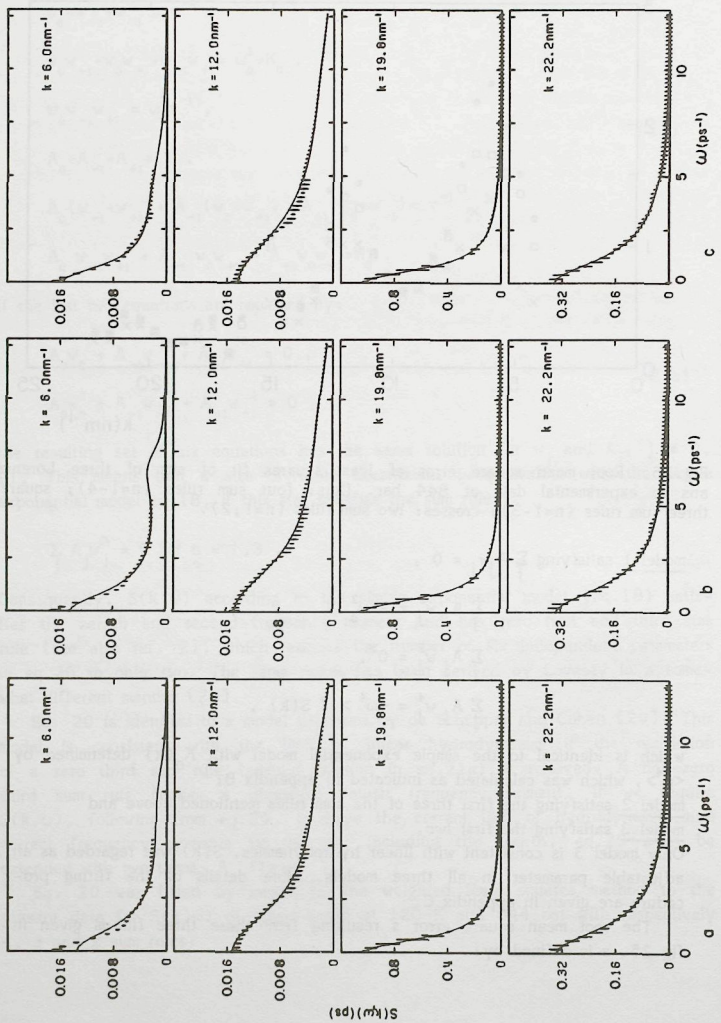

Fig.26. Experimental $S(k,\omega)$ (error bars) and fitted sum of three Lorentzians (solid line). a: four sum rules (n=1-4); b: three sum rules (n=1-3); c: two sum rules (n=1,2).

$$s^2 = \frac{1}{N-p} \sum_{j=1}^{N} \left[\frac{Y_j - f_j}{\sigma_j} \right]^2 ,$$

where N is the number of data points at a particular value of k, p the number of independent parameters, Y_j the experimental data for $S(k,\omega_j)$, f_j the model at (k,ω_j) and σ_j the estimated standard deviation of the error of the experimental data. We cannot expect $s^2(N-p)$ to follow a χ^2-distribution, because the data Y_j are correlated and probably not normally distributed, which makes $s < 1$ acceptable.

Some examples of the fits are shown in fig.26. The differences between the three models are not large for $12 \lesssim k \lesssim 22$ nm^{-1}. The fact that model 1 and model 2 have the wrong hydrodynamic limit may explain the bad fit at $k = 6$ nm^{-1}. Model 3 has a non-zero third sum rule and consequently a divergent fourth frequency moment. Nevertheless the root mean square error s of the fit of model 3 is for all k in the range 4.2 to 22.2 nm^{-1} smaller than or equal to the value of s of the fit of model 1, which has the correct fourth frequency moment. Moreover in fig.26 it can be seen that model 3 fits nearly perfectly to the experimental data. This means that the present experimental data *contain hardly any significant information on the fourth frequency moment*, because the error at large ω is too great. A correct hydrodynamic limit is more important than a correct fourth frequency moment for a description of the data. One memory function for the combined heat flux and stress tensor with a fixed value of the fourth frequency moment leads to bad fits at $k > 22$ nm^{-1}, as has been shown by Rowe and Sköld [30] and by de Schepper et al. [31].

From the fits with model 2 and 3 the dispersion curve for the generalized sound propagation mode (see ref. 2) has been determined and is given in fig.27. The bars connect the data for $\omega_s = \mathrm{Im}\, w_{+1} = -\mathrm{Im}\, w_{-1}$ from the fit with model 2 and 3 respectively. For $k \leq 10$ nm^{-1} there is no significant deviation from the hydrodynamic limit $\omega_s = c_s k$. It has been suggested [2] that the position ω_M of the maximum of the Fourier transform of the longitudinal current-current correlation function $C_l(k,\omega) = \omega^2 S(k,\omega)/k^2$ is related to the generalized sound dispersion ω_s. Indeed in the present case there is no significant difference between ω_s and ω_M at $10.2 \leq k \leq 22.2$ nm^{-1} (see fig.27). For comparison also the mean frequency ω_I of the response spectrum of the fluid to an external probe is given. Egelstaff defines ω_I as [32]:

$$\omega_I = \int_0^\infty \omega\, S_I(k,\omega)d\omega \Big/ \int_0^\infty S_I(k,\omega)d\omega \ , \qquad (22)$$

where $S_I(k,\omega)=0.5\ \{S(k,\omega)-S(k,-\omega)\}$. $S_I(k,\omega)$ is the Fourier transform of the imaginary part of the Van Hove function and describes the disturbance of the fluid produced by a probe, e.g. a neutron [33]. For k around 10 nm^{-1} the response frequency is significantly lower than the generalized sound frequency. The present theoretical knowledge is not sufficient to provide an explanation for the difference between ω_I and ω_s.

It is noteworthy that the sound propagation gap, found earlier in the IN-4 data at lower densities [2,34], is absent in the present results. This might be due to the fact that the experimental errors in the RKS-1 data are larger than in the IN-4 data. Therefore models 2 and 3 were also fitted to the RKS-1 data at 20 bar in order to check whether the gap found in the IN-4 data at 20 bar around k = 20 nm^{-1} would reproduce. Fig.28 demonstrates that this is indeed the case. Also it can be seen that the uncertainty in the dispersion of

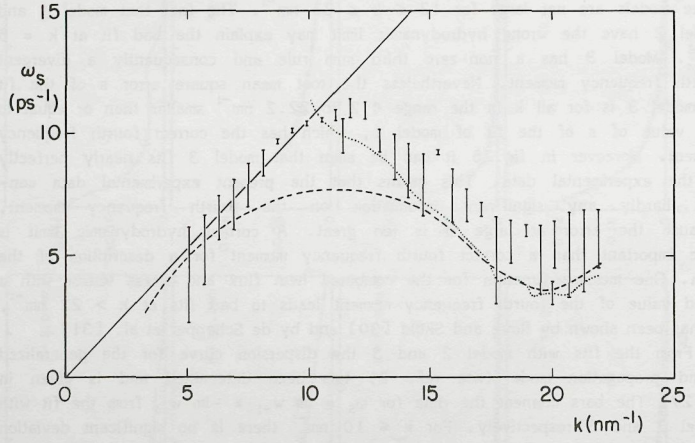

Fig.27. Dispersion relations in argon at 120 K and 844 bar. Dotted line: ω_M (with the estimated standard deviation indicated by bars at k=11.4 and 20.0 nm^{-1}); dashed line: ω_I, eq. 22; solid line: $c_s k$; the remaining error bars connect the values of ω_s from a fit of a sum of three Lorentzians with three (n=1-3) and with two (n=1,2) sum rules.

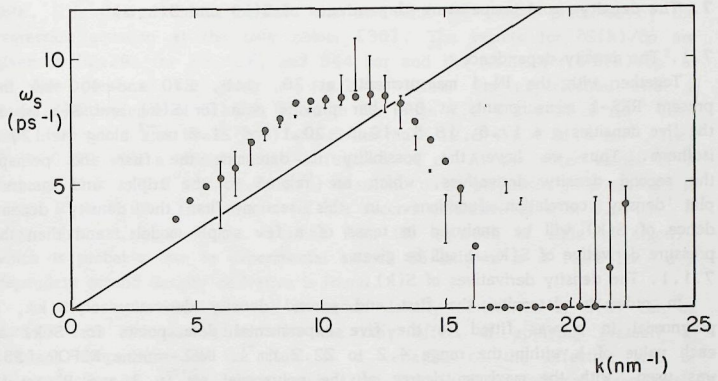

Fig.28. Extended sound dispersion in liquid argon at 120 K and 20 bar, as determined from the IN-4 measurements (dots) and from the RKS-1 measurements (error bars have the same meaning as in fig. 27). Solid line: $c_s k$.

the RKS-1 data is larger than of the IN-4 data. The (conservative) conclusion is that the present results for liquid argon at 120 K suggest that the sound propagation gap disappears at high densities before solidification is reached. Confirmation by means of more accurate measurements at high pressure and by means of computer simulations is necessary.

$$\rho^2 \left[\frac{\partial^2 S(k)}{\partial \rho^2}\right]_T = \frac{k}{9}\left\{ k \left[\frac{\partial^2 S(k)}{\partial k^2}\right]_{\rho,T} + 4 \left[\frac{\partial S(k)}{\partial k}\right]_{\rho,T} \right\} . \qquad (24)$$

Egelstaff *et al.* [37] expected this model to be reasonable for dense systems. For the first derivative they find excellent agreement with their experimental data in liquid rubidium, they find some discrepancies for liquid lead and strong discrepancies for argon near its triple point. The conclusions on liquid rubidium have been confirmed by more accurate measurements by Egelstaff et al. [39] in 1980. Egelstaff and Wang [38] deduce the second density derivative from the data on liquid neon at 35 K and the three densities ρ = 31.69, 33.38 and 34.66 nm^{-3}. Compared with eq.24 the order of magnitude is correct, but the sign is wrong.

In order to obtain $\partial S(k)/\partial k$ and $\partial^2 S(k)/\partial k^2$ from the present data, a smooth spline [35,40] was fitted to the experimental S(k) at each of the five densities for $4.2 \leq k \leq 22.2$ nm^{-1}. The right-hand sides of eqs. 23 and 24 can then be calculated at any k within this range. Some results are displayed in figs.30 and 31. In fig.30 the experimental data for $\partial S(k)/\partial \rho$ at 20 and 844 bar are compared with eq.23. The agreement is only qualitative and does not improve with increasing density, contrary to what Egelstaff et al. [37] suggest. The second density derivative according to eq.24 is tested in fig.31 against the experimental data. Again the agreement is qualitative and certainly not as bad as Egelstaff and Wang [38] find for liquid neon. Note however that the depth of the minimum of $\partial^2 S(k)/\partial \rho^2$ increases with density according to eq.24, which is in disagreement with the experimental data (fig.29b).

Next a simple model for the time-independent triplet correlation function will be tested. From eq.8 the following relation for g(r) can be derived:

$$\rho\, S(0) \left[\frac{\partial g(r)}{\partial \rho}\right]_T = \rho \int [\, g_3(\vec{r},\vec{s}) - g(r)\,]\, d\vec{s} + 2\,\{\, 1 - S(0)\,\}\, g(r) , \qquad (25)$$

where g_3 is defined analogous to the definition of g(r) as:

$$g_3(\vec{r},\vec{s}) = \frac{1}{\rho^3} < \sum_{i} \sum_{j \neq i} \sum_{k \neq i} \delta(\vec{R}_i)\, \delta(\vec{r} - \vec{R}_j)\, \delta(\vec{s} - \vec{R}_k) > .$$

Fig.30. Experimental isothermal pressure derivative of S(k) (dots) compared with the Winfield-Egelstaff approximation eq. 29c (solid line) and with the uniform-fluid model derived from eq. 23 (dashed line). a: 20 bar; b: 844 bar.

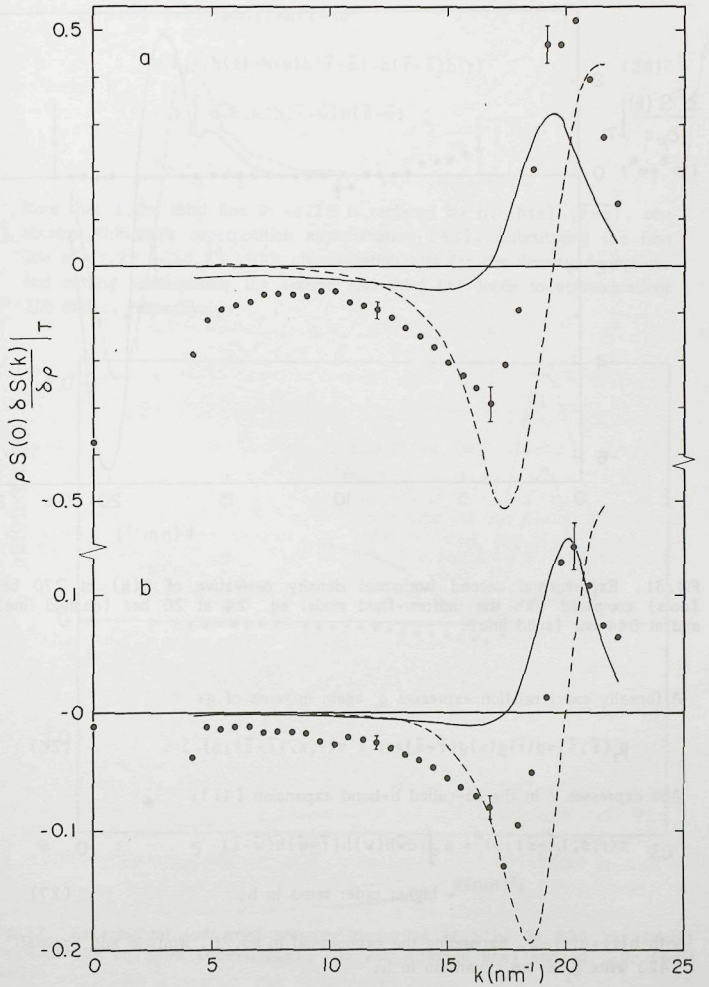

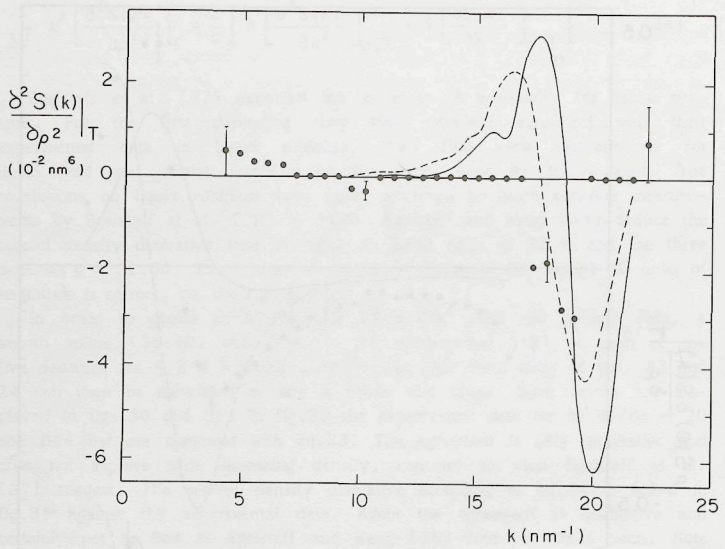

Fig. 31. Experimental second isothermal density derivative of S(k) at 270 bar (dots) compared with the uniform-fluid model eq. 24 at 20 bar (dashed line) and at 844 bar (solid line).

A formally exact relation expresses g_3 again in terms of g:

$$g_3(\vec{r},\vec{s}) = g(r)g(s)g(\vec{r}-\vec{s})\exp\,[\,\tau(r,s,|\vec{r}-\vec{s}|;\rho)\,]\,. \qquad (26)$$

Abe expresses τ in the so-called h-bond expansion [41]:

$$\tau(r,s,|\vec{r}-\vec{s}|;\rho) = \rho\int d\vec{w}\,h(w)h(\vec{r}-\vec{w})h(\vec{w}-\vec{s}) + \text{higher order terms in h}, \qquad (27)$$

with $h(r)=g(r)-1$. Expanding the exponential in eq.26, Winfield and Egelstaff [42] write g_3 as an expansion in h:

$$g_3(\vec{r},\vec{s}) = 1+h(r)+h(s)+h(\vec{r}-\vec{s}) + h(r)h(s)+h(s)h(\vec{r}-\vec{s})+h(\vec{r}-\vec{s})h(r) + \rho\int d\vec{w}\,h(w)h(\vec{r}-\vec{w})h(\vec{s}-\vec{w}) + \ldots. \qquad (28)$$

Note that if the third line in eq.28 is replaced by $h(r)h(s)h(\vec{r}-\vec{s})$, one obtains Kirkwood's superposition approximation [43]. Substituting the first line of eq.28 in eq.25 yields approximation 29a for the density derivative, and adding subsequently the second and third line leads to approximations 29b and c, respectively:

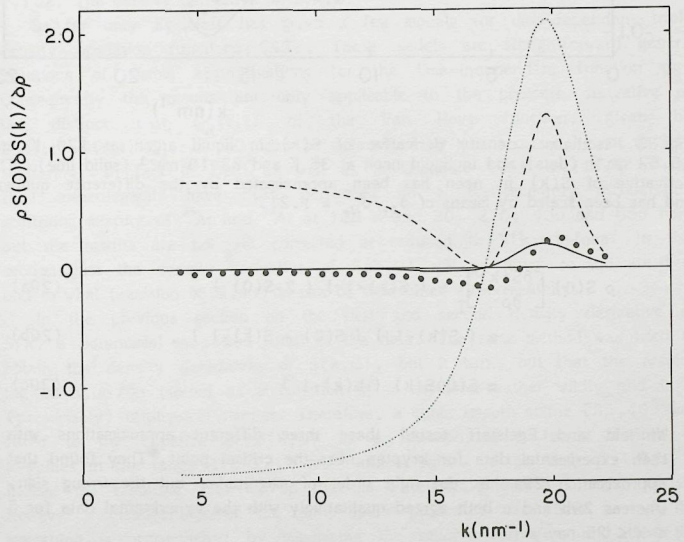

Fig. 32. Experimental isothermal pressure derivative of S(k) at 270 bar (dots) compared with eq. 29a (dotted line), eq. 29b (dashed line) and eq. 29c (solid line).

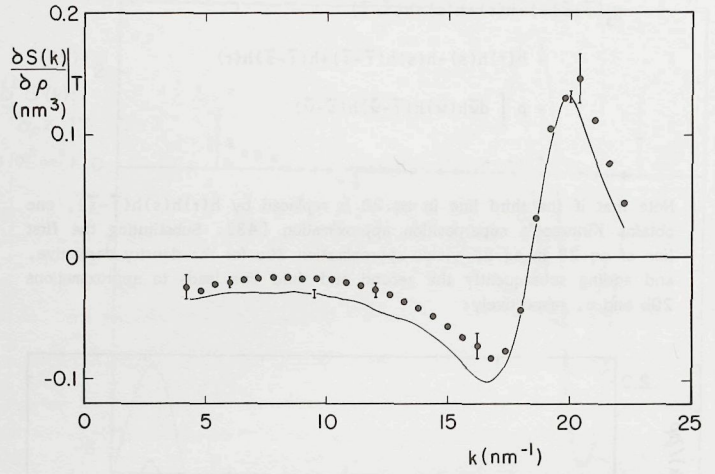

Fig.33. Isothermal density derivative of S(k) in liquid argon at 120 K and 18.52 nm^{-3} (dots) and in liquid neon at 35 K and 33.18 nm^{-3} (solid line). The derivative of S(k) in neon has been approximated by the difference quotient and has been scaled by means of $\sigma_{Ar}/\sigma_{Ne} = 1.21$.

$$\rho\, S(0) \left[\frac{\partial S(k)}{\partial \rho}\right]_T \approx \{\, S(k)-1 \,\}\, \{\, 2-S(0) \,\}\,, \qquad (29a)$$

$$\approx \{\, S(k)-1 \,\}\, \{\, S(0) + S(k)-1 \,\}\,, \qquad (29b)$$

$$\approx S(0)S(k)\, \{\, S(k)-1 \,\}\,. \qquad (29c)$$

Winfield and Egelstaff tested these three different approximations with their experimental data for krypton near the critical point. They found that approximation 29a has the right order of magnitude, but the wrong sign, whereas 29b and c both agreed qualitatively with the experimental data for $5 \lesssim k \lesssim 25$ nm^{-1}.

Approximation 29c is compared with the present experimental data at 20 and 844 bar in fig.30. The three approximations 29a, b and c are displayed in fig.32 for 270 bar. Apparently contributions of the three individual lines in eq.28 are large compared to their sum and cancel each other largely. Evidently approximations 29a and b are useless in the liquid state.

In summary, the present data for S(k) in liquid argon at 120 K and at five densities in the range 17.6-21.6 nm^{-3} cannot be explained by the simple models discussed in this section. Recently Haymet et al. [44] evaluated eq.26 including the second term of the h-bond expansion. They find excellent agreement with g_3 obtained from computer simulations of liquid sodium, but only qualitative agreement with the neutron diffraction data for liquid neon at 35 K by De Graaf and Mozer [12]. The difference between the present data for $\rho\partial S(k)/\partial\rho$ and those by De Graaf and Mozer (fig.33) is of the same order of magnitude as the discrepancy between the calculations by Haymet et al. and the neon data. Therefore it would be interesting to compare the calculated density derivative of S(k) according to Haymet et al. with the present experimental data. However, this requires extensive calculations and will not be done here.

7.1.2. The density derivative of $S(k,\omega)$

So far only Egelstaff has given a few models for time-dependent triple density-correlation functions [45]. These models are straightforward generalizations of simple approximations for the time-independent function g_3. Consequently the results are only applicable to the pressure derivative of the distinct part $G_d(r,t)$ of the Van Hove function, given by $G_d(r,t)=G(r,t)-G_s(r,t)$. G_s can be determined by means of incoherent neutron scattering. In fact in Delft as well as in Grenoble (with the IN-4 of the ILL) measurements have been performed on a predominantly incoherently scattering mixture of ^{36}Ar and ^{40}Ar at 120 K and 20, 270, 400 and 850 bar, but the results are not yet corrected or reduced to $S(k,\omega)$-form. In this section just the density derivative of $S(k,\omega)$ will be given to indicate how and to what precision $\partial S(k,\omega)/\partial\rho$ can be determined experimentally.

In the previous section on the first and second density derivative of S(k) a polynomial in ρ was fitted to the data. The same method was tried to obtain the density derivatives of $S(k,\omega)$, but it turns out that the resulting $\partial S(k,\omega)/\partial\rho$ plotted as a function of ω oscillates rather wildly and in a (presumably) unphysical manner. Therefore, a cubic smooth spline [35,40] was fitted to the experimental $S(k,\omega)$ as a function of ρ for a number of k-values in the range 4.2-22.2 nm^{-1} and ω-values in the range 0-13 ps^{-1}. Indeed the resulting $\partial S(k,\omega)/\partial\rho$ then is a relatively smooth function of ω. However a disadvantage of the cubic spline procedure used here is that the smoothing is accomplished by minimizing the second derivative and that the second derivative is set to zero at the first and last data point (of a total of only five in this case). This results in a biased second derivative and therefore no efforts were made to determine $\partial^2 S(k,\omega)/\partial\rho^2$.

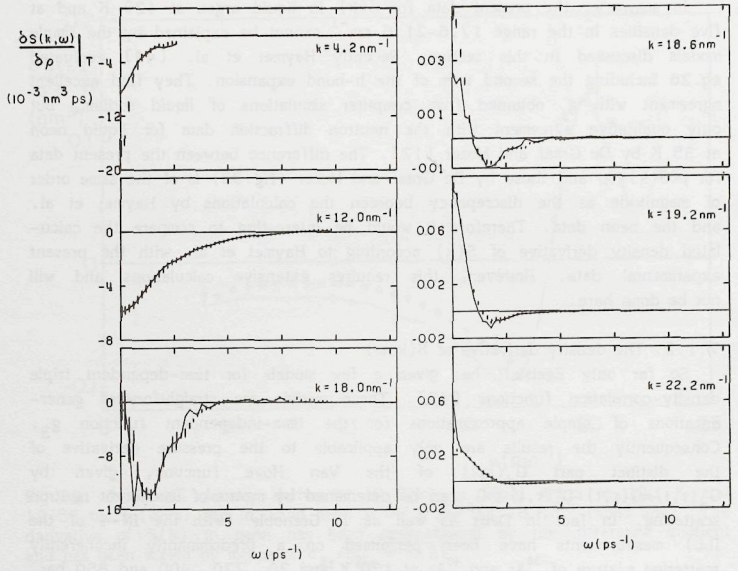

Fig.34. Isothermal density derivative of $S(k,\omega)$ at 115 bar (error bars) and at 400 bar (solid lines).

In fig.34 $\partial S(k,\omega)/\partial\rho$ is given for 115 and 400 bar. The isothermal pressure derivative is proportional to the isothermal density derivative according to

$$\rho k_B T \left[\frac{\partial S(k,\omega)}{\partial P}\right]_T = \rho S(0) \left[\frac{\partial S(k,\omega)}{\partial \rho}\right]_T .$$

This quantity has the same dimension as $S(k,\omega)$ and as can be seen from fig.35 also the same order of magnitude for most values of k. Furthermore it can be seen that the derivative of $S(k,\omega)$ is a damped oscillating function of ω. For $k \lesssim 18$ nm^{-1} $\partial S(k,\omega)/\partial P$ is negative at $\omega=0$, and for $18 \lesssim k \lesssim 22.2$ nm^{-1} $\partial S(k,\omega)/\partial P$ is positive at $\omega=0$, the change of sign around $k = 18$ nm^{-1}

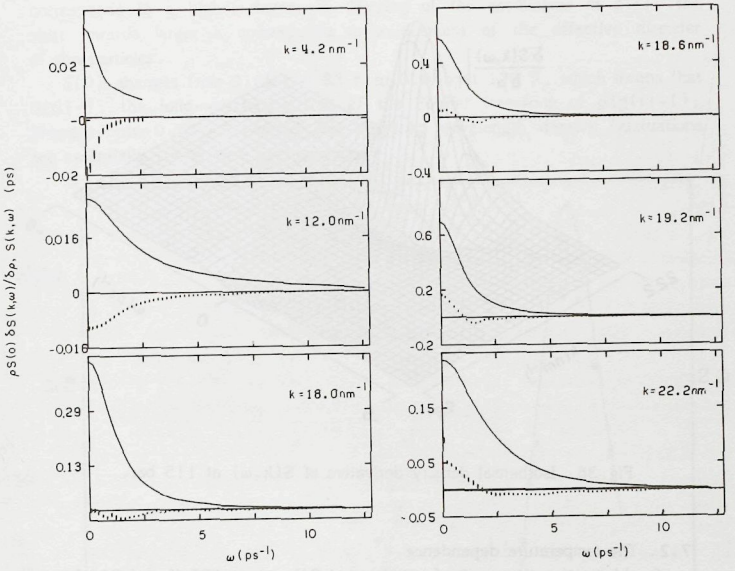

Fig.35. $S(k,\omega)$ (solid line) and isothermal pressure derivative of $S(k,\omega)$ (error bars) in liquid argon at 120 K and 270 bar.

being relatively abrupt. This behaviour of $\partial S(k,\omega)/\partial P$ is in agreement with the results of Groome et al. [46], who calculated from kinetic theory the pressure derivative of $S(k,\omega)$ for liquid argon near its triple point.

The features of $\partial S(k,\omega)/\partial P$ mentioned here can also be seen in the three-dimensional plot in fig.36.

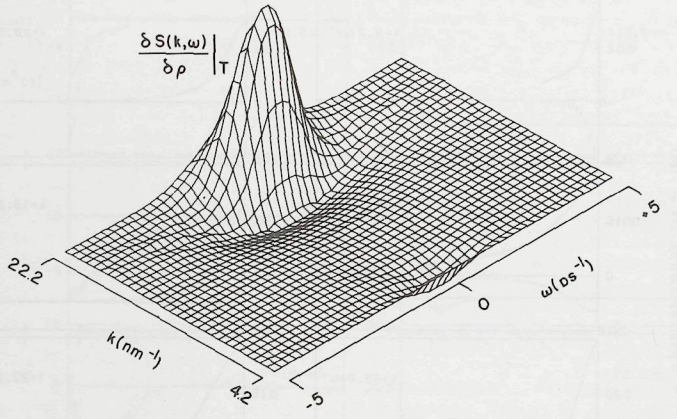

Fig.36. Isothermal density derivative of $S(k,\omega)$ at 115 bar.

7.2. The temperature dependence

In this section the results for $S(k)$ and $S(k,\omega)$ at 120 K and 844 bar will be compared with the neutron diffraction data by Yarnell et al. [10] at 85 K and at saturated vapour pressure and with the inelastic neutron scattering data by Sköld et al. [3] at 85.2 K and at saturated vapour pressure. The density of 21.2 nm^{-3} at 85 K and saturated vapour pressure differs only 2% from the density of 21.6 nm^{-3} at 120 K and 844 bar, so that the effect of changing the temperature at constant density on $S(k)$ and $S(k,\omega)$ can be studied.

The temperature derivative at constant density is according to eq.9 related to the energy-density-particle-density triplet correlation function. As there is no theory in the literature available for this correlation function, eq.9 cannot be used and the experimental data at the two temperatures are compared with each other to draw a few qualitative conclusions.

The structure factors at 85 and 120 K are given in fig.37. Increasing the temperature from 85 K to 120 K decreases the height of the main peak with 12% and shifts its position with 0.3 nm^{-1} towards larger k. This can be qualitatively understood from the fact that at the lower temperature the particles remain on the average deeper in the potential well of their mutual interaction, thus being more localized. A decrease of the main peak of $S(k)$

corresponds to a higher degree of damping of the oscillations in $g(r)$, the shift towards larger k corresponds to a decrease of the effective diameter of the particles.

$S(0)$ changes from 0.050 at 85 K to 0.045 at 120 K, which means that $S(0)-1$, the long-wavelength limit of the Fourier transform of $\rho\{g(r)-1\}$, changes only 0.5%, indicating that the long wavelength density fluctuations are essentially temperature independent.

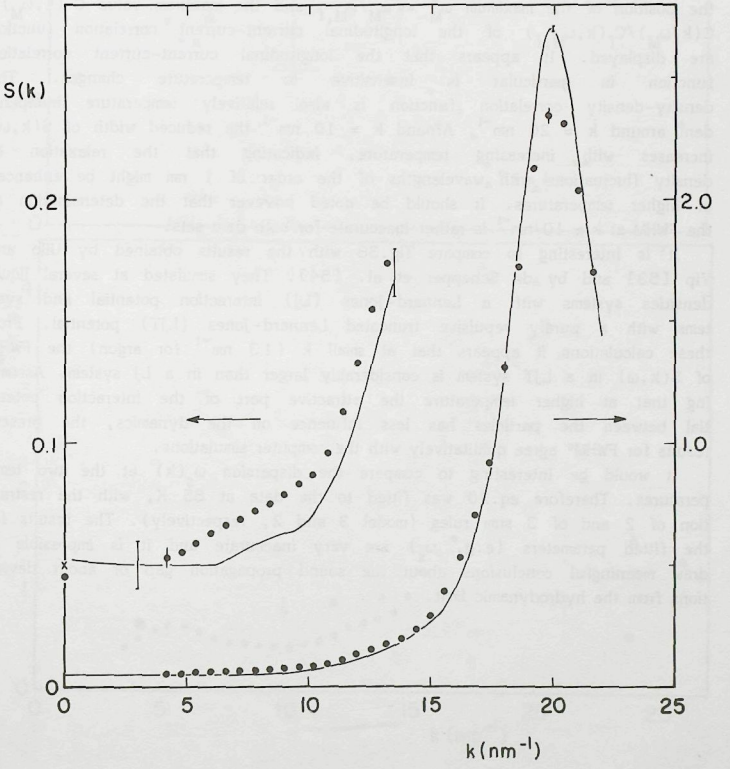

Fig.37. Structure factor in liquid argon at 120 K and 21.6 nm^{-3} (dots) and at 85 K and 21.2 nm^{-3} (solid line).

Regarding the influence of the temperature on the dynamics in a fluid, a first-order effect is due to the temperature dependence of the average kinetic energy per particle: $\langle \frac{1}{2}Mv^2 \rangle = \frac{3}{2}k_B T$. If time is measured in units which are proportional to $T^{-\frac{1}{2}}$, this effect is eliminated. This is, for instance, accomplished by measuring the dynamic quantities in free-gas units, as was also done in section 5. In fig.38 $FWHM^* = FWHM/FWHM_f$ and $S^*(k,0) = S(k,\omega=0)/\{ S(k)\ S_f(k,\omega=0)\}$ are given at both temperatures. In fig.39 the position of the maximum $\omega_M^* = \omega_M/\omega_{M,f}$ and the maximum value $C^*(k,\omega_M) = C(k,\omega_M)/C_f(k,\omega_{M,f})$ of the longitudinal current-current correlation are displayed. It appears that the longitudinal current-current correlation function in particular is insensitive to temperature changes. The density-density correlation function is also relatively temperature independent around $k = 20\ nm^{-1}$. Around $k = 10\ nm^{-1}$ the reduced width of $S(k,\omega)$ increases with increasing temperature, indicating that the relaxation of density fluctuations with wavelengths of the order of 1 nm might be enhanced at higher temperatures. It should be noted however that the determination of the FWHM at $k \approx 10\ nm^{-1}$ is rather inaccurate for both data sets.

It is interesting to compare fig.38 with the results obtained by Ullo and Yip [53] and by de Schepper et al. [54]. They simulated at several liquid densities systems with a Lennard-Jones (LJ) interaction potential and systems with a purely repulsive truncated Lennard-Jones (LJT) potential. From these calculations it appears that at small k ($13\ nm^{-1}$ for argon) the FWHM of $S(k,\omega)$ in a LJT system is considerably larger than in a LJ system. Assuming that at higher temperature the attractive part of the interaction potential between the particles has less influence on the dynamics, the present results for $FWHM^*$ agree qualitatively with the computer simulations.

It would be interesting to compare the dispersion $\omega_s(k)$ at the two temperatures. Therefore eq.20 was fitted to the data at 85 K, with the restriction of 2 and of 3 sum rules (model 3 and 2, respectively). The results for the fitted parameters (e.g. ω_s) are very inaccurate and it is impossible to draw meaningful conclusions about the sound propagation gap or about deviations from the hydrodynamic limit.

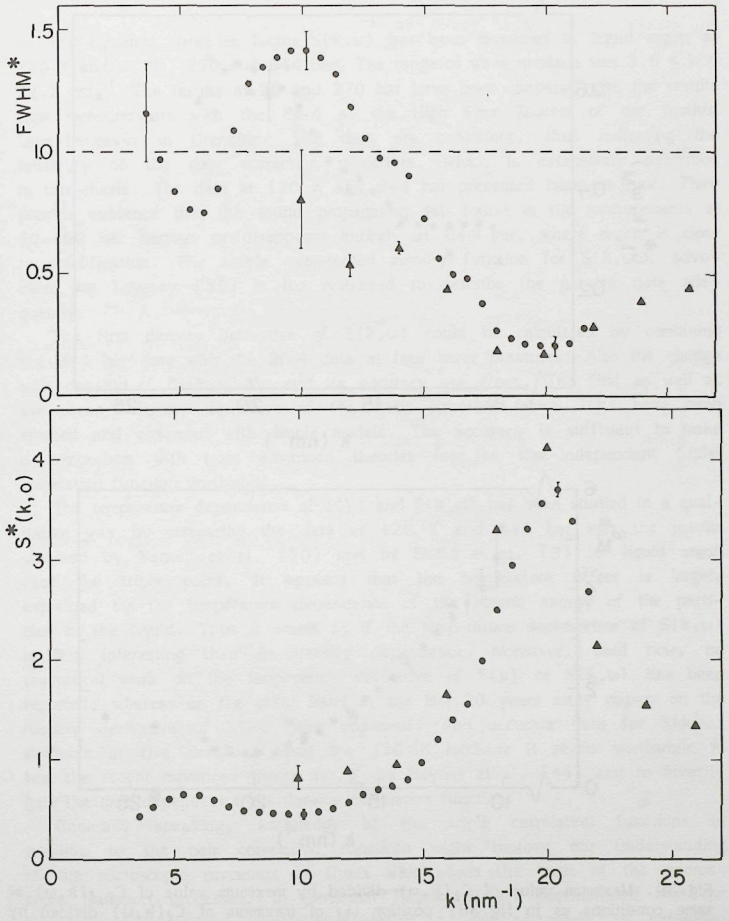

Fig.38. FWHM of $S(k,\omega)$ divided by FWHM of $S_f(k,\omega)$ in liquid argon at 120 K and 21.6 nm^{-3} (dots) and at 85.2 K and 21.2 nm^{-3} (triangles); value at $\omega=0$ of $S(k,\omega)$ divided by value at $\omega=0$ of $S_f(k,\omega)$ and by $S(k)$.

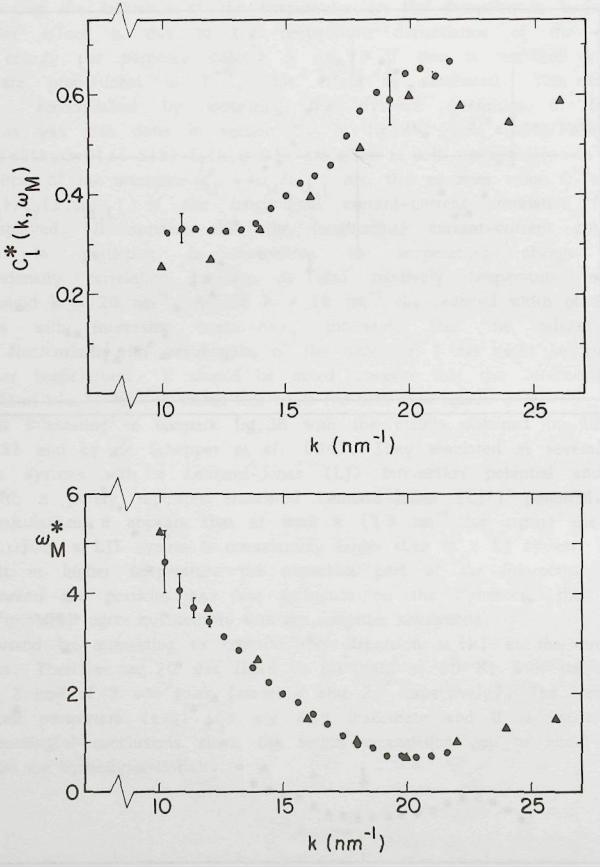

Fig.39. Maximum value of $C_{\ell}(k,\omega)$ divided by maximum value of $C_{\ell,f}(k,\omega)$ at same conditions as in fig.38; position ω_M of maximum of $C_{\ell}(k,\omega)$ divided by position of maximum of $C_{\ell,f}(k,\omega)$ at same conditions as in fig.38.

8. Conclusions.

The dynamic structure factor $S(k,\omega)$ has been measured in liquid argon at 120 K and at 20, 270 and 844 bar. The range of wave numbers was $3.6 \leq k \leq 22.2$ nm^{-1}. The results at 20 and 270 bar have been compared with the results from measurements with the IN-4 at the High Flux Reactor of the Institut Laue-Langevin in Grenoble. The data are consistent, thus indicating the reliability of the data correction procedure, which is extensively described in this thesis. The data at 120 K and 844 bar presented here are new. They provide evidence that the sound propagation gap found in the measurements at 20-400 bar narrows or disappears entirely at 844 bar, where argon is close to solidification. The simple exponential memory function for $S(k,\omega)$, advocated by Lovesey [55] is too restricted to describe the present data adequately.

The first density derivative of $S(k,\omega)$ could be calculated by combining the 844 bar data with the IN-4 data at four lower pressures. Also the change with density of $\partial S(k,\omega)/\partial\rho$ and its accuracy are given. The first as well as the second density derivative of the static structure factor $S(k)$ have been studied and compared with simple models. The accuracy is sufficient to make a comparison with more advanced theories for the time-independent triplet correlation function worthwhile.

The temperature dependence of $S(k)$ and $S(k,\omega)$ has been studied in a qualitative way by comparing the data at 120 K and 844 bar with the results obtained by Yarnell et al. [10] and by Sköld et al. [3] for liquid argon near the triple point. It appears that the temperature effect is largely explained by the temperature dependence of the kinetic energy of the particles in the liquid. Thus it seems as if the temperature dependence of $S(k,\omega)$ is less interesting than its density dependence. Moreover, until now, no theoretical work on the temperature derivative of $S(k)$ or $S(k,\omega)$ has been reported, whereas on the other hand in the last 20 years many papers on the density derivative of $S(k)$ have appeared. With accurate data for $S(k,\omega)$ available at five densities along the 120 K isotherm it seems worthwhile to test the recent advanced theory for g_3 by Haymet et al. [44] and to investigate the time-dependent triple density correlation functions.

Generally speaking, knowledge of the triple correlation functions in addition to the pair correlation functions might improve our understanding of the microscopic processes in fluids which form the basis of the macroscopic transport processes. In particular Haymet et al. demonstrated that the time-independent triplet correlation function g_3 can accurately be expressed in terms of the pair correlation function g, thus providing a closure for the Born-Green-Yvon hierarchy and leading to two equations for g and g_3 which actually can be solved numerically. The same procedure might be

applied to the time-dependent density correlation functions G and G_3. However, this would require extensive calculations due to the additional time variable. In addition to experimental data extensive computer simulations are needed.

Recently several computer simulations have been performed to investigate the influence of the shape of the particle interaction potential on the dynamics [53,54,56]. As indicated in the introduction and in section 7.2. additional information might be obtained from measurements of the temperature dependence of $S(k,\omega)$. In the high temperature limit the fluid is expected to be similar to a hard spheres system, whereas at low temperature the attractive well and other details of the interaction potential should be manifest. From the results and comparisons reported here it is clear that at the triple-point density a temperature change of 30-40% has little effect on the dynamics of collective density fluctuations.

To obtain relevant information from these small changes the experimental data should be considerably more accurate than the present data and the data by Sköld et al. On the other hand it might be worthwhile to measure the temperature dependence at a lower density, where the isochoric temperature derivative of the pressure is smaller than at triple-point density. In this way larger temperature changes within the same pressure range are possible. A third possibility might be to measure the temperature dependence in a fluid with a smaller well depth of the particle interaction potential, in order to obtain larger changes in $S(k,\omega)$ within the same temperature range (and at lower pressures).

Appendix A.

Stewart et al. [47] compiled many thermodynamic measurements on argon into one equation of state of the form:

$$\alpha(\delta,\tau) = \frac{A(\rho,T)}{RT} = \alpha^0(\tau) + \ell n\,\frac{\delta}{\delta^0} + \bar{\alpha}\,(\delta,\tau) \qquad (A1)$$

with $\delta = \rho/\rho_c$ reduced density
- ρ density
- ρ_c critical density (13.418 mol dm^{-3})
- T absolute temperature
- T_c critical temperature (150.69 K)
- $\tau = T_c/T$
- δ^0 reduced ideal gas density at pressure 1.01325 bar and at temperature T
- R molar gas constant (8.31434 J $mol^{-1}K^{-1}$)
- A Helmholtz function
- α^0 = the ideal gas reduced Helmholtz function for argon:

$$\alpha^0(\tau) = \frac{H_0^0\tau}{RT_c} - \frac{S_0^0}{R} + \frac{C_v^0}{R}\left[\,1 - \ell n\,\frac{T_0}{\tau}\,\right] \qquad (A2)$$

with H_0^0 reference enthalpy at T_0 = 298.15 K
- S_0^0 reference entropy at T_0 and P_0 = 1.01325 bar. (In ref.47 erroneously C_p^0 instead of C_v^0 is used).
- C_v^0 ideal-gas heat capacity ($\frac{3}{2}$ R)

$\bar{\alpha}(\delta,\tau)$ is given by Stewart et al. as a function with 34 constants. In ref.47 the term $N_{33}(\delta^3)(\tau^2)(EX)$ should read $N_{33}(\delta^2)(\tau^2)(EX)$.

From the Helmholtz function any thermodynamic quantity can be calculated by using derivatives of A with respect to V (=1/ρ) and to T. The thermodynamic quantities of interest in this work are

pressure: $P = -A_V$,

isothermal compressibility: $\rho\left(\frac{\partial P}{\partial \rho}\right)_T = VA_{VV}$,

heat capacity: $C_v = -T\,A_{TT}$,

ratio of heat capacities: $\gamma = \frac{C_p}{C_v} = 1 - \frac{A_{VT}^2}{A_{TT}A_{VV}}$,

adiabatic speed of sound: $c_s = V \left\{ \frac{1}{M} \frac{A_{TT}A_{VV} - A_{TV}^2}{A_{TT}} \right\}^{\frac{1}{2}}$

with M the molecular weight and

$$
\begin{aligned}
A_V &= \left(\frac{\partial A}{\partial V} \right)_T = - \rho RT \left(1 + \delta \frac{\partial \bar{\alpha}}{\partial \delta} \right) \\
A_{VV} &= \left(\frac{\partial^2 A}{\partial V^2} \right)_T = \frac{RT}{V^2} \left(1 + 2\delta \frac{\partial \bar{\alpha}}{\partial \delta} + \delta^2 \frac{\partial^2 \bar{\alpha}}{\partial \delta^2} \right) \\
A_{TT} &= \left(\frac{\partial^2 A}{\partial T^2} \right)_V = \frac{R}{T} \left(- \frac{3}{2} + \tau^2 \frac{\partial^2 \bar{\alpha}}{\partial \tau^2} \right) \\
A_{TV} &= A_{VT} = \frac{\partial^2 A}{\partial V \partial T} = - \frac{R}{V} \left(1 + \delta \frac{\partial \bar{\alpha}}{\partial \delta} - \partial \tau \frac{\partial^2 \bar{\alpha}}{\partial \delta \partial \tau} \right) .
\end{aligned}
\qquad \text{(A3)}
$$

The right hand sides of eq.A3 follow readily from eq.A1. From the explicit expression

$$
\bar{\alpha} = \sum_{k=1}^{10} \sum_{j=1}^{10} \left\{ a_{jk} \delta^j + b_{jk} \delta^j e^{-\delta^2} \right\} \tau^{k-5} + \sum_{k=11}^{12} \sum_{j=1}^{10} \left\{ a_{jk} \delta^j + b_{jk} \delta^j e^{-\delta^2} \right\} \tau^{k-11\frac{1}{2}}
$$

given in ref.47 the derivatives $\partial\bar{\alpha}/\partial\delta$, $\partial^2\bar{\alpha}/\partial\delta^2$, $\partial^2\bar{\alpha}/\partial\tau^2$ and $\partial^2\bar{\alpha}/\partial\delta\partial\tau$ were calculated analytically, and a computer program was written to evaluate the thermodynamic quantities of interest.

We assumed that the equations of state of natural argon and of ^{36}Ar are identical. For the molecular weight of ^{36}Ar (needed to calculate the speed of sound c_s) we used $M_{36} = 35.96755$.

The thermal conductivity λ and the shear viscosity η for natural argon were obtained from ref.48 and converted for ^{36}Ar by means of:

$$
\eta_{36} = \eta_n \left[\frac{M_{36}}{M_n} \right]^{\frac{1}{2}}
$$

$$
\lambda_{36} = \lambda_n \left[\frac{M_n}{M_{36}} \right]^{\frac{1}{2}} ,
$$

where $M_n = 39.948$ is the molecular weight of the natural isotopic mixture of argon. The sound damping factor Γ_s is obtained from ref.49 and converted for ^{36}Ar at the thermodynamical states of our measurements by interpolating the dimensionless quantity $\Gamma_s t_\sigma/\sigma^2$ as function of $\rho\sigma^3/V2$, with $t_\sigma = \frac{1}{2}\sigma\sqrt{M/k_BT}$ and

$$
\sigma = 0.338 \left[\frac{T_c}{T} \right]^{0.07633} \text{ in nm}
$$

(I.M. de Schepper, private communication).

Appendix B.

Madden and Rice [23] propose a generalization of the Mean Spherical Approximation (MSA) [50] for application to fluids with continuous intermolecular potentials:

$$c(r) = \left\{ 1 - \exp\left[\beta\varphi_0(r) \right] \right\} g(r) - \beta\varphi_1(r) \qquad (B1)$$

with $\varphi_0(r) = \varphi(r) - \varphi_m \quad r<r_m$
$= 0 \quad r>r_m$

$\varphi_1(r) = \varphi_m \quad r<r_m$
$= \varphi(r) \quad r>r_m$

$\varphi_m = \varphi(r_m)$

$\varphi(r)$ is the two-particle interaction potential and has its minimum at r_m. The direct correlation function $c(r)$ is related to the pair correlation function $g(r)$ by the Ornstein-Zernike relation:

$$g(r)-1-c(r) = \rho \int d\vec{r}'\, c(|\vec{r}-\vec{r}'|)\, \{g(r')-1\} \qquad (B2)$$

or its Fourier transform

$$S(k) = \frac{1}{1-\rho\tilde{c}(k)} \qquad (B3)$$

where $\tilde{c}(k)$ is the Fourier transform of $c(r)$:

$$\tilde{c}(k) = \int d\vec{r}\, e^{i\vec{k}\cdot\vec{r}} c(r) \; . \qquad (B4)$$

The set of equations (B1)-(B4) were solved for $S(k)$ or $g(r)$ by the method proposed by Gillan [51] to solve the Percus-Yevick and the Hyper-Netted Chain equations. In all our calculations the Lennard-Jones potential was used with $\varepsilon/k_B = 123.2$ K and $\sigma = 0.336$ nm [52]. The resulting set of $\varphi(r)$ and $g(r)$ is used for the calculation of the fourth frequency moment by means of eq.7.

Appendix C.

In fitting the sum of three Lorentzians to experimental data, one has to decide whether $S(k,\omega)$ as function of ω is described by a triplet or by a sum of three central Lorentzians. Therefore it is convenient to rewrite eq.20 as (I.M. de Schepper, private communication).

$$\frac{\pi S(k,\omega)}{S(k)} = \frac{A}{B^2+\omega^2} + F\,\frac{C-\omega^2}{(D^2-\omega^2)^2+4E^2\omega^2} \qquad (C1)$$

with: $w_0 = B$, $\quad \mathrm{Re}\, w_{\pm 1} = E$, $\quad \mathrm{Im}\, w_{+1} = (D^2-E^2)^{1/2}$,

$$A_0 = A/B, \quad \mathrm{Re}\, A_{\pm 1} = \frac{F(C-D^2)}{4D^2E}, \qquad (C2)$$

$$\mathrm{Im}\, A_{+1} = \frac{-F(C+D^2)}{D^2(D^2-E^2)^{1/2}} ,$$

where B and E are chosen > 0.

If $D^2 > E^2$, then Im w_{+1} and Im A_{+1} are real and $S(k,\omega)$ is described by a triplet, but if $D^2 < E^2$, then Im w_{+1} and Im A_{+1} are imaginary, $w_{\pm 1}$ and $A_{\pm 1}$ are real and $S(k,\omega)$ is described by a sum of three central Lorentzians. The sum rules for n=1,2 and 3 are rewritten as:

$$n=1: \quad F=A \qquad (C3a)$$

$$n=2: \quad C=D^2+2E\left[\frac{k^2}{\beta MA} + B - 2E \right] \qquad (C3b)$$

$$n=3: \quad 4E^2-2D^2-B^2+C=0 \qquad (C3c)$$

The actual fits were performed by means of the non-linear least-squares routine ZXSSQ from IMSL [34]. If the n=1 sum rule or the n=1 and the n=2 sum rules were imposed, simply F and C were eliminated as free parameters from the model by means of eqs. C3a and b. If also the n=3 sum rule is imposed, F, C and e.g. D can be eliminated according to:

$$F = A$$

$$C = 4E\left[\frac{k^2}{\beta MA} + B - E\right] - B^2 \qquad (C4)$$

$$D = \left[2E\left\{\frac{k^2}{\beta MA} + B\right\} - B^2\right]^{1/2}$$

which follows in a straightforward manner from C3.

After determination of the parameters A, .., F, the original parameters w_j, A_j, $j = 0, \pm 1$ were calculated according to C2.

References

[1] G.Maitland, M.Rigby, E.B.Smith and W.A.Wakeham, Intermolecular Forces (Clarendon, Oxford, 1981).

[2] I.M.de Schepper, P.Verkerk, A.A.van Well and L.A.de Graaf, Phys.Rev.Lett. **50** (1983) 974.

[3] K.Sköld, J.M.Rowe, G.Ostrowsky and P.D.Randolph, Phys.Rev.A **6** (1972) 1107.

[4] T.A.Postol and C.A.Pelizzari, Phys.Rev.A **18** (1978) 2321.

[5] L.J.Groome, A.Teitsma, P.A.Egelstaff and H.A.Mook, J.Chem.Phys. **73** (1980) 1393.

[6] P.A.Egelstaff, W.Gläser, D.Litchinsky, E.Schneider and J.-B.Suck, Phys.Rev.A **27** (1983) 1106.

[7] W.J.Buyers, V.F.Sears, P.A.Lonngi and D.A.Lonngi, Proc. Symp. Neutron Inelastic Scattering 1971 (IAEA, Vienna, 1972) p.399; Phys.Rev.A **11** (1975) 697.

[8] H.Bell, A.Kollmar, B.Alefeld and T.Springer, Phys.Lett.A **45** (1973) 479; H.Bell, H.Möller-Wenghoffer, A.Kollmar, R.Stockmeyer, T.Springer and H.Stiller, Phys.Rev.A **11** (1975) 316.

[9] P.Verkerk, Proc. Symp. Neutron Inelastic Scattering, Vienna 1977 (IAEA, Vienna, 1978) p.53.

[10] J.L.Yarnell, M.J.Katz, R.G.Wenzel and S.H.Koenig, Phys.Rev.A **7** (1973) 2130.

[11] K.E.Gubbins, C.G.Gray and P.A.Egelstaff, Mol.Phys. **35** (1978) 315.

[12] L.A.de Graaf and B.Mozer, J.Chem.Phys. **55** (1971) 4967.

[13] A.A.van Well and L.A.de Graaf, to be published.

[14] A.A.van Well, P.Verkerk, L.A.de Graaf, J.-B.Suck and J.R.D.Copley, Phys.Rev.A (in press).

[15] L.van Hove, Phys.Rev. **95** (1954) 249.

[16] R.D.Puff, Phys.Rev. **137** (1965) 406.

[17] R.G.DeGennes, Physica **25** (1959) 825.

[18] K.S.Singwi and A.Sjölander, Phys.Rev. **120** (1960) 1093; R.Aamodt, K.M.Case, M.Rosenbaum and P.F.Zweifel, Phys.Rev. **126** (1962) 1165.

[19] J.R.D.Copley, Comput.Phys.Commun. **7** (1974) 289; **21** (1981) 431.

[20] J.Kurkijärvi, Annales Academiae Scientiarium Fennicae A VI no.346 (1970) 1.

[21] S.W.Lovesey, J.Phys.C **6** (1973) 1856.

[22] K.Sköld, Phys.Rev.Lett. **19** (1967) 1023.

[23] W.G.Madden and S.A.Rice, J.Chem.Phys. **72** (1980) 4208.

[24] H.Mori, Progr.Theor.Phys. **28** (1962) 763; R.D.Mountain, Adv.Mol.Relaxation Processes **9** (1977) 225.

[25] P.A.Lonngi and L.S.García-Colín, Can.J.Phys. **58** (1980) 281.

[26] N.K.Ailawadi, A.Rahman and R.Zwanzig, Phys.Rev.A **4** (1971) 1616.
[27] J.R.D.Copley and S.W.Lovesey, Rep.Prog.Phys. **38** (1975) 461.
[28] S.W.Lovesey, Z.Phys.B **58** (1985) 79.
[29] I.M.de Schepper and E.G.D.Cohen, Phys.Rev.A **22** (1980) 287; J.Stat.Phys. **27** (1982) 223.
[30] J.M.Rowe and K.Sköld, Proc.Symp. Neutron Inelastic Scattering, 1972 (IAEA, Vienna, 1972) p.413.
[31] I.M.de Schepper, P.Verkerk, E.G.D.Cohen, A.A.van Well and L.A.de Graaf, Phys.Rev.Lett. **54** (1985) 158.
[32] P.A.Egelstaff in: Neutron Scattering, Editors K.Sköld and D.L.Price (Academic, New York, in press).
[33] L.van Hove, Physica **24** (1958) 404.
[34] I.M.de Schepper, P.Verkerk, A.A.van Well and L.A.de Graaf, Phys.Lett.A **104** (1984) 29.
[35] IMSL Library, Edition 9 (Houston, Texas, 1982).
[36] N.R.Draper and H.Smith, Applied Regression Analysis, 2nd Edition (Wiley, New York, 1981).
[37] P.A.Egelstaff, D.I.Page and C.R.T.Heard, J.Phys.C **4** (1981) 1453.
[38] P.A.Egelstaff and S.S.Wang, Can.J.Phys. **50** (1972) 684.
[39] P.A.Egelstaff, J.-B.Suck, W.Gläser, R.McPherson and A.Teitsma, J.de Phys. **41** (1980) C8-222.
[40] C.H.Reinsch, Numer.Math. **10** (1967) 177.
[41] R.Abe, Progr.Theor.Phys. **21** (1959) 421.
[42] D.J.Winfield and P.A.Egelstaff, Can.J.Phys. **51** (1973) 1965.
[43] J.S.Kirkwood, J.Chem.Phys. **3** (1935) 300.
[44] A.D.J.Haymet, S.A.Rice and W.G.Madden, J.Chem.Phys. **74** (1981) 3033; A.D.J.Haymet and S.A.Rice, J.Chem.Phys. **76** (1982) 661.
[45] P.A.Egelstaff, Proc.Symp. Neutron Inelastic Scattering, 1972 (IAEA, Vienna, 1972) p.383.
[46] L.Groome, K.Gubbins and J.Dufty, Phys.Rev.A **13** (1976) 437.
[47] R.B.Stewart, R.T.Jacobson, J.H.Becker, J.C.J.Teng and P.K.K.Mui in: Proc. 8th Symp. Thermophysical Properties I, Editor J.V.Sengers (Am.Soc.Mechanical Engineers, New York, 1982) p.97.
[48] V.A.Rabinovich, A.A.Wasserman, V.I.Nedostup and L.S.Weksler, Thermophysical Properties of Neon, Argon, Krypton and Xenon (Standard, Moscow, 1976) (in Russian).
[49] S.A.Mikhailenko, B.G.Dudar and V.A.Schmidt, Sov.J.Low Temp.Phys. **1** (1975) 109.
[50] J.Lebowitz and J.K.Percus, Phys.Rev. **144** (1966) 251.
[51] M.J.Gillan, Mol.Phys. **38** (1979) 1781.
[52] J.Rouch, J.P.Boon and P.A.Fleury, Physica A **88** (1977) 347.
[53] J.J.Ullo and S.Yip, Phys.Rev.A **29** (1984) 2092.

[54] I.M.de Schepper, J.C.van Rijs, A.A.van Well, P.Verkerk, L.A.de Graaf and C.Bruin, Phys.Rev.A **29** (1984) 1602; I.M.de Schepper, E.G.D.Cohen and M.J.Zuilhof, Phys.Lett.A **101** (1984) 399.
[55] S.W.Lovesey, Phys.Rev.Lett. **53** (1984) 401.
[56] K.Tokiwano and K.Arakawa, J.Phys.Soc.Japan **51** (1982) 4036.

NUCLEAR INSTRUMENTS AND METHODS 160 (1979) 439-447 ; © NORTH-HOLLAND PUBLISHING CO.

HIGH PRESSURE SAMPLE CONTAINER FOR THERMAL NEUTRON SPECTROSCOPY AND DIFFRACTION ON STRONGLY SCATTERING FLUIDS

PETER VERKERK and A. M. M. PRUISKEN*

Interuniversitair Reactor Instituut, 2600 GA Delft, The Netherlands

Received 30 October 1978

This paper contains a description of the construction and performance of a container for thermal neutron scattering on a fluid sample with about 1.5 cm^{-1} macroscopic cross section (neglecting absorption). The maximum pressure is about 900 bar. The container is made of 5052 aluminium capillary with inner diameter 0.75 mm and wall thickness 0.25 mm; it covers a neutron beam with a cross section of $9 \times 2.5\ cm^2$.

The container has been succesfully used in neutron diffraction and time-of-flight experiments on argon-36 at 120 K and several pressures up to 850 bar. It is shown that during these measurements the temperature gradient over the sample as well as the error in the absolute temperature were both less than 0.05 K.

Subtraction of the Bragg peaks due to container scattering in diffraction experiments may be difficult, but seems feasible because of the small amount of aluminium in the neutron beam. Correction for container scattering and multiple scattering in time-of-flight experiments may be difficult only in the case of coherently scattering samples and small scattering angles.

1. Introduction

To design a sample container for thermal neutron scattering one has to find a compromise between low scattering from the container and maximum attainable pressure, and between low multiple scattering and a reasonable amount of primary scattering from the sample. The first aspect calls for high strength construction materials with small cross sections for scattering and absorption; the second is a question of geometry.

For inelastic measurements aluminium is very suitable as container material. It scatters neutrons mainly coherently and scattering angles where Bragg peaks occur can be avoided as long as the wavelength of the incoming neutrons is not too small; besides, the absorption by aluminium is low.

In elastic measurements the Bragg peaks from an aluminium container have to be subtracted from the diffraction pattern of the sample. For this kind of neutron experiments incoherently scattering materials are generally preferred.

Aluminium alloys with small fractions of other elements, have a considerably increased mechanical strength, whereas the scattering and absorption cross sections are only slightly larger than in pure aluminium.

In this paper a container is described made of 5052 aluminium alloy capillary, with an inner diameter of 0.75 mm and 0.25 mm wall thickness. The container is used for measurements on ^{36}Ar at 120 K and pressures up to 850 bar [1]. Special care is taken that both density and temperature of the liquid argon sample are well-defined.

Section 2 contains definitions of a few parameters to characterise sample containers for scattering experiments. These parameters are used to summarise and compare several constructions applied recently by other authors. Section 3 gives a description of the construction of the present container and the filling line, and section 4 contains results of some calculations and checks concerning temperature measurement and control, and density fluctuations when the container is used in a cryostat at 120 K. The performance is treated in section 5. Some experimental results from a neutron time-of-flight measurement at 850 bar and from a diffraction experiment at 270 bar, both at 120 K, are given together with results from Monte Carlo simulations to estimate the amount of multiple scattering.

2. Constructional aspects

Neglecting self-shielding the fraction of incident radiation scattered by a sample is given by:

$$R_s = \frac{1}{2r} \int_{-r}^{r} [1 - \exp\{-\Sigma_s\, l(x)\}]\, dx, \qquad (1)$$

for a cylinder with radius r or by:

$$R_s = 1 - \exp\{-\Sigma_s d\}, \qquad (2)$$

* Present address: James Franck Institute, University of Chicago, Ill. 60637, U.S.A.

for a slab with an effective thickness (perpendicular to the incoming beam) d. The macroscopic scattering cross section of the sample is Σ_s, $l(x) = 2\sqrt{(r^2 - x^2)}$, and the diameter of the cylinder is supposed to be smaller than the width of the beam.

In first order approximation eq. (1) can be written as $R_s = 0.5\pi\Sigma_s r$ and eq. (2) becomes $R_s = \Sigma_s d$, or in general

$$R_s = \Sigma_s S_s / w, \tag{3}$$

S_s being the cross sectional area of the sample in the scattering plane and w the width of the incident beam. As long as $R_s \ll 1$, eq. (3) is a good approximation, while R_s is a useful measure for the scattering fraction of the sample, and multiple scattering is kept at an acceptable level for most purposes.

If R_s becomes of the order 1, the real scattering fraction differs significantly from eq. (3) (also because self-shielding cannot be neglected) and special constructions with absorbing materials have to be applied to keep multiple scattering within reasonable limits.

The analogue of eq. (3) for the container is

$$R_c = \Sigma_c S_c / w. \tag{4}$$

eqs. (3) and (4) are valid for samples and containers of any geometrical form.

Replacing the scattering cross section by the absorption cross section in eqs. (3) and (4) renders the absorption fraction of sample and container respectively. The transmission of the container is in first order approximation given by:

$$T_c = 1 - (\Sigma_{cs} + \Sigma_{ca})\, S_c / w, \tag{5}$$

where Σ_{cs} and Σ_{ca} stand for the macroscopic cross section for scattering and absorption, respectively.

Parameters relevant to the sample container in recently published[2-8] inelastic thermal neutron scattering experiments on fluids at elevated pressures are summarised in table 1. The temperature and pressure listed in the table refer to the sample with the highest pressure for the experiment reported. The scattering by the sample, the coherent and incoherent scattering and absorption of the container and its transmission, using the formulae mentioned before, are indicated also. In all cases an aluminium alloy has been applied. Chen et al.[4]) and Bell et al.[6]) used plain cylinders. Because it is difficult to manufacture these with very small inner diameter, in all other experiments referred to in table 1 slabs with cylindrical holes have been used. In ref. 4 the scattering by the sample is not small compared to 1 and as one may expect the multiple scattering is high: up to 40% as reported for the incoherently scattering hydrogen sample.

Instead of drilling narrow holes in a slab one may use fillers with slits inside cylinders with larger inner diameter. But in both cases the container scattering is relatively larger than for regular cylinders. Sköld et al.[2]) and Chen et al.[8]) used this method whereas Olsson and Larsson[5]) inserted a filler in cylindrical holes in a slab.

TABLE 1

Data on sample containers for recent neutron inelastic scattering experiments on compressed fluids.

Container geometry	Material (ASTM-code)	Sample	Σ_s [cm^{-1}]	Temperature [K]	P_{max} [bar]	R_s [eq. (3)]	R_c [eq. (4)] coh.	R_c [eq. (4)] inc ($\times 10^{+3}$)	T_c (2200 m/s) [eq. (5)]	Ref.
Cylinder + filler	Al-alloy	H_2O	4.6	300	1950	0.12	0.042	0.3	0.95	2
Slab with holes	Al	^{36}Ar	0.49	300	264	0.13	0.052	0.3	0.94	3
Cylinder	6061-T6	H_2	0.83	85	140	0.42	0.068	0.5	0.92	4
Slab with holes + fillers	Al-alloy	CH_4	2.24	300	1640	0.10	0.071	0.5	0.92	5
Cylinder	5754 X	Ne	0.034	70	110	0.08	0.202	1.4	0.76	6
Slab with holes	6061-T6	N_2	0.139	300	300	0.12	0.060	0.4	0.93	7
Cylinder + filler and Cd shims	7075-T651	H_2	1.36 2.08	293 78	1946 1000	0.21 0.17	0.151 0.128	1.0 0.9	0.82 0.85	8
Cylinder	5052	^{36}Ar	1.59	120	850	0.09	0.006	0.06	0.99	this work

Even after the application of a filler the sample in ref. 7 had a high scattering fraction and to reduce multiple scattering cadmium shims parallel to the scattering plane were used inside the sample container. The authors claim that multiple scattering was negligible in their experiments, but on the other hand correction for the container scattering caused serious problems.

Samples with a relatively small scattering cross section have to be studied using a large container, which unavoidably leads to a larger background as is the case in ref. 6.

It is clear that a sample with a large scattering cross section combined with a container consisting of one or more cylinders yields a low background to sample scattering ratio. The container should preferentially have shims of neutron absorbing material to decrease multiple scattering. This allows for a greater inner diameter of the cylinder, but then on the other hand the wall thickness must also be greater and container scattering increases proportionally to the primary scattering by the sample.

For our measurements on ^{36}Ar at pressures up to 850 bar (where $\Sigma_s \leqslant 1.59$ cm^{-1}) and at a temperature of 120 K, a container was constructed from one single 5 m long capillary, wrapped back and forth to cover the whole cross section of the neutron beam. Multiple scattering reducing shims were not inserted in the container, because of the small inner diameter of the capillary of only 0.75 mm. Nevertheless it is clear from table 1, that this container compares favourably with the other ones tabulated regarding scattering and transmission of the container. The primary scattering from the sample is chosen somewhat low so that little multiple scattering results. A similar container, used in low-pressure work, was constructed before by Sköld et al.[9]).

3. Construction of container and filling line

Some mechanical properties of aluminium 5052 alloy quoted by the manufacturer of the tubing (Uniform Tubes, Inc. Collegeville, Pa., U.S.A.), are summarised in table 2. From the data in the table an average molecular weight of 27.15 and a number density at room temperature $\rho = 0.0596$ Å^{-3} can be derived. Assuming an fcc lattice as for pure aluminium this yields a lattice constant $a = 4.06$Å. If the linear thermal expansion from 120 K to room temperature of 5052 alloy is equal to that of pure aluminium (as is the case in the temperature range 20–100 °C), then $a = 4.05$ Å at 120 K.

In table 3 the coherent scattering length, b [10]), and the absorption and total scattering cross sections, σ_a (2200 m/s) and σ_s [11]) respectively, of each element present in 5052 alloy are summarised. Type 5052 was chosen, because it combines small amounts of iron and copper (with a relatively large scattering cross section) and manganese (with a relatively large absorption cross section) with high strength. For the alloy the microscopic cross section for coherent scattering is $\sigma_c = 4\pi\langle b\rangle^2 = 1.59$ b and for incoherent scattering is $\sigma_{inc} = \sigma_s - \sigma_c = 0.01$ b. The macroscopic cross sections at 120 K are $\Sigma_s = 0.096$ cm^{-1}, $\Sigma_c = 0.095$ cm^{-1}, $\Sigma_{inc} = 0.001$ cm^{-1}, and $\Sigma_a(2200\text{ m/s}) = 0.016$ cm^{-1} respectively.

The aluminium capillary is bent in one piece into 38 parallel tubes, with their center lines

TABLE 2

Some mechanical properties of aluminium 5052 alloy[a].

Chemical composition (%)	Al 96.5; Cu 0.10; Mn 0.10; Cr 0.25; Mg 2.5; Zn 0.10; Si and Fe 0.45
Melting range (°C)	590–650
Density (g/cm^3)	2.68
Linear thermal expansion (K^{-1})	23.8×10^{-6} (for 20–100 °C)
Tensile strength (kgf/mm^2)	20, 27 or 30
Yield strength (kgf/mm^2)	9, 21 or 26
Elongation (%)	25, 10 or 8
Hardness (Brinell)	47, 68 or 77

[b]

[a] As quoted by the manufacturer of the tubing, Uniform Tubes, Inc., Collegeville, Pa., U.S.A.

[b] Properties of respectively annealed, half-hard, and hard temper material.

TABLE 3

Coherent scattering length, total scattering and absorption cross sections of the elements present in 5052 aluminium.

Element	b [10^{-12} cm]	σ_s [10^{-24} cm^2]	σ_a (2200 ms^{-1}) [10^{-24} cm^2]
Al	0.35	1.5	0.235
Cu	0.76	8.5	3.80
Mn	−0.39	2.0	13.3
Cr	0.352	4.1	3.1
Mg	0.52	3.7	0.063
Zn	0.57	4.2	1.10
Si	0.42	2.2	0.160
Fe	0.95	11.8	2.55
Weighted av.	0.356	1.60	0.26

1.3 mm apart, and mounted in an aluminium frame. To optimise the amount of sample seen by the incoming neutrons the plane of the parallel tubes makes an angle of 45° with the incoming beam; the tubes are perpendicular to the scattering plane. This implies that detectors at scattering angles between 0° and 90° view all the tubes separately (see fig. 1), which minimises self shielding of the sample.

Because of its higher strength hard-temper tubing was chosen. Since the container was designed to be used for ^{36}Ar, which was available in a limited amount only, much care has been taken to keep the excess volume outside the neutron beam as small as possible. So the capillary had to be bent between the parallel pieces with the smallest possible radius, which the manufacturer of the capillary advices to be 2.5 times the outer diameter, i.e. 3.1 mm. However, this proved to be impossible in practice, and a compromise had to be made between attainable maximum pressure and excess volume. After annealing the capillary for three hours at 200 °C the smallest bending radius without causing kinking or collapses turned out to be 5.5 mm. The annealing caused a decrease of the strength, and the maximum pressure of 1500 bar initially aimed at could not be reached. The bursting pressure proved to be about 1250 bar after the annealing and bending. Higher annealing temperatures caused a rapid further decrease in bursting pressure.

To connect the container with the supply bottle and pressure system, one end of the aluminium capillary was linked to a stainless steel capillary of 1 m length, inner diameter 0.4 mm, and outer

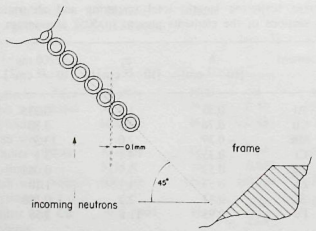

Fig. 1. Cross section in the scattering plane of the sample container.

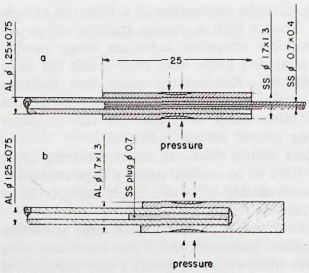

Fig. 2. (a) Coupling between aluminium and stainless steel capillary by means of a stainless steel sleeve. (b) Sealing of the end of an aluminium capillary with a steel plug and steel cap. Measures in mm.

diameter 0.7 mm. A drawing of the coupling is shown in fig. 2a. The wall of the aluminium tube is enclosed between the steel tube and a steel sleeve (inner diameter 1.3 mm, outer diameter 1.7 mm). By impressing the sleeve locally over a length of a few millimeters with a hydrostatic pressure of 2000 bar for a few minutes, a tight leak proof connection is obtained. In several trials this technique proved to be safe at sample pressures of up to about 1500 bar. The method was adopted from the Van der Waals laboratory, Amsterdam, where it has been common use for many years for connecting steel capillaries of different sizes.

The other end of the aluminium capillary is sealed with a steel cap, which is connected in a similar fashion (see fig. 2b). In this case a steel plug of 0.7 mm diameter replaces the steel capillary of fig. 2a.

4. Temperature and density control of the sample

To mount the container in a cryostat and to control and measure the temperature of the sample, the aluminium capillary is fixed in an aluminium frame (see fig. 3), which combines small weight with good thermal conductivity. The capillary fits into grooves 1.3 mm wide, indicated in fig. 3. To ensure good thermal contact between the capillary and the frame, which contains resistors for measuring and controlling the sample temperature, a mixture of silicon grease and copper powder is applied between the grooves and the

capillary (later replaced by commercially available heat transfer compound for cooling power transistors).

The sample temperature is controlled by means of an NTC resistor and measured absolutely with a calibrated platinum resistor. Through the electrical wires heat flows from the outside of the cryostat to the resistors, which if totally dissipated in the resistors may cause temperature fluctuations due to changes of the ambient temperature, and errors of a few K. To avoid this the resistors with 10 cm of the lead wires are mounted inside the frame, and again heat transfer compound is applied. Thus estimated errors are reduced to the order of 0.01 K.

The whole container, mounted in the cryostat is surrounded by a heat radiation shield of 1 cm aluminium (clad with cadmium) with 0.1 mm alumi-

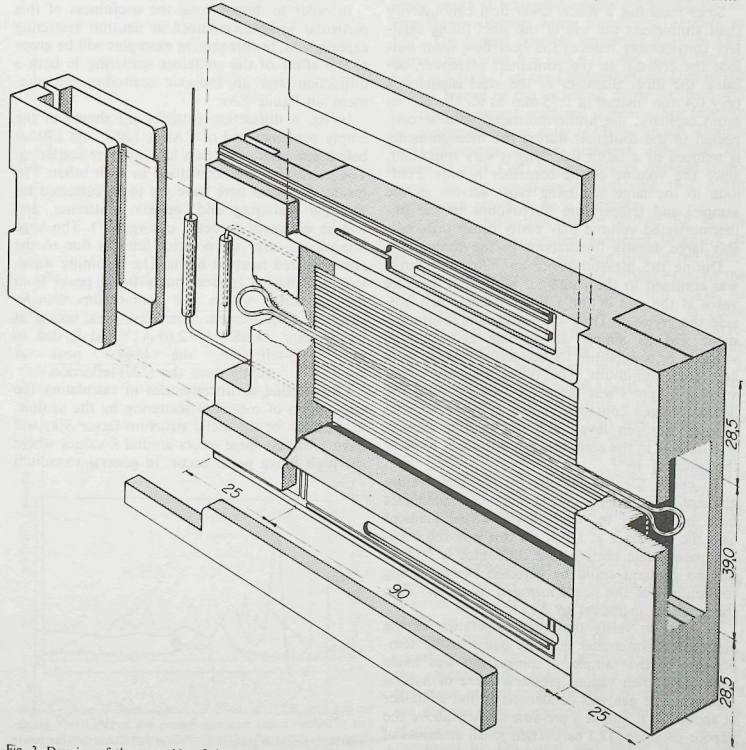

Fig. 3. Drawing of the assembly of the complete container. The upper and lower bar of the frame contain grooves for sensors for temperature control and measurement. Dimensions are in mm.

nium foil windows for the incoming neutrons and for those scattered into the detectors. During the measurements this shield is kept at about the same temperature as the sample.

It is easily calculated that, if the container and the shield are kept at 120 K, the heat flow by radiation from the walls of the cryostat is reduced to about 10 mW and the temperature gradient over the container will not exceed 5 mK.

Since steel has a much lower heat conductivity than aluminium the use of the steel filling capillary considerably reduces the heat flow from outside the cryostat to the container. Moreover, because the inner diameter of the steel capillary is only 0.4 mm instead of 0.75 mm as for the aluminium capillary, the unthermostrated volume connected to the container during the measurements is reduced by a factor 0.3. This is very important, since the volume of the container is only 2 cm^3 (due to the large scattering cross section of the sample) and temperature fluctuations in the unthermostrated volume may easily cause unacceptably large density fluctuations in the container.

During the measurements on ^{36}Ar the sample was confined to the container by a high pressure valve at the end of the filling capillary, just outside the cryostat. Thus the instrumental arrangement was as simple as possible and external volumes or possibilities for accidental leakage were kept to a minimum. The filling capillary (inner volume 0.1 cm^3) was thermally isolated from the liquid nitrogen container in the cryostat with its variable nitrogen level, and the relative density fluctuations in the container are estimated to be of the order of 10^{-3}.

To check the calculations on the temperature gradient, two copper-constantane thermocouples have been used to measure the actual gradient over the container at 120 K. In this way the smallest measurable temperature difference is 0.05 K. But no gradient could be detected except during the refilling of the liquid nitrogen container: then the gradient increased to 0.15 K.

In order to verify that the temperature of the platinum thermometer is really equal to the temperature of the sample, a comparison was made with the known vapour pressure curve of natural argon[12]. The gas was condensed in the container at about 120 K and at a pressure slightly above the vapour pressure (12.1 bar). Then small amounts of argon were repeatedly released through the high pressure valve at the end of the filling capillary. Coexistence of gas and liquid was reached when the pressure remained constant. The temperature of the sample was determined from the measured pressure and the thermodynamic data of argon[12]), and agreed within the accuracy (0.05 K) with the temperature determined from the resistance of the calibrated platinum resistor.

5. Performance

In order to demonstrate the usefulness of this particular sample container in neutron scattering experiments, in this section examples will be given of the effect of the container scattering in both a diffraction and an inelastic scattering measurement on liquid ^{36}Ar.

In fig. 4 diffraction patterns are shown of the empty container and of ^{36}Ar at 120 K and 270 bar before and after correction for container scattering. The intensities are normalised to each other. The results displayed here have yet to be corrected for multiple scattering and inelastic scattering, and will be discussed in detail elsewhere[13]). The large intensity at zero wave-vector limit is due to the non-scattered neutron beam. The incoming wavelength of 0.89 Å renders many Bragg peaks from the container within the momentum transfer range of measurement. The first peak occurs at wave-vector transfer $k = 2.69$ $Å^{-1}$ and is due to the (111)-reflection, the largest peak at $k = 4.39$ $Å^{-1}$ stems from the (220)-reflection.

Clearly, due to uncertainties in calculating the attenuation of container scattering by the sample, the results for the static structure factor $S(k)$ will have relatively large errors around k-values where the high Bragg peaks occur. In general vanadium

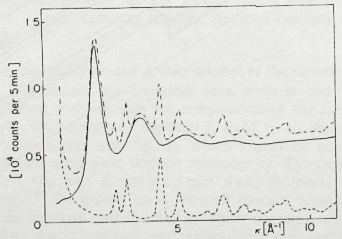

Fig. 4. Diffraction pattern of ^{36}Ar at 120 K and 270 bar before and after correction for container scattering (dash–dot, respectively solid line), and of the empty container (dashed line).

and titanium alloys, which scatter mainly incoherently, are more suitable materials for containers in diffraction work. But rather than constructing a separate container from diffraction experiments and solving the inherent new problems it seemed worthwile to use the available aluminium container used also in inelastic neutron scattering work, for which the average amount of scattering is low.

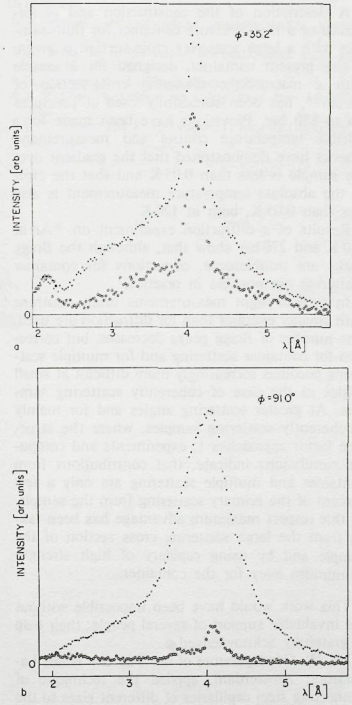

Fig. 5. Time-of-flight spectra of ^{36}Ar at 120 K and 850 bar (black dots), and of the empty container (open circles) at two selected scattering angles, after correction for time-independent background. The incoming wavelength is 4.08 Å. The vertical scale is in arbitrary units and different for a and b.

In fig. 5 two examples of uncorrected time-of-flight spectra of ^{36}Ar at 120 K and 850 bar are shown together with the scattering from the empty container (of the same type as in the above mentioned diffraction experiment). The scattering angles are 35.2°, and 91°, the incoming wavelength is 4.08 Å, so the wave-vector transfer k (at zero energy transfer) is 0.93 and 2.20 $Å^{-1}$, respectively.

There is no primary scattering from aluminium Bragg peaks at scattering angles $\phi \leqslant 91°$ (cf. fig. 4). The (111)-reflection from aluminium appears at 120°. The largest possible scattering angle of 180° corresponds with $k = 3.08$ $Å^{-1}$, just below the value $k = 3.10$ $Å^{-1}$ of the (200)-reflection. Due to the energy spread of the incoming neutrons there will be some backward scattered intensity, but this can be neglected since cotg $(\phi/2)$ is small. Double (111)-reflections scatter neutrons anywhere between 0° and 120°, but mainly in forward directions. So for small-angle scattering this might sometimes prove to be a nuisance.

From the diffraction pattern of ^{36}Ar (fig. 4) it is clear, that the integrated scattered intensity at 35.2° ($k = 0.93$ $Å^{-1}$) is less than 10% of the intensity from an isotropic scatterer, which explains the low signal to background ratio at this angle. At 91° scattering angle the total intensity is about equal to that of an isotropic scatterer and subtraction of container scattering is no problem. With any of the other containers, referred to in table 1, container scattering at small angles would be even more troublesome if used with a coherently scattering sample like liquid ^{36}Ar, due to the larger values of R_c [eq. (4)]. In the present case advantage has been taken from the large coherent scattering cross section of the sample, resulting in a comparatively high signal to background ratio.

To obtain some insight in the amount of multiple scattering to be expected with this particular sample container, Monte Carlo simulations with a computer program due to Bischoff[14]) and Copley[15]) have been performed. To generate the double differential cross section $d^2\sigma/d\Omega d\lambda$ of liquid ^{36}Ar, a model by Nelkin and Ghatak[16]) for the incoherent dynamic structure factor $S_s(k, \omega)$ has been used, together with Sköld's[17]) prescription to generate the coherent one, $S(k, \omega)$. Our measurements of the static structure factor $S(k)$ of argon at 120 K are not yet fully corrected and analysed and $S(k)$ of neon at corresponding temperature and density, measured by De Graaf and Mozer[18]), was used with scaled k-units. Results are presented in fig. 6

for scattering angles of 35.2° and 91° (the same as in fig. 5) and for 270 bar (density 0.0195 Å^{-3}). At small angles the multiple scattering, like the container scattering, is high. It even exceeds the single scattering, and it is caused by the pronounced structure in the liquid and the absence of any neutron absorbing material in the container. Application of neutron absorbing materials to reduce multiple scattering is difficult in this particular sample container due to the small size of the tubes and would lead to loss of intensity. Accurate calculations of the multiple scattering therefore, are required to correct experimental results.

The results of the Monte Carlo calculations carried out at 91° scattering angle are also more or less representative for an incoherently scattering sample and it is clear that for this case only a crude estimate of the multiple scattering will be needed for a sufficiently accurate correction of experimental results. These qualitative conclusions apply equally well to our measurements at 850 bar.

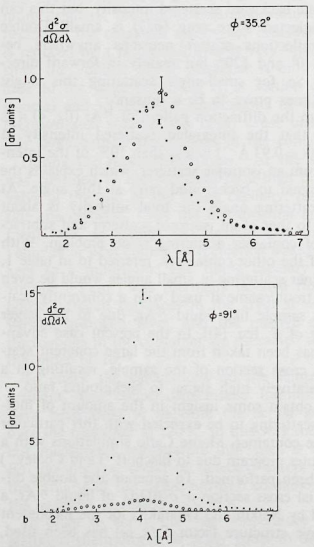

Fig. 6. Simulated time-of-flight spectra of ^{36}Ar and 120 K and 270 bar. Container scattering is not included. Dots represent single scattering, open circles represent all multiple scattering. The incoming wavelength is 4.08 Å. The error bars indicate the standard deviation due to the finite number of neutrons used in the simulation. Uncertainties from any other source are not indicated. The vertical scale is in arbitrary units, and similar for a and b.

6. Conclusions

A description of the construction and performance of a high pressure container for fluid samples with a large scattering cross-section is given.

The present container, designed for a sample with a macroscopic scattering cross-section of 1.6 cm^{-1}, has been succesfully used at pressures up to 850 bar. Provisions have been made for a reliable temperature control and measurement. Checks have demonstrated that the gradient over the sample is less than 0.05 K and that the error in the absolute temperature measurement is also less than 0.05 K, both at 120 K.

Results of a diffraction experiment on ^{36}Ar at 120 K and 270 bar show that, although the Bragg peaks are troublesome, corrections for container scattering are possible in practice.

In time-of-flight measurements often neutrons with smaller energies than for diffraction are used. The number of Bragg peaks decreases, but correction for container scattering and for multiple scattering becomes increasingly more difficult at small angles in the case of coherently scattering samples. At greater scattering angles and for mainly incoherently scattering samples, where the structure factor approaches 1, experiments and computer simulations indicate, that contributions from container and multiple scattering are only a few percent of the primary scattering from the sample. In this respect maximum advantage has been taken from the large scattering cross section of the sample and by using capillary of high strength aluminium alloy for the container.

This work would have been impossible without the invaluable support of several people; their help is gratefully acknowledged.

Mr. W. Goedegebuure of the Van der Waals Laboratory, Amsterdam, applied the technique of connecting steel capillaries of different sizes to the coupling between the aluminium and the steel capillary. He also gave valuable advice on high pressure equipment. Messrs. S. van der Helm, C. Bok, and J. van Leeuwen of the Interuniversitair Reactor Instituut performed innumerable tests before the present construction of the container and its heat treatment was decided upon. Mr. V. K. Boutkan cooperated in the time-of-flight experiments.

The many discussions with Prof. J. J. van Loef and Dr. L. A. de Graaf are gratefully acknowledged.

References

1) P. Verkerk, *Neutron inelastic scattering* (IAEA, Vienna, 1978) vol. 2, 53.
2) K. Sköld, L. Karlén and J. Sciesinski, Nucl. Instr. and Meth. **56** (1967) 305.
3) A. Hasman, Ph. D. Thesis (Delft, 1971).
4) S. H. Chen, Y. Lefevre and S. Yip, Phys. Rev. **A8** (1973) 3163.
5) L. G. Olsson and K. E. Larsson, Physica **72** (1974) 300.
6) H. Bell, H. Moeller-Wenghoffer, A. Kollmar, R. Stockmeyer, T. Springer and H. Stiller, Phys. Rev. **A11** (1975) 316.
7) R. K. Hawkins and P. A. Egelstaff, Mol. Phys. **6** (1975) 1639.
8) S. H. Chen, T. A. Postol and K. Sköld, Phys. Rev. **A16** (1977) 2112.
9) K. Sköld, J. M. Rowe, G. Ostrowski and P. D. Randolph, Phys. Rev. **A6** (1972) 1107.
10) G. E. Bacon, Acta Cryst. **A28** (1972) 357.
11) C. G. Shull, Compilation 1971, M.I.T.
12) I.U.P.A.C., *International thermodynamic tables of the fluid state, argon, 1971* (Butterworths, London, 1972).
13) J. van Tricht and P. Verkerk, to be published.
14) F. G. Bischoff, Ph. D. Thesis (Rensselaer Polytechnic Institute, 1970).
15) J. R. D. Copley, Comp. Phys. Comm. **7** (1974) 289.
16) M. Nelkin and A. Ghatak, Phys. Rev. **A135** (1964) 4.
17) K. Sköld, Phys. Rev. Lett. **19** (1967) 1023.
18) L. A. de Graaf and B. Mozer, J. Chem. Phys. **55** (1971) 4967.

Nuclear Instruments and Methods in Physics Research 228 (1985) 438–464
North-Holland, Amsterdam

II

CALCULATION OF THE DYNAMIC STRUCTURE FACTOR FROM THERMAL NEUTRON TIME-OF-FLIGHT SPECTRA

Peter VERKERK and Ad A. VAN WELL
Interuniversitair Reactor Instituut, 2629 JB Delft, The Netherlands

Received 3 May 1984

A description is given of a system of computer programs to calculate the dynamic structure factor from thermal neutron scattering time-of-flight measurements. A high degree of flexibility is obtained, in order to suit different demands of various experiments. Each program, as well as the data organisation, is described separately. The general applicability will be illustrated with two case histories: an experiment on liquid argon to obtain accurate data on the dynamic structure factor and an experiment on solid NH_4MnCl_3 to obtain information on the rotational motions of the NH_4-group.

1. Introduction

In order to obtain the dynamic structure factor $S(k, \omega)$ or its Fourier transform the intermediate scattering function $F(k, t)$ from thermal neutron time-of-flight measurements, corrections have to be made for the following effects:
- container scattering,
- background, due to fast neutrons, gamma radiation, etc., which is independent of time-of-flight channel,
- instrumental resolution,
- energy dependent detector efficiency,
- multiple scattering,
- self shielding of sample.

In addition, the double differential scattering cross-section has to be converted to $S(k, \omega)$ or $F(k, t)$. If at a fixed scattering angle φ the time-of-flight (or energy transfer $\hbar\omega$) varies, the momentum transfer $\hbar k$ changes as well, according to

$$k^{*2} = 2 - \Delta E^* - 2(1 - \Delta E^*)^{1/2} \cos\varphi.$$

with $k^* = k/k_0$, and $\Delta E^* = \hbar\omega/E_0$ being the energy transferred from the neutron to the sample, k_0 the wave number and E_0 the energy of the incoming neutrons. As the expression above depends on instrumental parameters, it is convenient to interpolate the experimental data to a rectangular (k, ω)-grid.

This paper describes a system of computer programs to perform the necessary calculations to apply the corrections mentioned above. The programs were actually developed on behalf of a series of measurements on liquid argon [1]. All the information from such experiments on monatomic fluids is contained in the quasi-elastic line shape of the time-of-flight spectra. In order to be able to make a meaningful comparison of $S(k, \omega)$ with the theory and to obtain reliable data for derived properties such as the frequency moments and the density derivative of $S(k, \omega)$, very accurate measurements are needed. The rotating-crystal spectrometer IN-4 at the High Flux Reactor of the Institut Laue-Langevin, Grenoble, is at present the most suitable instrument to carry out such measurements and was used for the argon experiment mentioned. It should be emphasized that the system for data correction described here can be used for any multiple detector time-of-flight experiment.

The experiment consisted of the following measurements: Seven different samples were used, employing two different containers. Two additional measurements on different vanadium samples, adapted to the

0168-9002/85/$03.00 © Elsevier Science Publishers B.V.
(North-Holland Physics Publishing Division)

different geometries of the two containers, were used to determine the resolution functions and to normalise the argon measurements. Furthermore, experiments with the two empty containers were done to deduce the correction for background scattering. Since for each of these measurements more than 60 detector angles were used, a total of nearly 700 time-of-flight spectra were produced. The computer programs available at the time when this experiment was done, were unsuitable to deal with such a large amount of data with high statistical accuracy. Therefore we devised a new system of computer programs, starting from the procedure described by Copley et al. [2]. The modular structure of their system was maintained, but the fixed sequence of the different correction steps was abandoned. In our system the order is free – within limits – and can be adapted to various types of experiment or to the ideas of the experimentalist. To facilitate this, the correction procedure was further divided into more independent steps; the output from each step is stored in a file (e.g. on disk). The details are given in the section on data organisation. As an additional advantage all intermediate results can be inspected even after completion of all corrections and one may start again at any step in the procedure, e.g. with a modification in one of the programs or in the input data.

The method for resolution correction as described in ref. [2] was replaced by a new algorithm [3]. The latter is fast and highly automatic, which is important for treating large amounts of data, and estimates the propagation of the experimental error *and* the systematic error originating from the deconvolution.

Other major modifications of the system of Copley et al. consist of an optimisation of their methods to correct for time-independent background and for multiple scattering. The remaining correction routines from ref. [2] were merely adapted to the general set-up of the system discussed in the present paper.

The programs are based on the following set-up of the experiment. A pulsed monochromatic neutron beam of wavelength λ_0 and repetition rate $1/T$ is incident on the sample. The incident flux is monitored by a (low efficiency) detector. The scattered neutrons are detected by a number of counters at fixed scattering angles and distances from the sample. The time of flight of the neutrons, which is proportional to their wavelength λ, is measured by a multichannel analyser system, which is triggered by the rotating crystal or chopper. A second monitor in the monochromatic beam after the sample is used to check the timing of the multichannel analyser.

In the remainder of this paper, the programs are referred to by means of a code name, defined here.

(a) The programs performing the actual corrections are:

CONT: subtraction of container scattering;
DECO: deconvolution of the time-of-flight spectrum and the time-of-flight resolution function;
DEFF: correction for detector efficiency;
MULCOR: correction for multiple scattering;
SSH: correction for self-shielding;
TINO: subtraction of time independent background and normalisation with respect to the number of incoming neutrons.

(b) Preparatory calculations, needed for the corrections, are performed by:

MSCAT: simulation of the experiment by means of the Monte Carlo technique, in order to determine the multiple scattering;
SAF: calculation of the attenuation of container scattering by the sample on behalf of CONT and calculation of self shielding in the sample on behalf of SSH.

(c) Programs necessary for the conversion of time-of-flight spectra to $S(k, \omega)$ are:

INTPOL: conversion of the double differential cross section obtained at the experimental scattering angle to $S(k, \omega)$ at a rectangular (k, ω)-grid;
NORM: normalisation of the time-of-flight spectra and of the resolution function;
TOP: determination of the position on the time-of-flight scale of the monitor peaks and of the peaks in the resolution run; calculation of the relation between time-of-flight scale and wavelength- (or energy-) scale.

(d) Program MOMENT to calculate the frequency moments $\langle\omega^n\rangle$ of $S(k, \omega)$, defined by

$$\langle\omega^n\rangle = \int_{-\infty}^{\infty} \omega^n S(k,\omega)\mathrm{d}\omega,$$

for $n = 0, \cdots, 4$ from the experimental data.

All these programs keep track of the statistical error, and – if possible – calculate the contribution of uncertainties in the corrections to the total estimated error in $S(k, \omega)$ or $\langle \omega^n \rangle$. Due to the complicated nature of some of the corrections the law of propagation of errors can not always be applied rigorously. For instance, inclusion of the covariances in the calculation would increase the computing time considerably, because it involves manipulation of large matrices (e.g. inversion). On the other hand, taking into account the variances only, still leads to useful estimates of the accuracy of the $S(k, \omega)$-data, as will be demonstrated in section 4 on applications. Therefore, all programs except MOMENT neglect the covariances. So, one needs checks to confirm the reliability of the error estimates for $S(k, \omega)$ and an independent measure for the quality of the experimental $S(k, \omega)$-data. Two relations can be used for this purpose without the need for additional knowledge about e.g. the static structure or the interaction potential. These are:

(1) The detailed balance condition:

$$S(k, -\omega) = \mathrm{e}^{-\hbar\omega/k_B T} S(k, +\omega), \tag{1}$$

which can be used to compare energy-loss with energy-gain data; T is the temperature of the sample and k_B the Boltzmann constant. The relation is applied in INTPOL.

(2) The first frequency moment $\langle \omega \rangle$ of $S(k, \omega)$:

$$\langle \omega \rangle = \hbar k^2 / 2M, \tag{2}$$

with M the mass of one particle in the sample.

Section 2 gives a description of the system of data management, in section 3 each program is described separately, and in section 4 some examples of applications of the present system will be presented.

2. Data management

Copley et al. [2] store intermediate results of a number of corrections on a random access file for inspection and in order to be able to omit parts of the correction procedure. We extended their system to obtain and save the intermediate results of all programs mentioned in the introduction and to enable the experimentalist to change the sequence of the various corrections. A detailed description of the data set organisation we have chosen is given:

The input data and all intermediate and final results are written on a random access file. This file can be copied on magnetic tape for later re-examination, improvements, etc. The file consists of 2500 numbered records, divided in series of 65. The ith record in series S_m is denoted by r_{mi} ($i = 1, \cdots, 65$; $m = 1, \cdots, 38$). Each S_m may contain the spectra of one measurement (e.g. on the sample or the container), or the spectra after one of the corrections, or the simulated data from MSCAT, or the simulated spectra interpolated by MULCOR to the experimental detector angles and time channels, or a model $S(k, \omega)$. The first record in every S_m (i.e. r_{m1}) is reserved for information on the sample and spectrometer used in the experiment; on each of the remaining 64 records of set S_m the spectrum at one detector can be written with a maximum of 512 time channels plus the corresponding variances. Room for information specific for the detector (scattering angle, wavelength increment, etc.) is reserved on each record r_{mi}, $i = 2, \cdots, 65$ as well. Data in $S(k, \omega)$ form at constant k are stored in such a way that each record r_{mi} ($i \neq 1$) contains the $S(k, \omega)$-values and variances for one value of k and for a maximum of 512 ω-values, plus information on the k-value, ω-step, number of ω-values, etc. The upper limit for the number of detectors (k-values) or time-channels (ω-values) can easily be increased.

Each set of records S_m is reserved for the output of one particular program or for the raw experimental data. All output is written in the same uniform format, and thus we can change the sequence of corrections or omit any part of the correction procedure, add new programs to the list given in the introduction and insert these at an arbitrary point in the correction procedure, and use one plotting and one printing routine to inspect all intermediate results.

Careful book-keeping is mandatory for the present flexible correction procedure. It is facilitated because each program writes the date and time it was run on the file (in record r_{m1}) and prints this information together with the name of the last correction executed previously.

In section 4 on applications the output of a few programs and some possible flow diagrams will be given as examples.

3. Description of the programs

3.1. Programs performing the actual corrections

3.1.1. CONT: subtraction of empty container run

The operations in CONT are summarised by:

$$s'_{ij} = s_{ij} - a_{ij} c_{ij}, \tag{3}$$

$$\sigma'^2_{ij} = \left(\sigma^s_{ij}\right)^2 + a^2_{ij} \left(\sigma^c_{ij}\right)^2, \tag{4}$$

where s_{ij} is the sample spectrum in channel j of detector i, c_{ij} the container spectrum, σ_{ij} the standard deviation of the corrected spectrum s'_{ij}, σ^s_{ij} and σ^c_{ij} the standard deviations of s_{ij} and c_{ij}, respectively, and a_{ij} the sample attenuation factor calculated by SAF.

The calculation of a_{ij} involves the evaluation of a double integral for all detectors and all time channels. Usually, this calculation will be performed for a reduced number of detectors and channels. In CONT the calculated a's are interpolated to the experimental detector angles and time channels by means of a quasi-Hermitean spline [4]. If the positions of the peak of the second monitor are different in the sample run and the container run, the latter is shifted over the difference by means of the same spline procedure before eq. (3) is evaluated. Because the calculation of the variances is less critical, $(\sigma^c_{ij})^2$ in eq. (4) is not shifted.

3.1.2. DECO: correction for time-of-flight resolution

It is assumed that a time-of-flight spectrum measured at detector i can be written as:

$$I_i(\lambda) = \int R_i(\lambda, \lambda') S_i(\lambda') \mathrm{d}\lambda', \tag{5}$$

with $R_i(\lambda, \lambda')$ the resolution function at wavelength λ and $S_i(\lambda)$ the spectrum we want to determine, without resolution broadening. Usually, only $R_i(\lambda = \lambda_0, \lambda')$ is known from an elastic scattering experiment (e.g. with vanadium; λ_0 is the wavelength of the incident neutrons).

$R_i(\lambda, \lambda')$ is approximated by a translation invariant model resolution function $R'_i(\lambda - \lambda')$, which is set equal to $R_i(\lambda, \lambda')$ at $\lambda = \lambda_0$. This may introduce errors in the shape of narrow inelastic peaks, if these are present in $S_i(\lambda)$, but for quasi-elastic scattering the approximation works usually well.

Then eq. (5) reduces to

$$I_i(\lambda) \approx \int R'_i(\lambda - \lambda') S_i(\lambda') \mathrm{d}\lambda', \tag{6}$$

which is solved for $S_i(\lambda)$ by the method described in ref. [3]. If I_i has been measured at λ_j for $j = 1, \cdots, N$ with $\lambda_j = (j-1)\Delta\lambda + \lambda_1$, S_i is estimated at λ_{ik} for $k = 1, \ldots, K_i$ with $\lambda_{ik} = (k-1)\Delta\lambda_{di} + \lambda_{i1}$. It is inherent to the method of deconvolution, that usually $K_i < N$ with $\Delta\lambda_{di}/\Delta\lambda = N/K_i > 1$. This is due to the combination of resolution and statistical errors in I_i, which does not allow to obtain information about $S_i(\lambda)$ with a resolution better than $\Delta\lambda_{di}$, unless a-priori information is used. If $\Delta\lambda_{di}$ turns out to be too large to reveal the desired details in $S_i(\lambda)$, it means that the resolution or the statistical accuracy in the experiment was insufficient. Since R_i, the shape of S_i, and the relative statistical error in I_i are in general

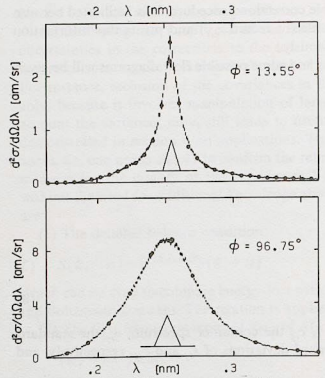

Fig. 1. Neutron time-of-flight spectra at two different scattering angles ϕ before (bare error bars) and after (dots with error bars) correction for resolution by means of DECO. The examples are from measurements on liquid ^{36}Ar with the rotating-crystal spectrometer IN-4 at the ILL, Grenoble. The resolution function is indicated schematically by the triangles. [1 attometer (am) = 10^{-18} m; 1 am/sr = 1 b/(Å sr).]

different for different detectors, $\Delta\lambda_{d_i}$ varies with i.

Formally, we do not know the shape of $S_i(\lambda)$ at values of λ between the points λ_{ik}. If the value of S_i is needed at some $\lambda \neq \lambda_{ik}$ (e.g. in program INTPOL), we will assume that S_i behaves smoothly as a function of λ, and interpolate by means of a spline.

Details of the calculation of the variance-covariance matrix of $S_i(\lambda_{ik})$ are given in ref. [3]. Systematic errors due to the approximation of the solution of eq. (6) are taken into account as well. However, as mentioned in the introduction, the covariances are neglected in the subsequent processing of the data.

Fig. 1 gives two examples of a spectrum before and after correction for resolution.

3.1.3. DEFF: correction for wavelength-dependent detector efficiency

The detector efficiency is given by

$$\epsilon(\lambda) = \frac{1}{R}\int_0^R \left[1 - \exp\left\{-2\Sigma_a(\lambda)\sqrt{R^2 - x^2}\right\}\right] \mathrm{d}x, \tag{7}$$

for a cylindrically shaped detector with its axis perpendicular to the direction of the neutrons to be detected. R is the radius of the cylinder and Σ_a the linear absorption coefficient for the nuclear reaction used to detect the neutrons. The wall effect and attenuation due to other reactions are neglected. Note that eq. (7) is approximately equal to

$$\epsilon(\lambda) \approx 1 - \exp\left[-\frac{\pi}{2}\Sigma_a(\lambda)R\right].$$

To avoid calculation of the integral in eq. (7) for each neutron wavelength corresponding to a time-of-flight channel, the improved approximation

$$\epsilon'(\lambda) = \left[1 - \exp\left\{-\frac{\pi}{2}\Sigma_a(\lambda)R\right\}\right]\left(1 + \sum_{i=1}^{M} b_i\lambda^i\right) \tag{8}$$

can be fitted by means of the least-squares method to the exact expression of eq. (7). For instance, in the case of a detector tube of 2.5 cm diameter, filled with 4 atm ^{3}He, the maximum relative deviation of eq. (8) from eq. (7) is 0.25% for $M = 3$ and $0.01 \leqslant \lambda \leqslant 1.00$ nm. We used $\sigma_a = 5333$ b [5] as the absorption cross section for 2200 m/s neutrons and $n = 0.1061$ nm^{-3} for the number density of the ^{3}He-gas; consequently $\Sigma_a = 0.5660$ cm^{-1} at 2200 m/s and Σ_a is assumed to be inversely proportional to the velocity (i.e. proportional to the wavelength) of the neutrons. For b_i we find $b_1 = -0.20692$ nm^{-1}, $b_2 = +0.37615$ nm^{-2} and $b_3 = -0.18751$ nm^{-3}.

3.1.4. MULCOR: correction for multiple scattering

Prior to MULCOR, the neutron scattering experiment must have been simulated by means of the Monte Carlo program MSCAT of Copley [6]. MSCAT calculates the following five contributions to the total intensity of detected neutrons separately:

Single scattering from
- the sample,
- the container;

multiple scattering from
- the sample,
- the container,
- neutrons scattered in the sample as well as in the container.

Each of these contributions is divided into two parts: one part for neutrons scattered elastically in the final event before detection, the other part for inelastic scattering in the final event. The experimentalist decides which combination of these contributions will be chosen in MULCOR. Fig. 2 shows the relative importance of several contributions to the total intensity of scattered neutrons at two scattering angles for the IN-4 measurements on liquid ^{36}Ar, mentioned in the introduction.

The following corrections and calculations are performed by MULCOR:

(1) Conversion of the output of MSCAT to the form $\mathrm{d}^2\sigma/\mathrm{d}\Omega\mathrm{d}\lambda$.

(2) Interpolation of the simulated spectra to the angles where the detectors of the spectrometer were positioned; usually the simulation is performed for a reduced number of detectors.

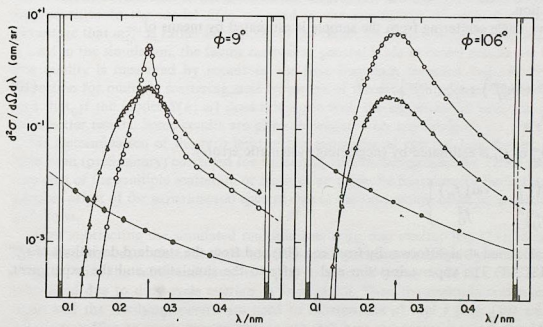

Fig. 2. Simulated spectra (by means of MSCAT) at two scattering angles ϕ for the same neutron scattering experiment as in fig. 1. The arrow indicates the value of the incoming wavelength (0.26 nm). In the experiment 512 time channels of 8 μs width were used, whereas the duty cycle was 4170 μs, resulting in a gap of 64 μs between the last and the first time channel, indicated in the figure by the vertical lines and the hatched area. Circles: single scattering; triangles: multiple scattering; dots: intensity due to duty-cycle overlap (single and multiple scattering); error bars: 2× the standard deviation calculated by MSCAT.

(3) Multiplication of the simulated spectra with the energy-dependent detector efficiency.

(4) Calculation of duty-cycle overlap. Duty-cycle overlap is due to those neutrons losing so much energy in the scattering process that they arrive later at the detector than the time corresponding with the last channel of the cycle and hence will be counted in the time channels of the following cycle (see fig. 2). In a real experiment these neutrons can not be distinguished from those detected during the proper cycle. This will result in errors in $S(k, \omega)$ at large ω and in the frequency moments, unless the data are corrected for the effect. The energy dependence of the detector efficiency (close to 1 for slow neutrons, approaching 0 for fast neutrons) even enlarges this effect.

(5) Interpolation of the simulated spectra to the experimental time-of-flight channels; now a detailed comparison between the measured and simulated spectra is possible. (Usually the simulation is performed for a reduced number of time channels.)

(6) Calculation of the norm of the total simulated intensity and norm of the the experimental spectra for each detector n_i^{sim}, and n_i^{e} respectively, and estimation of their standard deviations. The ratio $r_i\ (= n_i^{\mathrm{e}}/n_i^{\mathrm{sim}})$ is calculated for each detector and the weighted average $\bar{r}$ is determined. Variations of r_i large compared to the estimated standard deviation may indicate that a poor model for $S(k, \omega)$ has been used in MSCAT. A deviation of $\bar{r}$ from 1, large compared to its estimated standard deviation, may indicate that the experimental spectra are normalised incorrectly (assuming a correct normalisation of the simulation). To eliminate errors due to the latter in the correction for multiple scattering, the simulated spectra are multiplied with $\bar{r}$; the deviation of $\bar{r}$ from 1 is a measure of the error in the normalisation of the final $S(k, \omega)$.

(7) Correction for multiple scattering and duty-cycle overlap.

We write the spectra t_{ij} as

$$t_{ij} = \epsilon_j (s_{ij} + m_{ij}) + \epsilon_{j+M} o_{ij}, \tag{9}$$

for detector i and time channel j. The detector efficiency is ϵ_j, s_{ij} is the single scattering spectrum, m_{ij} the multiple scattering intensity, o_{ij} the contribution from overdue neutrons (causing duty-cycle overlap), $M = T/\Delta t$, T the period of one cycle and Δt the channel width. In principle, o_{ij} contains singly and multiply scattered neutrons. Either the factor method or the subtraction method can be chosen for the multiple scattering correction.

(a) *The factor method:* The single scattering from the sample is estimated by means of

$$\begin{aligned} s_{ij}^{\mathrm{e}} &= t_{ij}^{\mathrm{e}} f_{ij}, \\ f_{ij} &= \epsilon_j s_{ij}^{\mathrm{sim}} / \left\{ \epsilon_j \left(s_{ij}^{\mathrm{sim}} + m_{ij}^{\mathrm{sim}} \right) + \epsilon_{j+M} o_{ij}^{\mathrm{sim}} \right\}, \\ o_{ij}^{\mathrm{sim}} &= s_{i,j+M}^{\mathrm{sim}} + m_{i,j+M}^{\mathrm{sim}}. \end{aligned} \tag{10}$$

The standard deviation σ_{ij}^{e} of s_{ij}^{e} is estimated by (neglecting systematic errors):

$$\left(\sigma_{ij}^{\mathrm{e}}\right)^2 = \left(s_{ij}^{\mathrm{e}}\right)^2 \left\{ \frac{\mathrm{var}\left(t_{ij}^{\mathrm{e}}\right)}{\left(t_{ij}^{\mathrm{e}}\right)^2} + \frac{\mathrm{var}\left(f_{ij}\right)}{f_{ij}^2} \right\}.$$

The variance $\mathrm{var}(f_{ij})$ is calculated straightforwardly from eqs. (10) and from the standard deviations of s_{ij}^{sim} and m_{ij}^{sim} as given by MSCAT. The superscripts sim and e refer to the simulation and the experiment, respectively.

(b) *Subtraction method:*

$$\begin{aligned} s_{ij}^{\mathrm{e}} &= t_{ij}^{\mathrm{e}} - \bar{r}\left(\epsilon_j m_{ij}^{\mathrm{sim}} + \epsilon_{j+M} o_{ij}^{\mathrm{sim}}\right), \\ \left(\sigma_{ij}^{\mathrm{e}}\right)^2 &= \mathrm{var}\left(t_{ij}^{\mathrm{e}}\right) + \bar{r}^2 \left\{ \epsilon_j^2 \mathrm{var}\left(m_{ij}^{\mathrm{sim}}\right) + \epsilon_{j+M}^2 \mathrm{var}\left(o_{ij}^{\mathrm{sim}}\right) \right\}, \end{aligned} \tag{11}$$

neglecting systematic errors.

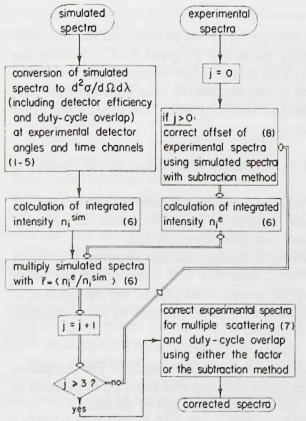

Fig. 3. Flow diagram for program MULCOR. Numbers in parentheses refer to the corrections and calculations mentioned in section 3.1.4.

Note that after the multiple scattering correction s_{ij}^{e} must still be corrected for detector efficiency. It is an open question whether the factor method or the subtraction method should be used; of course, ideally, the two methods should lead to the same result. Copley and Lovesey [7] state that the factor f_{ij} is in any case very sensitive to the model $S(k, \omega)$ used in the simulation, whereas the subtraction method has the advantage that m_{ij}^{sim} is rather insensitive to the choice of model. We find that, when a good model $S(k, \omega)$ is used in the simulation, the factor method in general leads to better results for the experimental $S(k, \omega)$. The quality is measured by means of the first frequency moment $\langle \omega \rangle$, which is very sensitive to the correction for multiple scattering, and by means of the detailed balance condition. On the other hand, we find that, if the model $S(k, \omega)$ does not agree with the experimental one, the subtraction method often gives better results. Some results are given in section 4 on applications.

(8) Determination of the zero level of the experimental spectra. Usually the experimental spectra will have been (preliminary) corrected for time-independent background by TINO prior to MULCOR. In that case part of the multiple scattering or the overlap might be mistaken for background. MULCOR corrects a possible offset of the experimental spectra due to the subtraction of an incorrectly determined background as follows.

After subtracting the simulated multiple scattering and overlap [eq. (11)], a constant contribution b_i is subtracted from each channel of the experimental spectrum measured by detector i using eq. (12) in section 3.1.6, so that the minimum level is equal to zero. If prior to MULCOR too much background was subtracted due to duty-cycle overlap, b_i is negative. Then the multiple scattering and overlap are added again and the resulting spectra are used to redetermine n_i^{e} and $\bar{r}$ [eqs. (10) and (11)]. In practice three iterations suffice to reach convergence. Note that here the factor method should not be used, because f_{ij} [eq. (10)] would distort any constant offset b_i and its determination would be difficult or impossible. As soon as the offset is sufficiently reduced, the definite correction for multiple scattering and overlap is applied, using either the factor method or the subtraction method.

MULCOR is summarised in the flow diagram of fig. 3.

3.1.5. SSH: correction for self-shielding

The incident neutron beam and the scattered neutrons are attenuated by the sample and the container due to absorption and scattering. Using the method of Copley et al. [2], program SAF calculates the self-shielding factor for a reduced number of scattering angles and time-of-flight channels and writes the results on one of the numbered records of the file mentioned in the section on data management. SSH interpolates these factors to the experimental scattering angles and time channels. The spectra and their standard deviations are divided by the proper self-shielding factor.

3.1.6. TINO: subtraction of time-independent background and normalisation with respect to the number of incident neutrons

The intensity in the peak of the first monitor (in front of the sample) is summed over a fixed number of channels. Subsequently, all spectra are normalised to a fixed number of monitor counts, in order to compare different runs and, e.g., to subtract the empty container run from a sample run.

The total background due to the sum of electronic noise, gamma radiation, and fast neutrons is difficult to determine. Some authors (e.g. Copley et al. [2]) carry out a separate run with cadmium in the beam instead of the container with sample, but even then one cannot be certain what part of the background is eliminated by the cadmium (e.g. thermal neutrons incoherently or inelastically scattered by the monochromator).

We choose to determine the background as follows:
A window of m consecutive time channels is shifted along the N time channels of detector i. The intensities of the m time channels within the window are added. The minimum of this sum as a function of position of the window divided by m is assumed to be the background b_i for each time channel of detector i:

$$b_i = \min_{1 \leqslant j_1 \leqslant N-m+1} \frac{1}{m} \sum_{j=j_1}^{j_1+m-1} c_{ij}. \tag{12}$$

where c_{ij} is the total intensity in time channel j. b_i is subtracted from the intensity in all time channels.

This method may fail if the spectrum has wings extending beyond the first or last time channel and duty-cycle overlap occurs. In that case a better approximation of b_i is calculated in MULCOR.

3.2. Programs for preparatory calculations

3.2.1. MSCAT: simulation of the neutron scattering experiment

In order to estimate the multiple scattering in the sample and the container, the neutron transport equation must be solved. This is frequently done with the Monte Carlo technique: the neutron scattering experiment is simulated in the computer and one obtains separately the contributions of singly and multiply scattered neutrons to the total intensity of scattered neutrons. One of the best programs, presently available to the neutron scattering community, is MSCAT, described by Copley [6]. A major advantage of MSCAT is the possibility to include container scattering in the simulation. However, if Bragg scattering (either in the container or in the sample) contributes substantially to the total scattering, the Monte Carlo

Table 1
Output of MSCAT. Each entry represents a two-dimensional array viz. a function of scattering angle and of time-of-flight channel.

Location of the scattering events		Last scattering event was:	
		elastic	inelastic
single	sample	s1e	s1i
	container	c1e	c1i
multiple	sample	sme	smi
	container	cme	cmi
	sample and container	(sc)me	(sc)mi

technique as applied in MSCAT, is rather inefficient, and prolonged runs of the program are needed to acquire sufficient statistical accuracy.

Recently a number of changes has been applied to MSCAT [8]. In the first place, the total scattered intensity measured by the detectors, is divided into ten separate contributions (see table 1) instead of the four described in ref. [6]. In terms of the present output as defined in table 1, the four contributions to the total intensity of the previous version of MSCAT can be given as:

- single elastic: s1e + c1e,
- multiple elastic: sme + cme + (sc)me,
- single inelastic: s1i + c1i,
- multiple inelastic: smi + cmi + (sc)mi

Note that here as well as in table 1 "multiple elastic" means that the neutrons, which have undergone all kinds of scattering processes (at least two), scattered elastically in the last event before detection; "multiple inelastic" has an analogous meaning.

The advantage of this modification is that those contributions to the total scattering, which contain single or multiple Bragg scattering and consequently have a low statistical accuracy, can be separated better from more accurate contributions. For instance, if an experiment with a fluid sample in an aluminium container is simulated, cme and (sc)me, in particular, will have low accuracy. The second type of changes to MSCAT [8] is meant for those cases where contributions such as cme or (sc)me can not be neglected and must be calculated with acceptable accuracy.

These modifications provide the following three possibilities: to truncate the simulation of a neutron history after a fixed number of collisions; to enforce either all collisions to take place in the container or in the sample; and to enforce all last collisions to occur either in the container or in the sample.

After a first run of MSCAT without truncation or forcing, a second run can be performed to improve the accuracy of one or a few of the ten contributions in table 1, using the computer in a more efficient way.

(a) *Time-of-flight resolution.* A useful feature of MSCAT is the possibility to simulate time-of-flight resolution. Since the resolution will have different effects on single and on multiple scattering (in particular if Bragg scattering is involved), the simple convolution of eq. (5) might be inappropriate for the total intensity of scattered neutrons. In that case the correction for multiple scattering must precede the resolution correction and time resolution should be included in the simulation with MSCAT.

In the simulation the time-of-flight resolution of the spectrometer can be approximated by

$$\Gamma_x^2 = \Gamma_t^2 + x^2 \Gamma_{\mathrm{tof}}^2. \tag{13}$$

The three parameters to be chosen are: the standard deviation Γ_{tof} of the inverse-velocity distribution; the standard deviation Γ_t of the distribution of the time-of-arrival at some reference point Z in the beam of non-scattered neutrons; and the position of Z with respect to the sample. Γ_x is the standard deviation of the time of arrival at a distance x from Z, and has a minimum at Z ($x = 0$). All distributions are assumed to be Gaussian.

If the spectrometer used in the experiment is of the rotating crystal type, time focussing of the neutrons occurs due to the Doppler effect. As a result, the spread in time of the neutron pulse will have a minimum at some distance L behind the monochromator (provided the rotation is in the appropriate sense). Clearly, Z should be chosen to coincide with this focussing point. The distance to the monochromator is given by:

$$L = \frac{2v}{\omega \mathrm{tg}\theta_{\mathrm{B}}},$$

where v is the average neutron velocity, ω the angular velocity of the rotating crystal and θ_{B} the Bragg angle. (Actually, a spectrometer with, e.g., two choppers as monochromator has no focusing point and in that case the best approximation would be to choose Z half-way the two choppers.) A measurement of Γ_x at two values of x with, e.g., two monitors at different positions in the neutron beam determines Γ_t and Γ_{tof}. A third monitor may be used to determine experimentally the position of Z instead of calculating it.

Note that MSCAT does not account for collimator divergence, which contributes to the time-of-flight

resolution. In fact, Γ_j and Γ_{tot} are effective parameters describing as closely as possible a more complex situation which is determined by more than two distributions.

(b) *Duty-cycle overlap (see section 3.1.4).* Duty-cycle overlap may also be estimated by means of MSCAT by taking in the simulation a few time channels at large flight times. If the time channels in the experiment are denoted by $t_j = t_0 + \Delta t$, Δt being the channel width and $j = 1, \cdots, N$, overlap can be simulated by choosing a few time channels at $t \geq t_0 + T$, where T is the period of one spectrometer cycle.

3.2.2. SAF: calculation of self shielding and of attenuation of container scattering by the sample

The attenuation factor $a_{i,j}$ in eqs. (3) and (4) and the self-shielding factor (section 3.1.5), which are both angle- and wavelength-dependent, are calculated for the geometry of one cylinder perpendicular to the scattering plane. The latter is defined by the incoming beam, sample, and detectors. The method is described by Copley et al. [2]. The factor $a_{i,j}$ depends upon the wavelength-dependent removal cross sections of sample and container material. These are calculated by MSCAT, which has to be run prior to SAF. The latter calculates $a_{i,j}$ at the same energies for which MSCAT provides the cross sections; the scattering angles for the $a_{i,j}$ in SAF are chosen to be the same as those for which MSCAT simulates the experiment. Before the scattering from the empty container multiplied by $a_{i,j}$ can be subtracted from the sample run, $a_{i,j}$ has to be interpolated to the experimental detector angles and to the energies corresponding with the experimental time-of-flight channels. This is done in program CONT.

The angle- and wavelength-dependent attenuation of the neutrons by sample and container is calculated in a similar way [2]. The interpolation to experimental scattering angles and energies is performed in program SSH.

For a different sample geometry a new version of program SAF must be written.

3.3. Conversion of time-of-flight spectra to $S(k, \omega)$

3.3.1. INTPOL: calculation of $S(k, \omega)$ on a rectangular (k, ω)-grid

This program converts the double differential scattering cross-section $d^2\sigma/d\Omega d\lambda$ to a symmetrised $S(k, \omega)$ and interpolates these data from the points given by the time channel width (i.e. equidistant on λ-scale) to equidistant points on the ω-scale and from constant scattering angle φ to constant k.

(a) *Conversion to symmetrised $S(k, \omega)$.*

The dynamic structure factor is related to the double differential cross-section by

$$S(k,\omega) = \frac{m}{\sigma\pi\hbar}\frac{\lambda^4}{\lambda_0}\frac{d^2\sigma}{d\Omega d\lambda}, \tag{14}$$

where m is the neutron mass, σ the bound atom scattering cross section, λ_0 the wavelength of the incident neutrons and λ the wavelength of the scattered neutrons.

According to the detailed balance condition

$$S(k,-\omega) = \exp\left(-\frac{\hbar\omega}{k_B T}\right) S(k,\omega),$$

we can define a symmetric and an antisymmetric function:

$$S_{sym}(k,\omega) = \tfrac{1}{2}\{S(k,\omega) + S(k,-\omega)\} = \tfrac{1}{2}\{1 + \exp(-\hbar\omega/k_B T)\} S(k,\omega); \tag{15}$$

$$S_{as}(k,\omega) = \tfrac{1}{2}\{S(k,\omega) - S(k,-\omega)\} = \mathrm{tgh}\left(\frac{\hbar\omega}{2k_B T}\right) S_{sym}(k,\omega). \tag{16}$$

Aamodt et al. [9] have shown that the following equation approximately relates $S(k, \omega)$ of a classical system with the real $S(k, \omega)$:

$$S_{cl}(k,\omega) \approx \exp\left(-\frac{\hbar\omega}{2k_B T} + \frac{\hbar^2 k^2}{8Mk_B T}\right) S(k,\omega). \tag{17}$$

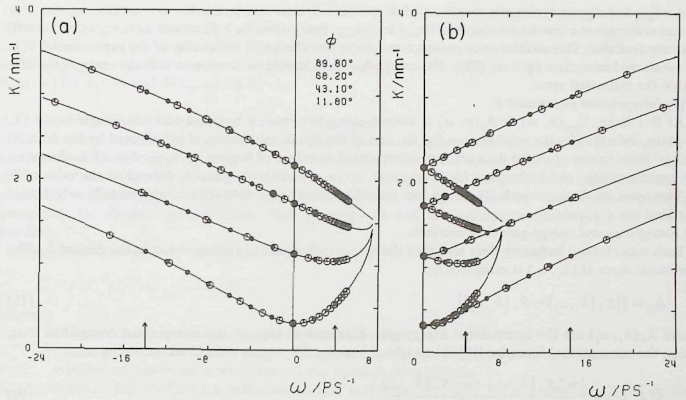

Fig. 4. (a) k as a function of ω for four different scattering angles ϕ, for neutrons with an incoming wavelength of 0.4 nm. At each scattering angle one time-of-flight increment has been chosen, leading to ω-values indicated by the circles. The dots correspond to a set of ω-values with constant increment $\Delta\omega$, which are the same for all four scattering angles. The arrows indicate ω_{min} and ω_{max}, defined in the text (section 3.3.1). (b) Same as fig. 4a but now as function of $|\omega|$. The left arrow indicates ω_{max}, the right arrow $|\omega_{min}|$. After symmetrising $S(k, \omega)$, interpolation to fixed k-values takes place at the ω-values indicated by the dots. Note that both energy-gain and energy-loss data are available only for $0 < \omega < \omega_{max}$.

This equation is exact for a system of non-interacting particles. Note that if $S(k, \omega)$ obeys the detailed balance relation, the right hand side of eq. (17) is a symmetric function of ω. Until now must theoretical calculations have been concerned with a classical system and eq. (17) should be used instead of eq. (15) when comparing results of these theories with experimental data. On the other hand $S_{sym}(k, \omega)$ and $S_{as}(k, \omega)$ are more fundamental quantities in the sense that S_{sym} is the Fourier transform of the real part of the Van Hove correlation function $G(r, t)$ and S_{as} is the transform of the imaginary part.

(b) *Interpolation to equidistant ω_j.*

The input data for INTPOL are given at the wavelength values $\lambda_{ik} = (k-1)\Delta\lambda_i + \lambda_{i1}$, for $k = 1, \cdots, M_i$. $\Delta\lambda_i$ and λ_{i1} are determined by the setting of the spectrometer and possibly by previous corrections (e.g. by DECO). From the relation $E = (\hbar k)^2/2m$ follows

$$\omega = \frac{2\pi^2\hbar}{m}\left\{\frac{1}{\lambda_0^2} - \frac{1}{\lambda^2}\right\}, \tag{18}$$

and consequently

$$\Delta\omega_{ik} = \frac{4\pi^2\hbar}{m\lambda_{ik}^3}\Delta\lambda_i.$$

For constant $\Delta\lambda$ the corresponding energy step $\Delta\omega$ is wavelength-dependent. INTPOL interpolates S_{sym} or S_{cl} and its estimated standard deviation from the data at λ_{ik} (indicated by circles in fig. 4a) to equidistant ω-values ω_j, which are equal for all detector angles and chosen by the experimentalist (dots in fig. 4a). A window $[\omega_{min}, \omega_{max}]$ is defined in such a way that experimental data are available within the range $\omega_{min} \leq \omega \leq \omega_{max}$ at all detector angles.

As S_{sym} and S_{cl} are symmetric functions of ω, the ($\omega < 0$)-data can be used at $\omega = |\omega|$ (see fig. 4b). For $0 < |\omega| \leqslant \omega_1$, where ω_1 is the minimum of $|\omega_{min}|$ and ω_{max}, energy-loss ($\omega > 0$) as well as energy-gain ($\omega < 0$) data are available. This enables us to perform one of the two checks on the quality of the experimental $S(k, \omega)$ mentioned in section 1 [cf. eq. (22)]. The energy-loss data should be consistent with the energy-gain data within the estimated error.

(c) *Interpolation to constant k.*

At this stage, $S_{sym}(k, \omega)$ or $S_{cl}(k, \omega)$ is known along the lines of constant scattering-angle in the (k, ω)-plane, indicated by the solid lines in fig. 4b, and at the equidistant values of ω indicated by the dots. At each of these values of ω, the data are now interpolated to values of k given by $k_i = i\,\Delta k$. Δk is chosen by the experimentalist and is the same for all ω; $i = i_1, \cdots, i_2$, where both i_1 and i_2 depend on the value of ω.

Two cases are distinguished: (1) energy-loss as well as energy-gain data are available and (2) only data of one kind are available.

(1) Energy-loss and energy-gain data available.

Both sets of data, including their standard deviations, are separately interpolated to the desired k_i. The systematic error at (k_i, ω_j) is estimated by

$$\Delta_{ij} = \tfrac{1}{2}\left|S_+(k_i,\omega_j) - S_-(k_i,\omega_j)\right|, \tag{19}$$

where $S_+(k_i, \omega_j)$ are the interpolated energy-gain data and $S_-(k_i, \omega_j)$ the interpolated energy-loss data. Using the conventional formulae [10] the weighted average $\bar{S}(k_i, \omega_j)$ is calculated according to:

$$\bar{S}(k_i,\omega_j) = \left\{\frac{w_{ij}^+ S_+(k_i,\omega_j) + w_{ij}^- S_-(k_i,\omega_j)}{w_{ij}^+ + w_{ij}^-}\right\}, \tag{20}$$

where we have chosen the following weight functions:

$$w_{ij}^{\pm} = \left\{\left(\sigma_{ij}^{\pm}\right)^2 + \Delta_{ij}^2\right\}^{-1};$$

σ_{ij}^- (σ_{ij}^+) is the interpolated standard deviation of $S_-(k_i, \omega_j)$ [$S_+(k_i, \omega_j)$]. $\bar{S}(k_i, \omega_j)$ is considered to be the best approximation of the true $S(k, \omega)$. The error is estimated as:

$$\Delta\bar{S}(k_i,\omega_j) = \left(w_{ij}^+ + w_{ij}^-\right)^{-1/2}. \tag{21}$$

We define a quality measure Q_{ij} by

$$Q_{ij}^2 = \left[\frac{S_+(k_i,\omega_j) - \bar{S}(k_i,\omega_j)}{\sigma_{ij}^+}\right]^2 + \left[\frac{S_-(k_i,\omega_j) - \bar{S}(k_i,\omega_j)}{\sigma_{ij}^-}\right]^2. \tag{22}$$

If $S_+(k_i, \omega_j)$ and $S_-(k_i, \omega_j)$ were normally distributed around the same mean with standard deviation σ_{ij}^+ and σ_{ij}^- respectively and with zero covariances, Q_{ij}^2 would follow the χ^2-distribution with one degree of freedom and the expectation of the average $\overline{Q^2}$ would be 1. Since Q_{ij} does not fulfil these conditions, the expectation of $\overline{Q^2}$ is unknown, but $\overline{Q^2} \gg 1$ certainly indicates that $S_+(k_i, \omega_j)$ and $S_-(k_i, \omega_j)$ do not have the same mean, or in other words that systematic errors are present. Q_{ij}^2, or $\overline{Q^2}$, can be used either to compare numerically the reliability of different measurements, or to check wether a change in one of the corrections is an improvement.

Instead of using the numerical measure Q_{ij} one may compare $S_+(k_i, \omega_j)$ graphically, e.g. as a function of k at constant ω. Note that in either case one actually uses the detailed balance condition as a check on the experimental $S(k, \omega)$.

(2) Only energy-loss or energy-gain data available.

This occurs at $\omega = 0$, at $\omega > \omega_1$ and at large and small k (see fig. 4b). At $\omega > \omega_1$, where the relative error is large, a cubic spline data smoother [4] is used to obtain $S(k, \omega)$ at the desired k_i. At $\omega = 0$ and at large and small k (and for $0 < \omega \leqslant \omega_1$), $S(k_i, \omega)$ is obtained by interpolation without smoothing.

At $\omega = 0$ and at large ω no attempt is made to estimate the systematic error; the interpolated estimated standard error is taken as the error in $S(k_i, \omega)$. At ω-values where energy-gain as well as energy-loss data are available, there will in general be a region $k < k_1$ and $k > k_2$, where only one kind of data is available. In the latter case the relative systematic error of $S(k, \omega)$ is approximated by the relative systematic error of $S(k_1, \omega)$ for $k < k_1$ and $S(k_2, \omega)$ for $k > k_2$.

3.3.2. NORM: absolute normalisation of time-of-flight spectra

In order to normalise the measured time-of-flight spectra, a separate measurement must be made on a sample of which the scattering properties are known. Corrections and calculations are less complicated if this sample scatters purely elastically and incoherently. However, it is not possible to eliminate inelastic scattering entirely. Program NORM uses the elastic part of an incoherently scattering sample (e.g. vanadium) for absolute normalisation. Slab geometry as well as (multiple-)cylinder geometry can be handled.

The total elastic intensity per unit of incident neutron flux scattered into detector i is given by:

$$I_i^{el} = \rho_N V_i^N \sigma_N (4\pi)^{-1} S_N(k_i) \Delta\Omega_i, \tag{23}$$

where

ρ_N: number density of the sample used for normalisation,
V_i^N: volume of the normalisation sample illuminated by the neutrons and seen by detector i,
σ_N: total bound scattering cross-section of the normalisation sample,
$S_N(k_i)$: structure factor of the normalisation sample, including: (1) single elastic scattering. (2) self-shielding and (3) multiple elastic scattering,
$\Delta\Omega_i$: solid angle subtended by detector i, which usually is the same for the sample- and the normalisation measurement.

The intensity scattered by the sample and measured by detector i in time channel j normalised with respect to incident neutron flux can be written as

$$I_{ij}^s = \rho_s V_i^s S_{ij} \Delta\lambda_i \Delta\Omega_i, \tag{24}$$

where ρ_s: number density of the sample,
V_i^s: volume of the sample illuminated by the neutrons and seen by detector i,
S_{ij}: absolutely normalised time-of-flight spectrum,
$\Delta\lambda_i$: width of time-of-flight channel on wavelength scale.

From eqs. (23) and (24) follows

$$S_{ij} = F_i I_{ij}^s / I_i^{el}, \quad \text{with} \quad F_i = \frac{\rho_N V_i^N \sigma_N S_N(k_i)}{\rho_s V_i^s 4\pi \Delta\lambda_i}. \tag{25}$$

For a calibration sample with slab geometry, $S_N(k_i)$ is calculated according to Copley et al. [2] for single and double scattering and according to Sears [11] for the total scattering. For cylinder geometry a Monte Carlo computer simulation with Copley's program MSCAT [6] is used.

Correction for inelastic scattering by the calibration sample:

The Debije–Waller factor is given by

$$W(k) = \exp(-2Ak^2),$$

with A the Debije–Waller coefficient. For example, in vanadium at 120 K, $A = 11 \times 10^{-6}$ nm^2 [12] and the inelastic scattering is less than 3% of the total scattering at $k < 40$ nm^{-1}.

In the neutron-scattering spectra of such a sample the inelastic contribution under the elastic peak is very well approximated by a straight line determined by the average of a few time channels on both sides of the elastic peak. However, if short wavelength neutrons are used, or if the Debije–Waller factor is large (e.g. at high temperatures), this simple method becomes too crude [13].

In that case the inelastic spectrum is approximated by the double differential cross-section for incoherent one-phonon scattering [14]:

$$\frac{d^2\sigma}{d\Omega d\lambda} = C\frac{W(k)}{\lambda^4}k^2\frac{g(\omega)}{\omega}\frac{1}{1-\exp(-\hbar\omega/k_BT)}, \tag{26}$$

where C is a normalisation constant used as a parameter to fit eq. (26) to the measured inelastic spectrum (outside the elastic peak). $g(\omega)$ is the normalised vibrational density of states, which must be given by the user. The Debije model

$$g(\omega) = 3\omega^2/\omega_D^3, \quad \omega < \omega_D,$$
$$= 0, \quad \omega > \omega_D,$$

will often be satisfactory.

3.3.3. TOP: determination of zero energy-transfer point in the spectra

The resolution measurement will be performed with an elastically scattering sample. The position of the elastic peaks will be assumed to be the ($\omega = 0$)-point on the time-of-flight scale. The peak position in units of channel number p_i for detector i is determined by the first moment:

$$p_i = \sum_{j=n_1}^{n_2} jc_{ij} / \sum_{j=n_1}^{n_2} c_{ij}, \tag{27}$$

where n_1 and n_2 are channel numbers chosen respectively 10 to the left and 10 to the right of the channel with maximum intensity and c_{ij} is the measured intensity in time channel j of detector i.

Because of various reasons the spectra of a sample run might be slightly shifted on the time-of-flight scale with respect to the spectra of the resolution run. Therefore, the positions of the monitor peaks in the resolution as well as in the sample measurement are determined too and denoted by p_m^r, and p_m^s, respectively. Then the $\omega = 0$ position in the sample run is given by $p_i + (p_m^s - p_m^r)$.

3.4. MOMENT: calculation of frequency moments

The frequency moments $\langle\omega^n\rangle$ of $S(k, \omega)$ are defined as:

$$\langle\omega^n\rangle = \int_{-\infty}^{\infty}\omega^n S(k,\omega)d\omega. \tag{28}$$

For $n = 0$, 1, 2 and for a one-component system they are given by:

$$\langle\omega^0\rangle = S(k); \quad \langle\omega\rangle = \omega_R = \frac{\hbar k^2}{2M}; \quad \langle\omega^2\rangle = \frac{k_BT}{M}k^2 + O(\hbar^2); \tag{29}$$

$\hbar\omega_R$ being the recoil energy. The equations for $\langle\omega^0\rangle$ and $\langle\omega\rangle$ are exact, the quantum correction for $\langle\omega^2\rangle$ is rather complicated [15]. For $n > 2$, $\langle\omega^n\rangle$ depends upon the interaction potential and the static density correlation functions which are incompletely known for the sample. For a system with a two-particle interaction potential, $\varphi(r)$, the third [16] and fourth [17] moments are given by:

$$\langle\omega^3\rangle = \omega_R\{\omega_R(\omega_R + 4\omega_K) + \Omega^2(k)\}; \quad \langle\omega^4\rangle = \langle\omega^2\rangle\{3\langle\omega^2\rangle + \Omega^2(k)\} + O(\hbar^2). \tag{30}$$

$\hbar\omega_K$ is the average kinetic energy per particle, given by the virial theorem:

$$\frac{P}{\rho} = \tfrac{2}{3}\hbar\omega_K - \tfrac{1}{6}\int d\mathbf{r}\rho g(r)\{\mathbf{r}\cdot\Delta\varphi(r)\},$$

P being the pressure, ρ the particle number density and $g(r)$ the static pair correlation function. For the

moments of $S_{inc}(k, \omega)$, the Fourier transform of the Van Hove self-correlation function, $\Omega^2(k)$ is given by:

$$\Omega^2(k) = \frac{\rho}{M}\int\frac{d^2\varphi(r)}{dz^2}g(r)d\mathbf{r},$$

which is independent of k. For $S_{coh}(k, \omega)$, the Fourier transform of the total Van Hove correlation function, which is the sum of the self- and distinct-part, we have

$$\Omega^2(k) = \frac{\rho}{M}\int(1-\cos kz)\frac{d^2\varphi(r)}{dz^2}g(r)d\mathbf{r}.$$

If the sample consists of particles of more than one species, having different scattering lengths b and molecular weights M, eqs. (29) and (30) cannot be used, as Fredrikze [15] has demonstrated. For instance for the first moment the correct expression is:

$$\langle\omega\rangle = \frac{1}{\langle bb^*\rangle}\left\langle\frac{bb^*}{M}\right\rangle\frac{\hbar k^2}{2},$$

where b^* is the complex conjugate of b. For the modified expressions for the remaining moments see ref. [15].

Program MOMENT calculates $\langle\omega^n\rangle$ for $n = 0, \cdots, 4$, as well as a classical approximation $\langle\omega^n\rangle_{cl}$ for $n = 0, 2, 4$, from the experimental data. $\langle\omega^n\rangle_{cl}$ is defined by:

$$\langle\omega^n\rangle_{cl} = \int_{-\infty}^{\infty}\omega^n S_{cl}(k,\omega)d\omega,$$

with $S_{cl}(k, \omega)$ given by eq. (17). A rigorous check on the experimental data is provided by $\langle\omega\rangle$ or, if $S(k)$ is known from an independent source, by $\langle\omega^0\rangle$.

Instead of eq. (28) we use for the odd moments:

$$\langle\omega^{2n+1}\rangle = \int\omega^{2n+1}\mathrm{tgh}\left(\frac{\hbar\omega}{2k_BT}\right)S_{sym}(k,\omega)d\omega,$$

because INTPOL calculates only the symmetric part of the dynamic structure factor, $S_{sym}(k, \omega)$.

When $\langle\omega^n\rangle$ is calculated from the experimental $S(k, \omega)$, the integral in eq. (28) must be estimated by some numerical procedure. The contribution from $S(k, \omega)$ for $\omega > \omega_L$, $\hbar\omega_L$ being for given k the maximum energy transfer in the neutron scattering experiment, will be more and more important with increasing n. The experimental value of $\langle\omega^n\rangle$ is estimated as follows:

$$\langle\omega^n\rangle \approx 2I_n + M_n;$$
$$I_n = \Delta\omega\left\{\tfrac{1}{2}\delta_{n,0}F(\omega=0) + \sum_{i=1}^{L}F(\omega_i)\omega_i^n\right\};$$
$$F(\omega) = S_{sym}(k,\omega), \quad \text{for } n \text{ even},$$
$$= \mathrm{tgh}\left(\frac{\hbar\omega}{2k_BT}\right)S_{sym}(k,\omega), \quad \text{for } n \text{ odd}. \tag{31}$$

In eq. (31) $2I_n$ is the contribution to $\langle\omega^n\rangle$ from the experimental data, estimated by means of the trapezium formula and M_n is the contribution from a model $S_M(k, \omega)$ at $\omega > \omega_L$. $\omega_i = i\Delta\omega$ are the ω-values of the experimental data and $\delta_{i,j}$ is Kronecker's symbol.

For $S_M(k, \omega)$ we use a Gaussian in ω obeying the detailed balance condition:

$$S_M(k,\omega) = \frac{A}{\sigma\sqrt{2\pi}}\exp\left[-\frac{(\omega - \frac{1}{2}\hbar\beta\sigma^2)^2}{2\sigma^2}\right],$$

where A is the norm and $\beta = 1/k_B T$. In MOMENT two possibilities are available for the determination of the two unknown parameters A and σ:

(1) from a least-squares fit of $S_M(k, \omega)$ to the experimental data at large ω (e.g. at ω_i for $i = \frac{1}{2}L, \cdots, L$);

(2) from Sköld's [18] formula

$$S_M(k,\omega) = S(k) S_{\mathrm{inc}}\left\{ \frac{k}{\sqrt{S(k)}}, \omega \right\},$$

with the free gas model for the incoherent dynamic scattering function

$$S_{\mathrm{inc}}(k,\omega) = S_{\mathrm{f}}(k,\omega) = \frac{1}{k}\left(\frac{M\beta}{2\pi}\right)^{1/2} \exp\left[-\frac{M\beta}{2k^2}\left(\omega - \frac{\hbar k^2}{2M}\right)^2 \right],$$

leading to $A = S(k)$ and $\sigma^2 = k^2/[M\beta S(k)]$.

Once A and σ have been determined, M_n can be calculated by

$$M_n = \int_{-\infty}^{-\omega_L} \omega^n S_M(k,\omega)\mathrm{d}\omega + \int_{\omega_L}^{\infty} \omega^n S_M(k,\omega)\mathrm{d}\omega.$$

The resulting expressions are given in the appendix. If option (2) for A and σ is chosen, $S(k)$ must be known. Since M_0 depends on $A = S(k)$, $S(k)$ is determined from the experimental $\langle \omega^0 \rangle$ in an iterative way, using $2I_n$ [eq. (31)] as a first guess for $S(k)$.

Estimating the error in $\langle \omega^n \rangle$.

The first moment $\langle \omega \rangle$ and, if $S(k)$ is a-priori known, $\langle \omega^0 \rangle$ as well, can be used as a check on the reliability of the experimental $S(k, \omega)$-data. Therefore, it is important to estimate the error in $\langle \omega^n \rangle$ as accurately as possible. As mentioned before, in the calculation of the propagation of the experimental errors the covariances are not taken into account. These could however cumulate in the moments or any quantity derived from the experimental $S(k, \omega)$. Several of the programs, described in this paper, introduce correlations among the experimental data. To improve the error estimate of $\langle \omega^n \rangle$, we use a simple model for the covariances of the $S(k, \omega)$ data at constant k.

The law of propagation of errors yields for the variance of I_n [eq. (31)]:

$$\mathrm{var}(I_n) = (\Delta\omega)^2 \left\{ \tfrac{1}{4}\delta_{n,0}\sigma_0^2 + \sum_{i=1}^{L} \omega_i^{2n}\sigma_i^2 + \delta_{n,0}\sigma_0 \sum_{i=1}^{L} \sigma_i \mathrm{corr}(F_0, F_i) + 2\sum_{i>j=1}^{L}\sum^{L} \omega_i^n \omega_j^n \sigma_i \sigma_j \mathrm{corr}(F_i, F_j) \right\}, \quad (32)$$

where σ_i is the estimated standard deviation of $F_i = F(\omega_i)$. The correlation coefficient $\mathrm{corr}(F_i, F_j)$ is related to the covariance of F_i and F_j, $\mathrm{cov}(F_i, F_j)$, as follows:

$$\mathrm{corr}(F_i, F_j) = \frac{\mathrm{cov}(F_i, F_j)}{\left[\mathrm{var}(F_i)\mathrm{var}(F_j)\right]^{1/2}}.$$

Neglecting the covariances leads to

$$\mathrm{var}(I_n) = (\Delta\omega)^2 \left\{ \tfrac{1}{4}\delta_{n,0}\sigma_0^2 + \sum_{i=1}^{L} \omega_i^{2n}\sigma_i^2 \right\}, \quad (33)$$

which is a low estimate if the data F_i are positively correlated, since $\sigma_i > 0$ for all i. The data F_i are obtained by interpolation in INTPOL from data at equidistant λ-values to equidistant ω-values, where $\Delta\omega$ is chosen by the experimentalist. The ω-increment before interpolation is given by

$$\Delta\omega' = \frac{4\pi^2\hbar}{m\lambda^3}\Delta\lambda. \quad (34)$$

The estimate of $\mathrm{var}(I_n)$ using eq. (33) is approximately proportional to $\Delta\omega$ (note that L is inversely

proportional to $\Delta\omega$). This means that decreasing $\Delta\omega$ by increasing the number L of interpolated data F_i would lead to an arbitrarily small value of $\mathrm{var}(I_n)$, which contradicts common sense. The reason is that interpolation to ω-values with a smaller spacing $\Delta\omega$, causes stronger positive correlations among the interpolated data. A simple solution is to multiply eq. (33) by $\Delta\omega_0'/\Delta\omega$, leading to:

$$\mathrm{var}(I_n) \approx \Delta\omega\Delta\omega'_0 \left\{ \tfrac{1}{4}\delta_{n,0}\sigma_0^2 + \sum_{i=1}^{L} \omega_i^{2n}\sigma_i^2 \right\}, \quad (35)$$

where $\Delta\omega_0'$ is some average value of the wavelength-dependent $\Delta\omega'$ of eq. (34). The factor $\Delta\omega_0'/\Delta\omega$ renders $\mathrm{var}(I_n)$ practically independent of the choice of $\Delta\omega$, which is reasonable, and in an approximate way takes into account the positive correlations introduced by decreasing $\Delta\omega$. In practice, a useful value for $\Delta\omega_0'$ is obtained by setting $\lambda = \lambda_0$ in eq. (34), λ_0 being the wavelength of the incident neutrons; because $\Delta\lambda$ may be dependent on the scattering angle, we interpolate (in INTPOL) $\Delta\lambda$ to the particular k-values for which $S(k, \omega)$ and $\langle \omega^n \rangle$ are being calculated. Eq. (35) still neglects covariances generated by programs like DECO or MULCOR and takes into account the covariances of INTPOL only approximately. We think, however, that eq. (35) is an improvement compared to eq. (33) and a useful compromise of minimising computer time and estimating accurately the error of I_n. Taking into account the unknown error in M_n approximately, we assume that the relative error in $\langle \omega^n \rangle$ is equal to the relative error in I_n.

4. Applications

Two examples will be given of applications of the data correction procedure described in this paper. One is on the calculation of $S(k, \omega)$ from accurate measurements [1] on liquid ^{36}Ar at 120 K and 115 bar with the rotating-crystal spectrometer IN-4 at the High Flux Reactor of the Institut Laue–Langevin, Grenoble (see section 1). The second example is on the analysis of measurements on NH_4MnCl_3 at the Delft 2 MW reactor [19], to study the motions of ammonium-groups in a solid.

4.1. IN-4 measurements on liquid ^{36}Ar

In fig. 5 the flow diagram indicates how the correction procedure is applied in this case. We will

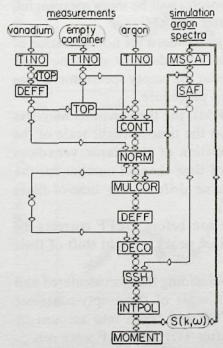

Fig. 5. Diagram of the data correction procedure as applied to accurate measurements on liquid ^{36}Ar. The double lines indicate the loop where the experimental $S(k, \omega)$ is used to calculate a new correction for multiple scattering.

comment on the flow diagram and give a few results to demonstrate the need to correct for resolution and duty-cycle overlap. We will compare the factor method for multiple-scattering correction with the subtraction method, using two rather different models for $S(k, \omega)$ as input for MSCAT.

4.1.1. The flow diagram (fig. 5)

Each box in the diagram of fig. 5 represents one of the programs discussed in the previous section; the circles represent different parts of the random-access input/output file, where intermediate results are being stored for inspection and for input into programs (see section 2). The final output is the fully corrected symmetrised, or classical $S(k, \omega)$ at a rectangular (k, ω)-grid for equidistant k- and ω-values. We will discuss the flow diagram in reverse starting from the output.

INTPOL: As discussed in the description of this program, the interpolation from the detector angles to the desired k-values is improved by simultaneously using the energy-gain and the energy-loss data by first symmetrising $S(k, \omega)$. This is only possible when all corrections have been performed. So INTPOL must be the last step, in contrast to the second example on NH_4MnCl_3, where not $S(k, \omega)$ but its Fourier transform the intermediate scattering function $F(k, t)$ is the desired result.

SSH: the correction for self-shielding can only be performed after the correction for multiple scattering (in MULCOR), since the self-shielding factor calculated by SAF is only valid for single scattering. The correction for resolution must also precede SSH, because the self-shielding factor is wavelength dependent and the time-of-flight resolution of the spectrometer causes an uncertainty in the wavelength of the detected neutrons.

DEFF(argon), DECO: because resolution and detector efficiency affect single scattering, multiple scattering and duty-cycle overlap in different ways, DEFF and DECO should be executed after MULCOR. Consequently, the simulation of the experiment by means of MSCAT should include the resolution of the spectrometer. In the real experiment the neutron spectra are first folded with the resolution function and then the neutrons are detected (for the moment neglecting the – usually small – contribution of the finite detector size to the overall time-of-flight resolution). Since the corrections should take place in reversed order, DEFF should precede DECO.

If – as is often the case – the detector efficiency and the self-shielding factor are smooth functions of the neutron wavelength, the order of DEFF, DECO and SSH is unimportant.

MULCOR: the simulated time-of-flight spectra are interpolated by MULCOR to the experimental detector angles and time channels. The comparison with the experimental spectra will be more meaningful, when these are normalised absolutely, so MULCOR should be executed after NORM.

NORM, DEFF(vanadium): in the present case vanadium slabs are used as standard for normalisation of the argon spectra. So the vanadium spectra must be fully corrected for both detector efficiency and background before applying NORM. In the present case the background from the empty spectrometer was very low and was subtracted separately before starting the actual correction procedure.

TOP: in order to convert the neutron intensities to $d^2\sigma/d\Omega d\lambda$ (in NORM), the time-channel numbers must be converted to the wavelength scale. TOP determines the position on the time-of-flight scale of the monitor peaks in the vanadium and the argon measurement, and the position of the elastic vanadium peaks. This information is used to determine the $(\lambda = \lambda_0)$-point in units of time-channel number for the argon spectra (λ_0 is the incoming neutron wavelength), and to determine drift of the time-of-flight reference point between the various measurements.

Because the detector efficiency is wavelength-dependent, TOP must be run before DEFF corrects the vanadium spectra. But since DEFF changes the shape of the elastic vanadium peaks, a slight shift of their position is possible and TOP is run again after DEFF.

CONT: for the subtraction of the empty-container measurement the self-shielding factors calculated and written on file by SAF are needed. A possible shift of the time-of-flight scale of the empty-container measurement with respect to the argon measurement is determined by TOP and taken into account by CONT. So the correction for container scattering can only be performed after TOP and SAF were run.

TINO: the first step for each of the three measurements is TINO, normalising all spectra to the same (arbitrary) unit of incoming neutron flux by means of the monitor in the incoming beam. Also a first estimate is made of the time-independent background.

SAF: this program uses part of the output of MSCAT and provides CONT with the sample attenuation factor and SSH with the self-shielding factor.

MSCAT: the simulation of the time-of-flight spectra is used by MULCOR for the correction for multiple scattering and duty-cycle overlap. MSCAT provides program SAF with the wavelength-dependent removal cross-sections of the sample and of the container.

The final $S(k, \omega)$-data are used to improve the model for MSCAT within the region in the (k, ω)-plane covered by the experiment. When the experimental $S(k, \omega)$-data are obtained, MSCAT and all the programs connected by the double line in fig. 5 are run again. The cycle is repeated until $S(k, \omega)$ does not change significantly any more. Improvement can be monitored by means of Q^2 (see section 3.3.1), using the detailed balance condition, and by means of the deviation of the first frequency moment $\langle\omega\rangle$ from its theoretical value $\omega_R = \hbar k^2/2M$. $\langle\omega\rangle$ is calculated from the experimental $S(k, \omega)$ by MOMENT.

4.1.2. Results

Fig. 6 shows the effect of skipping the resolution correction on $S(k, \omega = 0)/S(k)$ and on the full width at half-maximum (fwhm) of $S(k, \omega)$. In the present case the resolution correction is clearly essential for $k \lesssim 30$ nm^{-1}.

Fig. 7 shows the effect of deleting the correction for duty-cycle overlap by means of Q_{ij}^2 [eq. (22)], averaged over ω-intervals of 1 ps^{-1} and over all k where Q_{ij}^2 is defined. Also, the data for $S(k, \omega)$ at the 57 detector angles are given for $|\omega| = 12$ ps^{-1}, where the correction for duty-cycle overlap has a maximum influence on Q^2. It appears that Q^2 is a very sensitive probe for testing the influence of the various corrections.

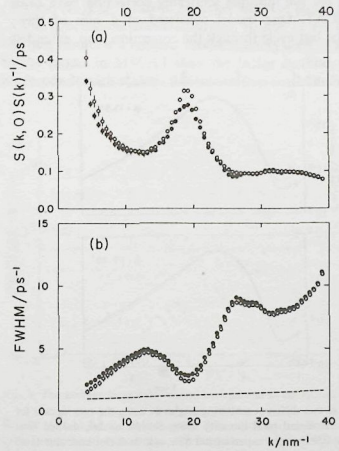

Fig. 6. Influence of the resolution correction by DECO on (a) the top of the dynamic structure factor, $S(k, \omega = 0)/S(k)$ and (b) on the full width at half-maximum (fwhm) of the dynamic structure factor. Dots: without resolution correction; circles: with resolution correction; dashed line: fwhm of the resolution.

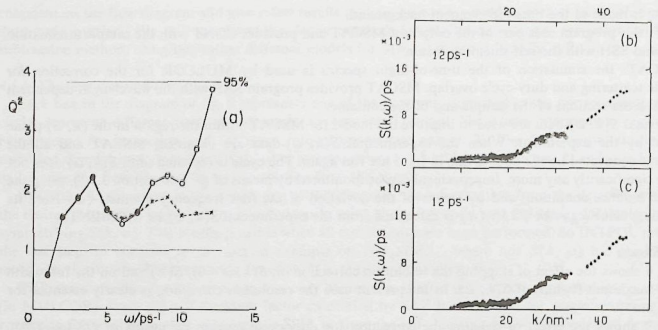

Fig. 7. Effect of deleting correction for duty-cycle overlap. (a) $Q^2(\omega)$, i.e. Q^2_{ij} averaged over all k-values and over ω-intervals of 1 ps^{-1}. The upper 95% limit and the mean of the χ^2-distribution with one degree of freedom are indicated by the light horizontal lines. Crosses: with overlap correction; circles: without overlap correction. (b, c) Energy-loss (circles) and energy-gain (dots) data for $S(k, \omega)$ at $|\omega| = 12$ ps^{-1} and for the 57 detector angles of the neutron scattering experiment vs k, (b) without and (c) with applying the correction for overlap.

Both the factor method and the subtraction method for the multiple scattering correction have been tested with two different models for $S(k, \omega)$ in MSCAT. One model consisted of a sum of three Lorentzians fitted to the experimental $S(k, \omega)$ [1] after the last cycle through the correction loop, extended

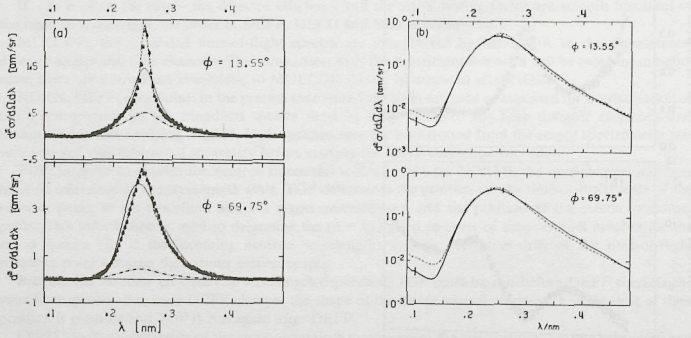

Fig. 8. (a) Comparison of simulated spectra with experimental spectra at two different scattering angles ϕ, using the two models for $S(k, \omega)$ mentioned in the text. Dots: experimental data; solid line: simulated total intensity using Sköld's model; dashed line: simulated total intensity using as a model the sum of three Lorentzians fitted to the experimental $S(k, \omega)$; dash-dot line: simulated multiple scattering using the latter model. (b) Simulated sum of multiple scattering and duty-cycle overlap if Sköld's model (solid line) or if the fitted sum of three Lorentzians (dashed line) is being used as model $S(k, \omega)$ in the simulation. The scattering angles are the same as in fig. 8a.

with simple hydrodynamics for $0 < k < k_{min}$, and with the Gram–Charlier (large-k) expansion of $S(k, \omega)$ according to Sears [20] for $k > k_{max}$. $\hbar k_{min}$ and $\hbar k_{max}$ are, respectively, the smallest and the largest momentum transfer in the neutron scattering experiment at which a meaningful fit with three Lorentzians is possible. The other model was the free-gas model, modified by the Sköld recipe [18] to yield the known zeroth and second frequency moment. For two scattering angles the simulated spectra are compared with the experimental spectra in fig. 8a. The sum of the resulting multiple scattering and intensity due to duty-cycle overlap is plotted in fig. 8b on a logarithmic scale as a function of λ. For this case we find that the multiple scattering does not depend much upon the choice of the model. The intensity due to overlap contains both multiple and single scattering, which explains the significant differences at small λ in fig. 8b. Fig. 9 shows the "time-independent background" as calculated by TINO and the fraction due to duty-cycle overlap determined by MULCOR. In MULCOR the difference of the two is used as an improved estimate of the real time-independent background.

The quality of the resulting $S(k, \omega)$ for four different cases (both the factor method and the subtraction method combined with each of the two models mentioned above) is measured by $Q^2(\omega)$ in fig. 10 and by $\langle\omega\rangle/\omega_R$ in fig. 11. $Q^2(\omega)$ is the result of averaging Q^2_{ij} over ω-intervals of 1 ps^{-1} and over all k-values where Q^2_{ij} is defined.

In addition, fig. 12 gives the resulting experimental $S(k, \omega)$ at the different detector angles on k-scale at $|\omega| = 7$ ps^{-1} for (a) the factor method combined with the Sköld model and for (b) the factor method combined with the model $S(k, \omega)$ fitted to the results of the previous iteration. According to $Q^2(\omega)$ and $\langle\omega\rangle$ in figs. 10 and 11 combination (b) gives the best results.

It should be noted that the error bars in fig. 11 include the contribution from systematic errors, as measured by the differences between the energy-gain and the energy-loss data [see section 3.3.1 eq. (21)], but that Q^2 measures these differences relative to the estimated statistical errors in $S(k, \omega)$. Because the factor method has a tendency to yield smaller estimates of the errors than the subtraction method [see eqs. (10) and (11)], Q^2 tends to be larger with the factor method, provided the systematic errors do not decrease.

The conclusions drawn from figs. 10 and 11 are that in the present example (1) the factor method yields the best results if a realistic model is being used in MSCAT and (2) the subtraction method is less sensitive to the model in MSCAT than the factor method, so that if it is not known to which extent the model corresponds with reality, the subtraction method should be applied.

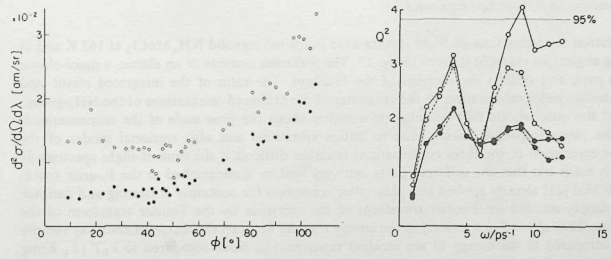

Fig. 9. The average time-independent background as calculated by TINO (circles) and the fraction due to duty-cycle overlap (dots).

Fig. 10. $Q^2(\omega)$ for the experimental $S(k, \omega)$-data after four alternative ways to correct the data for multiple scattering: i. using Sköld's model in the simulation with the factor method in MULCOR: circles, connected with solid line; ii. using the same model with the subtraction method: circles, connected with a dashed line; iii. using the fitted sum of three Lorenzians in the simulation with the subtraction method: dots, connected with a dashed line; iv. using the same model with the factor method: dots, connected with a solid line.

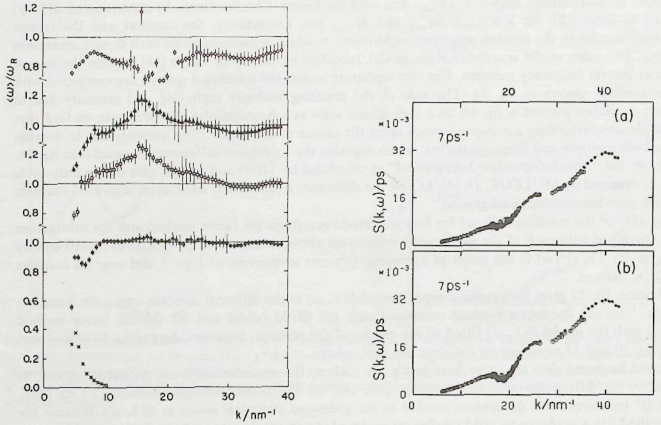

Fig. 11. The first frequency moment $\langle\omega\rangle$ of the experimental $S(k, \omega)$, resulting from the four alternative ways to correct the data for multiple scattering, as in fig. 10. From top to bottom: method i; method ii; method iii; method iv; (see fig. 10). $\omega_R = \hbar k^2/2M$ is the recoil. The crosses indicate the contribution of the model [M_n in eq. (31)] to the total moment for case iv; at $k \geq 10$ nm^{-1} this contribution is negligible. The error bars represent 2 × the standard deviation according to eq. (35).

Fig. 12. Experimental energy-loss (circles) and energy-gain (dots) data for $S(k, \omega)$ at $|\omega| = 7$ ps^{-1} and for all 57 detector angles, using the factor method in MULCOR. (a) Using the fitted sum of three Lorentzians in the simulation. (b) Using Sköld's model.

4.2. *Rotational motions of NH_4-groups in a solid*

Incoherent neutron scattering time-of-flight spectra were measured on solid NH_4MnCl_3 at 163 K and at several scattering angles; an example is given in fig. 13. The spectrum consists of an elastic, a quasi-elastic and an inelastic part, and reflects the motions of the H-atoms. The ratio of the integrated elastic and quasi-elastic intensities yields information on the symmetry of the preferred orientations of the NH_4-groups and the shape of the quasi-elastic part contains information about the time scale of the reorientational motions [19]. The inelastic part is mainly due to lattice vibrations and also torsional modes of the NH_4-groups. The separation of the three contributions is rather difficult if the time-of-flight spectrum is being used, but it turns out that the different parts can very well be distinguished in the Fourier space. Bregman and De Mul [21] already applied this idea: after correction for container scattering and detector efficiency, they simply divided the Fourier transform of the spectrum by the Fourier transform of the resolution function. They showed that as long as the energy transfer between the scattered neutrons and the sample is small compared to the energy of the incident neutrons and small compared to $k_B T$ (k_B being Boltzmann's constant and T the temperature of the sample), the result is a good approximation of the intermediate incoherent scattering function $F_i(k, t)$ which is the Fourier transform of $S_i(k, \omega)$, the self part of the dynamical structure factor $S(k, \omega)$.

This approximation can not be used in the present case, where the high inelastic intensity at large ω (see fig. 13) results in disturbing oscillations in the Fourier transform. Therefore, the time-of-flight spectra are converted to the symmetrised $S_i(k, \omega)$ before Fourier transformation and deconvolution. Interpolation

from the scattering angles to constant k was not attempted, because the number of detector angles was insufficient; the results will demonstrate that this is not necessary either.

Fig. 14 gives the flow diagram of the correction procedure applied in the present case. The normalisation and the resolution were determined by a measurement on the same sample at a lower temperature of 96 K. The width of the quasi-elastic peak at this temperature is expected to be small compared to the resolution of the spectrometer. This measurement is also corrected for container scattering and detector efficiency and converted to $S_i(k, \omega)$. The Fourier transform of $S_i(k, \omega)$ at 163 K is divided by the Fourier transform of $S_i(k, \omega)$ at 96 K. The result is given in fig. 15.

Since $S_i(k, \omega)$ was symmetrised before the Fourier transformation, the intermediate scattering function $F_i(k, t)$ should be real. A non-zero Im $F_i(k, t)$ indicates asymmetries in $S_i(k, \omega)$ due to the neglect of the correction for multiple scattering and due to the fact that $S_i(k, \omega)$ was not interpolated to constant k. As long as Im $F_i(k, t)$ is small compared to Re $F_i(k, t)$ these approximations are justified, as is the case for $t \lesssim 3.5$ ps.

Since inelastic scattering gives rise to a broad spectrum for the measurements at both temperatures, its influence on $F_i(k, t)$ is expected to be significant only near $t = 0$. Self-shielding is approximately ω-independent and equal for both measurements, so it is automatically taken care of when dividing the Fourier transforms. The elastic scattering causes the limit of $F_i(k, t)$ for $t \to \infty$ to be constant, as can be seen in fig. 15. Subtraction of this constant yields – except for two or three points near $t = 0$ – the Fourier transform of the quasi-elastic part of $S_i(k, \omega)$.

A simple model [19] was fitted to Re $F_i(k, t)$, deleting the three points at and nearest to $t = 0$:

$$F_i(k,t) = C(k)\{A(k) + [1 - A(k)]e^{-t/\tau}\}, \tag{36}$$

where A is the part due to elastic scattering, C the ratio of the Debije–Waller factors at 163 K and at 96 K, and τ the relaxation time for rotational jump-diffusion. The model implies that the time the NH_4-group needs to rotate from one position to another is much smaller than the time the group resides in a preferential orientation. As can be seen from fig. 15 the fit is satisfactory, and the present correction

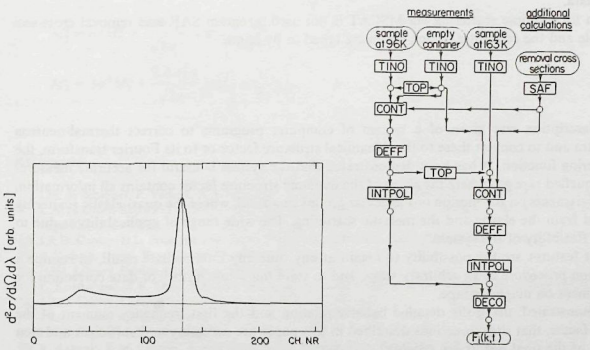

Fig. 13. Time-of-flight spectrum from solid $NH_4Mn\,Cl_3$ at 163 K at a scattering angle of 83°, after correction for container and detector efficiency. The incoming neutron wavelength was 0.41 nm, the flightpath 1.2 m and the time channel width 8 μs.

Fig. 14. Flow diagram for the data correction procedure applied to the measurements on $NH_4Mn\,Cl_3$ at 163 K. The scattering by the sample at 96 K with the same density has been measured to determine the normalisation and resolution.

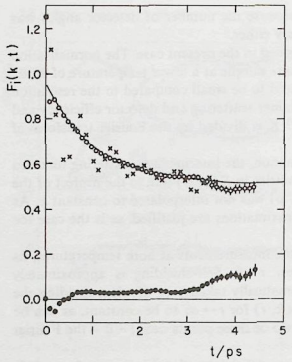

Fig. 15. The Fourier transform, of $S(k, \omega)$ at 83° for NH_4MnCl_3 at 163 K. The function is approximately equal to the intermediate incoherent scattering function $F_i(k, t)$ at $k = 20.4$ nm^{-1}. Circles: Re $F_i(k, t)$; dots: Im $F_i(k, t)$; crosses: Re $F_i(k, t)$ according to the method of Bregman and De Mul [21]; solid line: sum of constant and single exponential fitted to Re $F_i(k, t)$ (circles). The error bars are calculated as described in section 3.

procedure is a substantional improvement compared to the method of Bregman and De Mul [21].

Instead of subtracting the multiple scattering after performing a computer simulation as in the case of liquid ^{36}Ar, the multiple scattering might be calculated from the model, eq. (36), and included in the fit to the experimental data.

Since correction for multiple scattering via MSCAT is not used, program SAF uses removal cross-sections for the sample and the container, which are being typed in by hand.

5. Conclusions

An extensive description was given of a system of computer programs to correct thermal-neutron time-of-flight spectra and to convert these to the dynamical structure factor or to its Fourier transform, the intermediate scattering function. It has been demonstrated that the system is useful for accurate measurements on, e.g., a liquefied rare gas where the *shape* of the dynamic structure factor contains all information, as well as for measurements on the motion of molecular groups in a solid, where the quasi-elastic scattering has to be separated from the elastic and the inelastic scattering. The wide range of applicability is due to the high degree of flexibility of the system.

Other important features are the possibility to regain at any time any intermediate result, to resume a part of the correction procedure at an arbitrary stage, and to store the whole history of data correction for a particular experiment on magnetic tape.

It has been demonstrated, using the detailed balance relation and the first frequency moment of the dynamic structure factor, that the corrections described in this paper are necessary and sufficient and that the error estimates of the final results are reliable.

Prof. J.R.D. Copley is acknowledged for providing some of his computer programs, such as the modified version of MSCAT. J.C. van Rijs assisted in the construction and implementation of the correction procedure. Profs. E.G.D. Cohen, L.A. de Graaf and J.J. van Loef critically read the manuscript and gave valuable advise.

Appendix

If for $\omega > \omega_L$

$$S_M(k,\omega) = \frac{A}{\sigma\sqrt{2\pi}} \exp\left[-\frac{\left(\omega - \frac{1}{2}\hbar\beta\sigma^2\right)^2}{2\sigma^2}\right],$$

then M_n for $n = 0, \ldots, 4$ is given by:

$$M_0 = \frac{A}{2}\left[\operatorname{erfc}\left\{\frac{\left(\omega_L + \frac{1}{2}\hbar\beta\sigma^2\right)}{\sigma\sqrt{2}}\right\} + \operatorname{erfc}\left\{\frac{\left(\omega_L - \frac{1}{2}\hbar\beta\sigma^2\right)}{\sigma\sqrt{2}}\right\}\right],$$

$$M_1 = \tfrac{1}{2}\hbar\beta\sigma^2 M_0 + A\sigma\sqrt{\frac{2}{\pi}}\ \sinh\left(\tfrac{1}{2}\beta\hbar\omega_L\right) \exp\left\{-\frac{1}{2\sigma^2}\left(\omega_L^2 + \tfrac{1}{4}\hbar^2\beta^2\sigma^4\right)\right\},$$

$$M_2 = \sigma^2 M_0 + \tfrac{1}{2}\hbar\beta\sigma^2 M_1 + \frac{A\omega_L\sigma}{\sqrt{2\pi}}\left[\exp\left\{-\frac{\left(\omega_L - \frac{1}{2}\hbar\beta\sigma^2\right)^2}{2\sigma^2}\right\} + \exp\left\{-\frac{\left(\omega_L + \frac{1}{2}\hbar\beta\sigma^2\right)^2}{2\sigma^2}\right\}\right],$$

$$M_3 = 2\sigma^2 M_1 + \tfrac{1}{2}\hbar\beta\sigma^2 M_2 + A\omega_L^2\sigma\sqrt{\frac{2}{\pi}}\ \sinh\left(\tfrac{1}{2}\beta\hbar\omega_L\right) \exp\left\{-\frac{\left(\omega_L^2 + \frac{1}{4}\hbar^2\beta^2\sigma^4\right)}{2\sigma^2}\right\},$$

$$M_4 = 3\sigma^2 M_2 + \tfrac{1}{2}\hbar\beta\sigma^2 M_3 + \frac{2A\omega_L^3\sigma}{\sqrt{2\pi}}\ \cosh\left(\tfrac{1}{2}\hbar\beta\omega_L\right) \exp\left\{-\frac{\left(\omega_L^2 + \frac{1}{4}\hbar^2\beta^2\sigma^4\right)}{2\sigma^2}\right\}.$$

For the classical approximation we simply set $\hbar = 0$:

$$M_1^c = M_3^c = 0,$$

$$M_0^c = A\ \operatorname{erfc}\left\{\frac{\omega_L}{\sigma\sqrt{2}}\right\},$$

$$M_2^c = \sigma^2 M_0^c + \frac{2A\omega_L\sigma}{\sqrt{2\pi}}\ \exp\left\{-\frac{\omega_L^2}{2\sigma^2}\right\},$$

$$M_4^c = 3\sigma^2 M_2^c + \frac{2A\omega_L^3\sigma}{\sqrt{2\pi}}\ \exp\left\{-\frac{\omega_L^2}{2\sigma^2}\right\}.$$

References

[1] I.M. de Schepper, P. Verkerk, A.A. van Well and L.A. de Graaf, Phys. Rev. Lett. 50 (1983) 974; A.A. van Well, P. Verkerk and L.A. de Graaf, Report 132–82–7/1 (IRI, Delft, 1984); A.A. van Well, P. Verkerk, L.A. de Graaf, J.-B. Suck and J.R.D. Copley, Phys. Rev. A (in press).
[2] J.R.D. Copley, D.L. Price and J.M. Rowe, Nucl. Instr. and Meth. 107 (1973) 501; 114 (1974) 411.
[3] P. Verkerk, Comp. Phys. Comm. 25 (1982) 325.
[4] IMSL Library, Edition 9 (Houston, Texas, 1982).
[5] L. Koester and W.B. Yelon, Summary of low energy neutron scattering lengths and cross sections (ECN, Petten, 1982).
[6] J.R.D. Copley, Comp. Phys. Comm. 7 (1974) 289; 21 (1981) 431.
[7] J.R.D. Copley and S.W. Lovesey, Rep. Prog. Phys. 38 (1975) 461.
[8] J.R.D. Copley et al., to be published.
[9] R. Aamodt, K.M. Case, M. Rosenbaum and P.F. Zweifel, Phys. Rev. 126 (1962) 1165.
[10] B.R. Martin, Statistics for Physicists (Academic Press, London, 1971).
[11] V.F. Sears, Adv. Phys. 24 (1975) 1.
[12] M. Kamal, S.S. Malik and D. Rorer, Phys. Rev. B 18 (1978) 1609.
[13] B.J.M. Vernooy, M.Sc. Thesis, IRI, Delft (1981) in Dutch.

[14] W. Marshall and S.W. Lovesey, Theory of thermal neutron scattering (Clarendon, Oxford, 1971).
[15] H. Fredrikze, Mol. Phys. 48 (1983) 903.
[16] R.D. Puff, Phys. Rev. 137 (1965) 406.
[17] P.G. De Gennes, Physica 25 (1959) 825.
[18] K. Sköld, Phys. Rev. Lett. 19 (1967) 1023.
[19] C. Steenbergen, L.A. de Graaf, L. Bevaart, J. Bartolomé and L.J. de Jongh, J. Chem. Phys. 70 (1979) 1450.
[20] V.F. Sears, Phys. Rev. 185 (1969) 200.
[21] J.D. Bregman and F.F.M. de Mul, Nucl. Instr. and Meth. 93 (1971) 109.

Computer Physics Communications 25 (1982) 325–345
North-Holland Publishing Company

III

RESOLUTION CORRECTION: A SIMPLE AND EFFICIENT ALGORITHM WITH ERROR ANALYSIS

Peter VERKERK

Interuniversitair Reactor Instituut, 2629 JB Delft, The Netherlands

Received 15 December 1981

A new procedure to correct experimental spectra for instrumental resolution is described. A-priori knowledge is not used, in contrast to other deconvolution methods; consequently the range of applications is very wide, while the necessary computations are simple. Use is being made of the Fast Fourier Transform technique, which makes the method suitable to process large amounts of data. Not only the propagation of the random statistical errors but also the contribution from systematic errors, which arise in any method, is estimated. The validity of the method is demonstrated by means of numerical tests taken from different sources in the literature.

1. Introduction

In many experiments the resolution of the measuring device is of the order of the size of the details the experimentalist wants to study, and consequently the relevant information is distorted. The restoration of the original signal is hampered by the ever present random noise and the fact that often the rate of distortion (i.e. the resolution function) is not exactly known. In addition, even if the measurements were exact and the resolution function were exactly known, it is not always possible to eliminate the resolution effect (see e.g. Seidman [21]).

Suppose we want to measure quantity $S_0(x)$ (e.g. a spectrum) by means of an instrument with a resolution $R_0(x, x')$. $R_0(x, x')$ gives the response of the instrument at x to an impulse at x'. The measured signal is given by

$$M_0(x) = \int R_0(x, x')\, S_0(x')\, \mathrm{d}x' + Z_0(x), \qquad (1)$$

where $Z_0(x)$ is the random noise.

Usually the data $M_0(x)$ are collected at a finite, discrete set x_j, $j = 1, \ldots, N$. If $M(x_j)$ is an average of $M_0(x)$ over a channel with finite width Δx_j, eq. (1) becomes

$$M(x_j) = \int R(x_j, x')\, S_0(x')\, \mathrm{d}x' + Z_j \qquad (2)$$

with

$$R(x_j, x') = \frac{1}{\Delta x_j} \int_{x_j - \frac{1}{2}\Delta x_j}^{x_j + \frac{1}{2}\Delta x_j} R_0(x, x')\, \mathrm{d}x$$

and Z_j the random noise in channel number j.

The problem is to estimate $S_0(x)$ from the Fredholm integral equation of the first kind (2) given $M(x_j)$ and $R(x_j, x')$ $(j = 0, \ldots, N-1)$, which is an ill-posed problem. A nearly inexhaustible amount of literature exists on the subject, since every experiment needs a method of deconvolution adapted to its specific demands. Reviews have been given by Turchin, Kozlov and Malkevich in 1971 [1], by Frieden in 1975 [2] and by Biraud in 1976 [3]. All methods leading to useful results incorporate a-priori knowledge about $S_0(x)$ in one way or another (e.g. the fact that $S_0(x)$ is a smooth or a positive definite function). Very sophisticated algorithms have been developed that will give satisfactory results in many experimental situations, but generally they have two drawbacks that could be prohibitive in certain circumstances. Firstly , they are relatively (computer-)time consuming; for instance Kennett et al. [4] presented an algorithm, using Bayesian techniques, that needed for some of the numerical tests more than 2000 iterations before a fully satisfactory estimate $\hat{S}(x)$ of the true solution $S_0(x)$ was reached. Secondly, due to the non-linear nature of the algo-

0010-4655/82/0000–0000/$02.75 © 1982 North-Holland

rithms, calculation of the noise propagation is difficult and time consuming too: Routti and Sandberg [5] applied a non-linear minimisation algorithm to preserve positivity of the estimated solution $\hat{S}(x)$ and one of the methods they propose to estimate the confidence band is to unfold $M(x)$ several times using different physically realistic perturbations.

In thermal neutron inelastic scattering experiments carried out with advanced time-of-flight spectrometers a large number of spectra (of the order of a hundred each with several hundred channels) can be measured simultaneously. If in addition some parameter of the sample as for instance temperature or pressure is varied, it is clear that one needs a fast and fully automatic computer program to correct such an amount of spectra for the resolution of the spectrometer. As in the literature no method has been found that meets these demands and gives reliable error bounds simultaneously, a new method has been developed and is presented in this paper.

The proposed algorithm does not use any a-priori knowledge about $S_0(x)$, is very simple and fast, and in addition gives confidence limits for the estimated solution $\hat{S}(x)$. In section 2 the deconvolution procedure is described, section 3 treats the error analysis and section 4 gives results of a few test cases, taken from the literature.

2. Deconvolution procedure

Our aim is to find an approximate solution $\hat{S}(x)$ for

$$M(x_j) = \int R(x_j, x')\, S_0(x')\, \mathrm{d}x' + Z_j \qquad (2)$$

with given $M(x_j)$ and $R(x_j, x')$, $j = 0, \ldots, N-1$. The random noise Z_j is assumed to have zero mean and to be uncorrelated with Z_k, $k \neq j$. The method presented below makes use of the Discrete Fourier Transform (DFT), so Fast Fourier Transform algorithms can be applied to minimise computing times. This imposes restrictions on the applicability.

Firstly, the resolution function must be translation invariant:

$$R(x, x') = R(x - x')$$

and secondly, the sampling of $M(x)$ must be equidistant in x (the latter condition can always be fulfilled by simple interpolation, but then the covariances of $M(x_j)$ are no longer zero). In the third place eq. (2) is approximated by

$$M(x_j) = \Delta x \sum_k R(x_j - x_k)\, S(x_k) + Z_j$$

or in short notation:

$$M_j = \Delta x \sum_k R_{j-k} S_k + Z_j. \qquad (3)$$

If the functions M, R, S and Z are extended periodically with a period of $(N-1)\,\Delta x$, the discrete convolution theorem [6] applies:

$$m_k = \Delta x\, r_k s_k + z_k$$

with the DFT and its inverse defined as:

$$f_k = \sum_{j=0}^{N-1} F(x_j) \exp(\mathrm{i}\, jk 2\pi/N), \qquad (4a)$$

$$F(x_j) = \frac{1}{N} \sum_{k=0}^{N-1} f_k \exp(-\mathrm{i}\, jk 2\pi/N), \qquad (4b)$$

where $\mathrm{i} = \sqrt{-1}$ and $f_k\, \Delta x$ is approximately equal to the continuous Fourier transform

$$f(y_k) = \int_{-\infty}^{\infty} F(x) \exp(\mathrm{i} x y_k)\, \mathrm{d}x$$

at $y_k = k\, \Delta y$ with $\Delta y = 2\pi N/\Delta x$.

In general, $S_k \neq S_0(x_k)$, but in appendix A it is demonstrated that to a good approximation

$$S_k = \frac{1}{\Delta x} \int_{x_k - \frac{1}{2}\Delta x}^{x_k + \frac{1}{2}\Delta x} S_0(x)\, \mathrm{d}x.$$

In other words, the solution of eq. (3) is an average over channels of the true solution $S_0(x)$.

The DFT of S_j is equal to

$$s_k = \frac{1}{\Delta x} \left\{ \frac{m_k}{r_k} - \frac{z_k}{r_k} \right\},$$

where m_k, r_k and z_k are the DFT's of M_j, R_j and Z_j, respectively. (Note that $r_0 = 1/\Delta x$ if the resolution function $R(x)$ is normalised to 1.) Since z_k is unknown, the true s_k is estimated by

$$\hat{s}_k = m_k/(r_k\, \Delta x) = s_k + z_k/(r_k\, \Delta x) \qquad (5a)$$

or in terms of continuous Fourier transforms:

$$\hat{s}(y) = m(y)/r(y) = s_0(y) + z(y)/r(y). \qquad (5b)$$

If y becomes large enough, $r(y)$ and $s_0(y)$ will eventually approach zero in contrast to $z(y)$, and the second term in the right hand sides of (5) will dominate $\hat{s}(y)$ and $\hat{s}_k$, respectively. Several papers [7–14] have been published on the problem of amplified noise in the higher-order Fourier components of $S_0(x)$. Most authors describe different variants of the low-pass filter, that damps $\hat{s}(y)$ for $|y|$ larger than some value Y. As a result the noise term $x(y)/r(y)$ remains bounded, but on the other hand the effect of the factor $1/r(y)$, which amplifies $m(y)$ and is supposed to eliminate the resolution effect, is partly or completely overruled by the effect of the filter, which damps $m(y)$. In other words: a complete elimination of the effects due to instrumental resolution is impossible; peaks in $S_0(x)$ will always be broadened by the filter.

There are two different types of error in $\hat{S}(x)$: (i) statistical errors, which are amplified by the deconvolution operation and (ii) systematic errors due to the filtering, which are largest in peaks and may also cause unphysical oscillations in the deconvolved signal. Error type 1 increases with increasing cut-off Y, while error type 2 decreases. The form of the filter can be optimised to produce a minimum of artificial oscillations in $\hat{S}(x)$ (see e.g. De Mul and Bregman [10] and Cantoni et al. [13]). Rotondi [11] used the weighted least squares regression to expand $M(x)$ and $R(x)$ in a Fourier series. It can be demonstrated by comparing the Fourier components m_k and r_k obtained in this way with those obtained by (4), that this is also a variant of the low-pass filter with its inherent underestimation of narrow peaks and production of oscillations in $\hat{S}(x)$. Wild et al. [12] fit some model function to $\hat{s}(y)$ by means of weighted least squares to eliminate $z(y)/r(y)$ in (5). However, they wrongfully neglect the covariances of the Fourier components m_k: inclusion of the complete variance-covariance matrix of m_k in the weighted least squares calculations requires an extra $N \times N$ matrix inversion. Also, if $z(y) \gg m(y)$ (generally for large $|y|$) and if $s(y) \to 0$ for increasing $|y|$, it is uncertain whether the fitted function will approach zero, due to the small weight of $m(y)/r(y)$ in the least squares calculation for these values of y, unless the model function has this property.

The present method is based on the observation that the Fourier transform $m(y)$ of $M(x)$ does not contain significant information for $|y| > Y$ and consequently only a limited number (say K) of Fourier coefficients m_k contains the essential information from the measurement of $M(x)$ (see also ref. [14]). Below will be indicated how to determine whether a Fourier coefficient contains significant information. Except in the case of extremely good resolution or statistical accuracy K is smaller than the number N of samples $M(x_j)$. Deleting the $N-K$ least significant Fourier coefficients is equivalent to a rectangular low-pass filter. As nearly every paper on deconvolution points out, the application of a rectangular filter to $\hat{s}(y)$ causes unphysical oscillations in $\hat{S}(x)$ due to the discontinuity in $\hat{s}(y)$ at $y = \pm Y$. It is demonstrated below how this can be avoided.

If the Fourier transform $s(y)$ of $S(x)$ beyond $|y| = Y$ is not known, the behaviour of $S(x)$ at points x closer than $\Delta x = \pi/Y$ is unknown [6]. A decrease of Δx (e.g. by interpolation) implies some postulate for the missing part of $s(y)$, $|y| > Y$. The aforementioned oscillations caused by the rectangular low-pass filter are a consequence of the assumption $s(y) = 0$ for $|y| > Y$, which is evidently wrong except for functions $S(x)$ with a band limit Y. So the rectangular low-pass filter method can be improved by making more realistic assumptions about $s(y)$ for $|y| > Y$, e.g. by using a-priori information on $S(x)$. Alternatively, if such knowledge is not available or if one does not want to use it in order to keep the deconvolution method as simple as possible, $\hat{S}(x)$ should be calculated at $x_j = j\, \Delta x'$ with $\Delta x' = \pi/Y$ and $j = 0, \ldots, K-1$. In most cases $K < N$ and $\Delta x'$ will be larger than the original sampling interval Δx of $M(x)$. This is no loss of information, but the quality of the experiment that yielded $M(x_j)$ does not permit estimation of $S(x)$ at more than K points spaced $\Delta x'$. These arguments might be illustrated by the following.

Let us regard as in ref. [9] the truncated function $s(y)$ as a sum of the step function $c(y) = s(Y)\, U(Y-y)$ and the continuous function $\{s(y) - s(Y)\}\, U(Y-y)$, where $U(y)$ is the Heaviside step function ($U(y) = 0$ for $y < 0$, $U(y) = 1$ for $y > 0$).

The Fourier transform of $c(y)$ is:

$$S(Y)\ \sin(xY)/\pi x. \tag{6}$$

This expression has zeros for $x_j = j\pi/Y$ ($j \neq 0$), and the oscillations in $S(x)$ due to the discontinuity in $s(y)$ at $y = Y$ are at least reduced by calculating it at these x_j. This does not exclude oscillations with a different period in $S(x)$ due to the discontinuities in the derivatives of $s(y)$ at $y = Y$, but in most cases their effect is smaller as will be demonstrated below with a few examples.

To summarise: $M(x)$ and $R(x)$ are sampled at x_j, $j = 0,\ldots,N-1$ with constant Δx. The DFT gives m_k and r_k, $k = 0,\ldots,N-1$. To find the corrected spectrum the K most significant coefficients m_k are selected and the inverse DFT is applied to $\hat{s}_k = m_k/r_k$, $k = 0,\ldots,K-1$:

$$\hat{S}(x_l) = \frac{1}{N} \sum_{K=0}^{k-1} \hat{s}_k \exp(-i2\pi lk/K) \tag{7}$$

with $x_l = lN\,\Delta x/K$. If it is assumed that $S(x)$ is a smooth function, one can use for instance spline interpolation to construct some $\hat{S}(x)$ at the original sampling points $x = x_j = j\,\Delta x$ from the given set $\hat{S}(x_l)$, but this is optional and completely independent from the deconvolution procedure.

The statements above are illustrated with a few numerical examples in figs. 1–3. A Gaussian, a Lorentzian and an exponential are sampled at 128 points, the DFT is applied and the Fourier series are truncated to 16 terms (the DFT of the Lorentzian also to 8 terms). The results of applying (4b) after replacing the deleted Fourier components by zeros and of applying (7) are compared with the original functions. In all three cases the use of (7) combined with cubic spline interpolation gives on the average smaller errors than the use of (4b) after setting Fourier components to zero. The assumption of smooth behaviour of $S(x)$ between the data at the increased sampling interval was justified in these examples (the error bars in figs. 1–3 will be explained in the next section on error analysis).

In appendix B is indicated how the sequences $M(x_j)$, $R(x_j)$, m_k and r_k should be arranged and how to choose the Fourier components that are to be deleted.

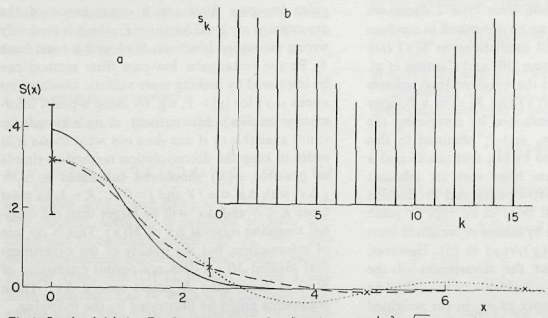

Fig. 1. Result of deleting Fourier components of a Gaussian $\exp(-\frac{1}{2}x^2)/\sqrt{2\pi}$, solid line in (a), which is sampled at 128 points symmetrically around $x = 0$ with sampling interval $\Delta x = 0.3$. Crosses indicate the inverse fast Fourier transform of the 16 Fourier components shown in (b) (see appendix A) yielding an estimate of the original Gaussian at an increased sampling interval $128\,\Delta x/16$. The dashed line connects these points by means of a cubic spline and the dotted line is the result of the inverse Fourier transform of the same Fourier components shown in (b), however with replacing the deleted Fourier components by zeros. The error bars are explained in section 3.

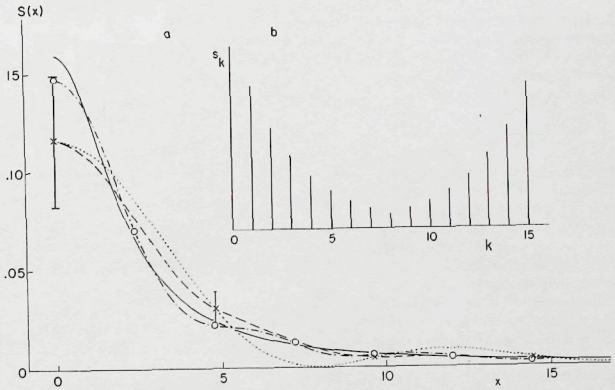

Fig. 2. Same as fig. 1 for a Lorentzian $2/(\pi(4+x^2))$. Also the effect of decreasing the number of retained Fourier components from 16 to 8 is shown. Circles and dash–dot line for 16 Fourier components, without and with added zeros, respectively; crosses and dotted line similar for 8 Fourier components and dahsed line for cubic spline interpolation between estimates of original Lorentzian at increased sampling interval $128\,\Delta x/8$.

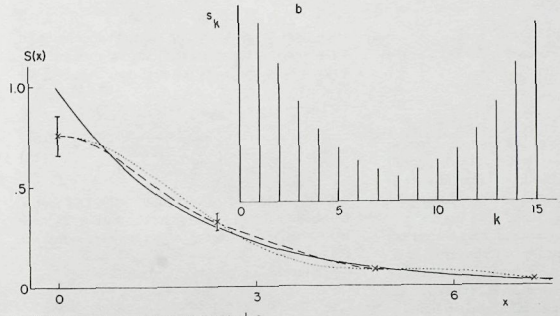

Fig. 3. Same as fig. 1 for exponential $\exp(-\frac{1}{2}x)$.

To find useful criteria to determine an optimal cut-off index K of the Fourier series, we note that the terms m_k in the truncated series are identical to the parameters of an unweighted least squares fit to $M(x_j)$ with orthogonal functions

$$\Psi_k(x) = \frac{1}{N} \exp\left[-ik\frac{(x_j - c)}{\Delta x}\frac{2\pi}{N}\right],$$

($x_j = j\,\Delta x + c$) and some of the statistical criteria in least squares fitting can be adopted to determine the optimum number of parameters which is the best value of K in the sense of reducing oscillations in $\hat{S}(x)$ without excessive smoothing. Further details are given in appendix C.

One could argue that application of the unweighted least squares method is incorrect if the M_j have different variances σ_j. But if, as is often the case, σ_j increases with increasing M_j, peaks will have relatively small weights in the weighted least squares method and consequently the systematic underestimation of these peaks will be worse than in the unweighted method. Furthermore, in the weighted method no use can be made of the orthogonality of the functions $\Psi_k(x)$, which implies more computational effort: the Fast Fourier Transform techniques cannot be applied, adding an extra component to the Fourier series requires recalculating all previous ones, and the error analysis is more complicated (see Rotondi [11]).

3. Error analysis

3.1. Propagation of experimental errors

Suppose the variances of the random errors in M_j and R_j are known for $j = 0,\ldots,N-1$, and all M_j and R_j are uncorrelated. In appendix D is shown how to calculate the variance–covariance matrix $\mathrm{var}(\hat{S}_j, \hat{S}_m)$ of $\hat{S}_j$; j and $m = 0,\ldots,K-1$. Note that in general the $\hat{S}_j$ are mutually correlated. If $R(x)$ is known theoretically or if the errors in R_j are small compared to those in M_j, the last four terms in the right hand side of eq. (D.4) vanish. Combining (D.2), (D.4) and (D.6) it is straightforward to prove the following simple result for this case:

$$\mathrm{var}(\hat{S}_j, \hat{S}_m) = \frac{1}{N^2}\sum_{k,l=0}^{K-1} \exp\left(-\frac{i\,jk2\pi}{K}\right) \times c_{kl}\exp\left(-\frac{iml2\pi}{K}\right) \qquad (8)$$

with

$$c_{kl} = \frac{(\tilde{\sigma}^2)_{k'+l'}}{r_{k'}r_{l'}(\Delta x)^2} \qquad (k'+l') \bmod N \qquad (9)$$

and

$$(\tilde{\sigma}^2)_k = \sum_{j=0}^{N-1} \sigma_j^2 \exp(i\,jk2\pi/N), \qquad (10)$$

where $k' = k$ for $k = 0,\ldots,K/2$ and $k' = k+N-K$ for $k = K/2+1,\ldots,K-1$ and similar for l'.

Example

A simple example might be enlightning. Let $\sigma_j = 1$ for $j = 0,\ldots,N-1$. The DFT is $(\tilde{\sigma}^2)_k = N\delta_{k0}$ and according to (8) and (9)

$$\mathrm{var}(\hat{S}_j, \hat{S}_m) = \frac{1}{(\Delta x)^2}\left[V_{m-j} - \frac{(-1)^{m+j}}{2N|r_{K/2}|^2}\right] \qquad (11)$$

with

$$V_j = \frac{1}{N}\sum_{k=0}^{K-1}\frac{1}{|r_k|^2}\exp(-i\,jk2\pi/K), \qquad (12)$$

where r_k refers to the truncated Fourier series (note that the last term in the right hand side of eq. (11) is due to setting the imaginary part of $s_{K/2}$ to zero – see appendix B – and does not occur for $K = N$).

The variance of $\hat{S}_j$ is

$$\mathrm{var}(\hat{S}_j) = \frac{1}{N(\Delta x)^2}\left[\sum_{l=0}^{K-1}\frac{1}{|r_l|^2} - \frac{1}{2|r_{K/2}|^2}\right] \qquad (13)$$

which is independent of j (due to the fact that σ_j is the same for all j) and increases with K. If there is no resolution effect in M_j, (13) yields $\mathrm{var}(\hat{S}_j) = (K - 1/2)/N$.

To give a numerical example let

$$R(x) = \frac{1}{\sigma_R\sqrt{2\pi}}\exp\left(-\frac{x^2}{2\sigma_R^2}\right)$$

Table 1
Correlation matrix $\mathrm{cor}(\hat{S}_j, \hat{S}_k)$ of $\hat{S}_j$, $j = 0,\ldots,K/2$, if the variance σ_j^2 of M_j is equal to 1 for all j and $R(x)$ is a Gaussian with standard deviation $\sigma_R = \sqrt{0.1}$. The sampling interval $\Delta x = 0.3$ and $K = 16$

j: 0	1	2	3	4	5	6	7	8	k
1	−0.04	0.01	−0.01	0.01	−0.01	0.01	−0.01	0.01	0
	1	−0.04	0.01	−0.01	0.01	−0.01	0.01	−0.01	1
		1	−0.04	0.01	−0.01	0.01	−0.01	0.01	2
			1	−0.04	0.01	−0.01	0.01	−0.01	3
				1	−0.04	0.01	−0.01	0.01	4
					1	−0.04	0.01	−0.01	5
						1	−0.04	0.01	6
							1	−0.04	7
								1	8

and let $R(x)$ and $m(x)$ be sampled at $x_j = (j - 63)\,\Delta x$, $j = 0,\ldots,127$ with $\Delta x = 0.3$. The DFT of $R(x)$ is approximately equal to the continuous Fourier transform divided by Δx:

$$r_k \approx \frac{1}{\Delta x}\exp\left(-\frac{y_k^2\sigma_R^2}{2}\right)$$

with $y_k = k\,\Delta y$ for $k = 0,\ldots,K/2$, and $y_k = -(k-K/2)\,\Delta y$ for $k = K/2+1,\ldots,K-1$, with $\Delta y = 2\pi/(N\,\Delta x)$.

If $K = 16$ one obtains for $\sigma_R^2 = 0$ (no resolution effect), 0.1, 0.5 $\mathrm{var}(\hat{S}_j) = 0.12$, 0.13, 0.16, respectively. The correlation matrix

$$\mathrm{cor}(\hat{S}_j, \hat{S}_m) = \frac{\mathrm{var}(\hat{S}_j, \hat{S}_m)}{\left\{\mathrm{var}(\hat{S}_j)\,\mathrm{var}(\hat{S}_m)\right\}^{1/2}} \qquad (14)$$

is given in tables 1 and 2 for $K = 16$ and $\sigma_R^2 = 0.1$ and 0.5, respectively. In fig. 4 the standard deviation $\sqrt{\mathrm{var}(\hat{S}_j)}$ is plotted as a function of the number of terms K in the truncated Fourier series for $\sigma_R^2 = 0.5$.

3.2. Error due to truncation of the Fourier series

In order to estimate the order of magnitude of the error in $\hat{S}_j$ due to the truncation of its Fourier series $\hat{s}_k$ it is assumed that $s(y) \to 0$ for $|y| \to \infty$ and that the deleted part of $\hat{s}_k$ approaches zero exponentially. This is more or less an intermediate situation, since for instance a Gaussian decays faster and a Lorentzian decays more slowly than an exponential. These assumptions enable us to obtain an explicit expression for the inverse Four-

Table 2
Correlation matrix $\mathrm{cor}(\hat{S}_j, \hat{S}_k)$ of $\hat{S}_j$, as in table 1, however $\sigma_R = \sqrt{0.5}$

j: 0	1	2	3	4	5	6	7	8	k
1	−0.18	0.07	−0.03	0.02	−0.01	0.01	−0.01	0.01	0
	1	−0.18	0.07	−0.03	0.02	−0.01	0.01	−0.01	1
		1	−0.18	0.07	−0.03	0.02	−0.01	0.01	2
			1	−0.18	0.07	−0.03	0.02	−0.01	3
				1	−0.18	0.07	−0.03	0.02	4
					1	−0.18	0.07	−0.03	5
						1	−0.18	0.07	6
							1	−0.18	7
								1	8

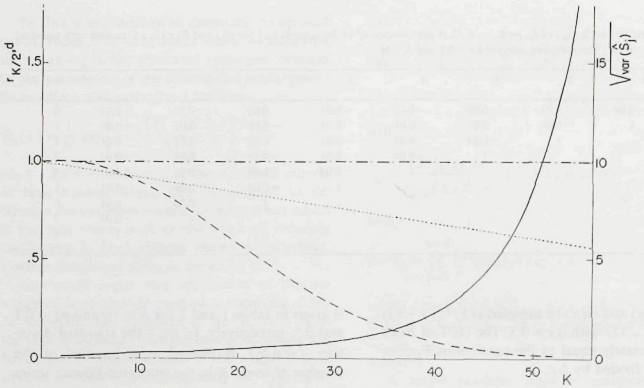

Fig. 4. Standard deviation $\sqrt{\text{var}(\hat{S}_j)}$ (solid line) of the random error in $\hat{S}_j$, $j=0,\ldots,K-1$, given as function of the number of terms K in the truncated Fourier series. The resolution function $R(x)$ is Gaussian with standard deviation $\sigma_R=\sqrt{0.5}$, sampling interval $\Delta x=0.3$, the number of samples $N=128$ and the standard deviation of the random error in M_l, $l=0,\ldots,N-1$ is $\sigma_l=1$. The value of the Fourier transform of the resolution function at the cut-off, $r_{K/2}$, is indicated by the dashed line. The relative error d in $\hat{S}_j$ due to truncation of the Fourier series if $S_j=\delta_{j0}$ is indicated by the dotted line and its estimate by means of (17) by the dash-dotted line.

ier transform of the deleted part of $\hat{s}_k$. The inverse DFT is approximated by the integral transform:

$$\frac{1}{2\pi}\int_{-\infty}^{\infty} e^{-iyx}s(y)\,dy \approx \frac{1}{N}\sum_{k=0}^{N-1} e^{-ijk2\pi/N}\hat{s}_k$$

with $s(y)$ some function of y that is equal to $\hat{s}_k\,\Delta x$ at $y_k=k\,\Delta y$ ($\Delta x=2\pi/N\,\Delta y$). Deletion of all Fourier components $\hat{s}_k$ with $K/2+1\leqslant k\leqslant N-K/2$ implies subtracting from the inverse DFT approximately:

$$D(x)=\frac{1}{2\pi}\left\{\int_{-\infty}^{-Y} e^{-iyx}s(y)\,dy + \int_{Y}^{\infty} e^{-iyx}s(y)\,dy\right\} \qquad (15)$$

with $Y=K\,\Delta y/2$.

If $s(y)=A\,\exp(-b|y|)$, (15) becomes

$$D(x)=\frac{A\,e^{-Yb}}{\pi}\,\frac{b\cos(Yx)-x\sin(Yx)}{x^2+b^2}. \qquad (16)$$

$D(x)$ vanishes for tg $Yx=b/x$, which has non-equidistant solutions for x, that approach multiples of $\pi/Y=N\,\Delta x/K$ for $x\to\infty$. Note that the deconvoluted spectrum $S(x)$ is estimated by $\hat{S}_j$ at $x_j=jN\,\Delta x/K$. At the latter values of x (16) becomes:

$$D_j=\frac{A}{\pi}\,e^{-Yb}\frac{(-1)^j b}{x^2+b^2}=\frac{(-1)^j\hat{s}_{K/2}\hat{S}_j}{\hat{s}_0}$$

and the relative error in $\hat{S}_j$ is estimated by:

$$\frac{|D_j|}{\hat{S}_j}=\frac{|\hat{s}_{K/2}|}{\hat{s}_0} \qquad (17)$$

which does not depend on j.

One may consider to correct $\hat{S}_j$ by adding D_j, but $\hat{s}_{K/2}$ has a large random error $z_{K/2}/r_{K/2}$, which might be of the same order of magnitude as $\hat{s}_{K/2}$, and in addition the true Fourier series s_k will in general not be exponential for $k>K/2$. This leads to a large uncertainty in D_j and therefore it was decided to add D_j^2 to the variance of the random error calculated in section 3.1, to obtain an estimate of the square of the total error in $\hat{S}_j$.

It may seem worthwhile to evaluate (15) for a Gaussian or for a Lorentzian behaviour of $\hat{s}_k$ but this does not lead to simple explicit expressions like (17).

Some examples

The error bars indicated in figs. 1–3 are equal to $2|D_j|$ calculated, using (17). In the case of a Lorentzian $S(x)$ (fig. 2), whose Fourier transform is exactly exponential, $|D_j|$ is only approximately equal to the difference between the inverse DFT of the truncated Fourier series and the original $S(x)$ due to the remaining approximations made in deriving (17). As to be expected, the errors are overestimated in the case of a Gaussian $S(x)$ (fig. 1) and underestimated in the case of an exponential $S(x)$ (fig. 3).

Another simple but illustrative example is obtained with $S_j=\delta_{j0}$. The DFT is $s_k=1$ for all k. Truncating to K terms and applying the inverse DFT yields.

$$\hat{S}_j=\frac{K}{N}\delta_{j0}.$$

Note that in this particular example the estimate $\hat{S}_j$ is exact for all $j\neq 0$ (apart from random errors), which illustrates again the advantage of increasing the sampling interval from Δx to $N\,\Delta x/K$. The true relative error is $(1-K/N)$ and is indicated in fig. 4 as function of K. Eq. (17) yields an estimate of the relative error in $\hat{S}_j$ equal to 1 for all K, also indicated in fig. 4.

The latter example represents the worst possible case with respect to truncation of the Fourier series since s_k does not approach zero; any other function $S(x)$ will result in a smaller and better estimated truncation error in $\hat{S}_j$.

3.3. Conclusions

In section 3.1 *exact* expressions are derived for the variance–covariance matrix $\text{var}(\hat{S}_j,\hat{S}_k)$. Its numerical computation is relatively easy because a few simplifications reducing the number of Fourier transforms needed were possible. The estimate $\hat{S}_j$ of $S(x)$ is calculated in a reduced number of points and use can be made of Fast Fourier Transforms.

In section 3.2 an expression is derived to estimate the error in $\hat{S}_j$ due to truncation of the Fourier series. In other words: we take into account that our regression model for $M(x)$ (a finite Fourier series) is not the true one which is usually unknown, and that our estimate $\hat{S}_j$ is biased [16]. This error will decrease with increasing K in contrast to $\text{var}(\hat{S}_j)$ and the optimum value of K is such that the truncation error is of the same order of magnitude as the standard deviation of the random error (fig. 4).

4. Numerical tests

In spite of the large number of publications on deconvolution methods one hardly finds reproducible numerical tests in the literature, to make a fair comparison of the different algorithms possible. The present method is applied to five tests taken from refs. [17–20] and to three additional variants of some of these.

In each case a known function $S(x)$ is folded with a resolution function $R(x)$, pseudo-random noise on the resulting M_j is simulated, the deconvolution algorithm is applied assuming $R(x)$ exactly known, and $\hat{S}_j$ is compared with the original S_j and, if possible, with the $\hat{S}_j$ given in the paper from which the test is taken. As mentioned in the introduction full automatism was one of the requirements and the tests were used to investigate whether one single cut-off criterion for the Fourier series existed, to be used under different conditions regarding shape of $S(x)$ and $R(x)$ and statistical errors. At least for the seven tests below this proved indeed to be the case: the Fourier coefficients could be regarded insignificant as soon as F, defined by eq. (C.9), dropped below 6. This is confirmed by a comparison of the mean squared deviation with the mean of the variances of the random error in M_j. The ratio is given by

$$t=\frac{T^2}{N-K}\Big/\frac{1}{N}\sum_{j=0}^{N-1}\sigma_j^2 \qquad (18)$$

Table 3
Summary of results from the tests (numbers refer to the text). N is the number of samples, K is the number of terms in the truncated Fourier series, F is defined in eq. (C.9), and t, the ratio of the mean squared deviation and the mean variance, is used to check whether K is large enough. $\overline{\Delta_o}$, $\overline{|\Delta_o|}$ and f_o compare the actual deviation with the standard deviation of $\hat{S}$, whereas $\overline{\Delta_e}$, $\overline{|\Delta_e|}$ and f_e compare the actual deviation with the estimated total error of $\hat{S}$

Test	N	K	F eq. (B.9)	t eq. (18)	$\overline{\Delta_o}$ eq. (22)	$\overline{\lvert\Delta_o\rvert}$ eq. (23)	f_o	$\overline{\Delta_e}$ eq. (20)	$\overline{\lvert\Delta_e\rvert}$ eq. (21)	f_e
1	44	8	41	0.80	−0.08	0.99	0.50	−0.08	0.99	0.50
2	150	10	6.3	1.21	+0.02	0.69	0.70	−0.01	0.54	0.90
3	150	8	53	1.20	−0.12	0.65	0.88	−0.12	0.56	0.88
4	1024	14	218	0.95	+0.02	0.86	0.57	0.00	0.77	0.71
5	1024	24	59	0.94	+0.01	1.18	0.54	0.00	0.64	0.79
6	512	24	7.6	1.19	−5.5	3.1	0.46	−5.5 +0.12	13.1 1.4	0.46 0.60 [a]
7	512	20	3424	1.08	−0.01	2.7	0.00	−0.15	2.4	0.1

[a] After deleting the outer 5 points $\hat{S}_j$.

with T^2 defined by (C.6). As should be expected, t turned out to be close to 1 for all tests.

Another aim was to test the reliability of the estimated confidence limits. The actual deviation Δ_j of $\hat{S}_j$ from S_j is compared with the standard deviation of $\hat{S}_j$ and with the estimated total error

$$e_j = \left\{\mathrm{var}\left(\hat{S}_j\right) + D_j^2\right\}^{1/2}, \tag{19}$$

where $\mathrm{var}(\hat{S}_j)$ is given by (8) ($j=m$) and D_j by (17). For a standard normal distribution the average of the variable is zero, the average of its absolute value is 0.80 and 68% is smaller than 1.

In each test the following three quantities to judge the error estimates are used

$$\overline{\Delta_e} = \frac{1}{K}\sum_{j=0}^{K-1} \Delta_j/e_j, \tag{20}$$

$$\overline{|\Delta_e|} = \frac{1}{K}\sum_{j=0}^{K-1} |\Delta_j/e_j| \tag{21}$$

and the fraction f_e of $|\Delta_j/e_j|<1$. Also, the estimated standard deviation of $\hat{S}_j$ is compared with the actual deviation by means of

$$\overline{\Delta_o} = \frac{1}{K}\sum_{j=0}^{K-1} \Delta_j/\sqrt{\mathrm{var}\left(\hat{S}_j\right)}, \tag{22}$$

$$\overline{|\Delta_o|} = \frac{1}{K}\sum_{j=0}^{K-1} |\Delta_j/\sqrt{\mathrm{var}\left(\hat{S}_j\right)}| \tag{23}$$

and the fraction f_o of $|\Delta_j/\sqrt{\mathrm{var}(\hat{S}_j)}|<1$. Thus the effect of the estimation of the truncation error on the reliability of the estimation of the total error is investigated.

In each of the tests F, t, $\overline{\Delta}_o$, $\overline{|\Delta_o|}$, $\overline{\Delta_e}$, $\overline{|\Delta_e|}$, f_e and f_o [eqs. (C.9), (18), (20)–(23)] are calculated and given in table 3.

4.1. Test # 1

Johnson [17] presents a method to solve eq. (1) where the resolution function does not need to be translation invariant. His method is based on substitution of the Taylor series expansion of $S(x)$ in (1) and he obtains a solution $\hat{S}(x)$ in terms of derivatives of $M(x)$ and moments of $R(x,x')$ by repeated differentiation of (1) and elimination of the derivatives of $S(x)$.

Johnson tests his method with a Gaussian $S(x)$ and a Gaussian and translation invariant resolution function:

$$S(x) = \frac{1}{\sigma_S\sqrt{2\pi}}\exp\left(-\frac{x^2}{2\sigma_S^2}\right),$$

$$R(x) = \frac{1}{\sigma_R\sqrt{2_p}}\exp\left(-\frac{x^2}{2\sigma_R^2}\right).$$

So $M(x)$ is also Gaussian with standard deviation $\sigma_M = \sqrt{\sigma_S^2 + S_R^2}$. He shows for this special case

Table 4
Results for test # 1 and comparison with Johnson's method [17]

j	x_j	M_j	S_j	$\hat{S}_j$ ref. [17]	Δ_j	$\hat{S}_j$ this work	Δ_j
0	−4.2	0.001	0.000			0.004	0.004
1	−4.0	0.002	0.000			0.008	0.008
2	−3.8	0.003	0.000			0.008	0.008
3	−3.6	0.004	0.001	−0.001	−0.002	0.007	0.006
4	−3.4	0.007	0.001	−0.001	−0.002	0.005	0.004
5	−3.2	0.010	0.002	−0.001	−0.003	0.003	0.001
6	−3.0	0.016	0.004	0.003	−0.001	0.003	−0.001
7	−2.8	0.023	0.008	0.006	−0.002	0.005	−0.003
8	−2.6	0.034	0.014	0.014	0.000	0.010	−0.004
9	−2.4	0.046	0.022	0.028	0.006	0.020	−0.002
10	−2.2	0.066	0.035	0.040	0.005	0.035	0.000
11	−2.0	0.085	0.054	0.064	0.010	0.056	0.002
12	−1.8	0.107	0.079	0.086	0.007	0.083	0.004
13	−1.6	0.140	0.111	0.119	0.008	0.115	0.004
14	−1.4	0.166	0.150	0.160	0.010	0.152	0.002
15	−1.2	0.206	0.194	0.209	0.015	0.193	−0.001
16	−1.0	0.236	0.242	0.260	0.018	0.238	−0.004
17	−0.8	0.269	0.290	0.296	0.006	0.284	−0.006
18	−0.6	0.293	0.333	0.328	−0.005	0.326	−0.007
19	−0.4	0.303	0.368	0.343	−0.025	0.362	−0.006
20	−0.2	0.326	0.391	0.366	−0.025	0.387	−0.004
21	0	0.321	0.399	0.369	−0.030	0.398	−0.001
22	0.2	0.328	0.391	0.380	−0.011	0.390	−0.001
23	0.4	0.305	0.368	0.355	−0.013	0.357	−0.001
24	0.6	0.295	0.333	0.333	0.000	0.333	0.000
25	0.8	0.259	0.290	0.280	−0.010	0.291	0.001
26	1.0	0.229	0.242	0.238	−0.004	0.246	0.004
27	1.2	0.196	0.194	0.190	−0.004	0.200	0.006
28	1.4	0.167	0.150	0.161	0.011	0.157	0.007
29	1.6	0.140	0.111	0.125	0.014	0.118	0.007
30	1.8	0.108	0.079	0.093	0.014	0.083	0.004
31	2.0	0.084	0.054	0.063	0.009	0.054	0.000
32	2.2	0.065	0.035	0.041	0.006	0.031	−0.004
33	2.4	0.048	0.022	0.029	0.007	0.016	−0.006
34	2.6	0.034	0.014	0.017	0.003	0.006	−0.008
35	2.8	0.024	0.008	0.008	0.000	0.002	−0.006
36	3.0	0.016	0.004	0.002	−0.002	0.001	−0.003
37	3.2	0.011	0.002	0.000	−0.002	0.003	0.001
38	3.4	0.007	0.001	−0.001	−0.002	0.006	0.005
39	3.6	0.004	0.001	−0.001	−0.002	0.009	0.008
40	3.8	0.003	0.000			0.011	0.011
41	4.0	0.002	0.000			0.011	0.011
42	4.2	0.001	0.000			0.006	0.006
43	4.4	0.000	0.000			−0.003	−0.003

that, even if $\sigma_R/\sigma_M = 0.5$, only two terms in the Taylor series expansion of $S(x)$ are sufficient to obtain an accuracy of 2% in $\hat{S}(x)$ (apart from experimental errors) and so only $M(x)$, its second derivative and the zeroth and second moment of $R(x)$ are needed.

In ref. [17] $\sigma_S = 0.1$, $\sigma_R = 0.7$ and $M(x)$ is sampled at 43 points with $\Delta x = 0.2$, while normally

distributed pseudo-random noise with a standard deviation of 2% is added to M_j. Johnson gives a table of M_j, $j = 3,\ldots,39$ and to test the present method these were copied from ref. [17] and supplemented with simulated extra data for $j = 0$, 1, 2, 40, 41, 42, 43. The results are summarised in table 3: the least squares fit to M_j with only 8 Fourier coefficients is satisfactory, since $t = 0.80$, and the error estimates seem quite reliable. Note that in this case the truncation errors appears to be small compared to the statistical errors, which is not the case in the following tests. The sampling interval is increased from 0.2 to 1.1 and in order to compare the present results with those given in ref. [17] a cubic spline, which is continuous and has continuous first and second derivatives, was used to interpolate $\hat{S}_j$ to the original x_j. Table 4 gives the results together with the true S_j and the best $\hat{S}_j$ from ref. [17]. Johnson uses the overall error, defined by

$$\left\{\frac{1}{N}\sum_{j=0}^{N-1}\Delta_j^2\right\}^{1/2}\frac{1}{S_{\max}} \tag{24}$$

(private communication) to indicate the quality of the $\hat{S}_j$. He obtains 2.7% whereas the present method yields 1.3% for $j = 0,\ldots,43$ or 1.1% for $j = 3,\ldots,39$. The peak underestimation in ref. [17] is 7.5% and only 0.3% in the present method. The latter error would certainly be greater if the formally more correct weighted least squares technique were used for calculating the Fourier series, since in this test the statistical error is proportional to M_j and consequently the points around the peak would have a relatively small weight.

4.2. Tests # 2 and # 3

Hossfeld et al. [18] present a method using Bayesian techniques and fit a spline folded with the known resolution function to the data M_j. They determine the number of knots for the spline by visual inspection of the data and by trial. Their method is not restricted to translation invariant resolution functions and gives estimated confidence limits of $\hat{S}_j$. From ref. [18] the following two tests are taken.

S and R are again Gaussian with $\sigma_S = 0.25$ and

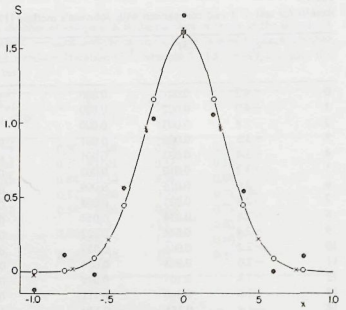

Fig. 5. Results of test # 2 and # 3. The true $S(x)$ is given by the solid line, the estimates $\hat{S}_j$ are given by open circles for $\sigma_R = 0.1$ (test # 2) and by crosses for $\sigma_R = 0.2$ (test # 3). In both tests the standard deviation of the normally distributed pseudo-random noise is 1% of M_j. Estimated error bars ($2e_j$) smaller than the symbols for $\hat{S}_j$ are deleted. Solid circles represent results for $\hat{S}_j$ in test # 3 ($\sigma_R = 0.2$) if the number of Fourier coefficients is increased with 2.

$\sigma_R = 0.1$ (test # 2) and 0.2 (test # 3). The pseudo-random noise in M_j is distributed normally with a standard deviation of 1%. In ref. [18] the x_j, $j = 0,\ldots,149$ are randomly distributed on $[-1, 1]$. As the present method requires equidistant x_j, the data were simulated with $\Delta x = 1/75$, $N = 150$ and $x_0 = -1$.

The results are given in table 3 and fig. 5. The value of t (resp. 1.21 and 1.20) indicates that 10 resp. 8 Fourier coefficients are sufficient to describe $M(x)$ within the given experimental error. Fig. 5 indicates that $S(x)$ is very well approximated by $\hat{S}_j$ albeit in much less points than the original 150. If the number of Fourier coefficients would be increased, in order to obtain more estimates $\hat{S}_j$ at a closer spacing the same would happen as in ref. [18] for $\sigma_R = 0.2$ where the number of knots for the spline was probably too large: $\hat{S}_j$ would oscillate and the errors would increase. In fig. 5 is demonstrated what happens if in the latter case K is increased from 8 to 10.

The results in table 3 indicate that the systematic error is not negligible, in contrast to test # 1, but on the other hand the present method of estimating this error leads to an overestimation of the total error by a factor 2 on the average.

4.3. Test # 4 and # 5

Hunt [8] uses the discrete Fourier transform to solve (3) with a low-pass filter that minimises the second differences of $\hat{S}_j$ with the boundary condition

$$\sum_{j=0}^{N-1}\left(M_j - \hat{M}_j\right)^2 = \sum_{j=0}^{N-1}\sigma_j^2,$$

where

$$\hat{M}_j = \sum_k R_{j-k}\hat{S}_k.$$

The filter is found iteratively.

In test # 4, taken from ref. [8], $S(x)$ is a sum of two Gaussians:

$$S(x) = \exp\left[-\left\{\frac{x+100}{75}\right\}^2\right] + \exp\left[-\left\{\frac{x-100}{75}\right\}^2\right]$$

and the resolution function is rectangular:

$$R(x) = 1 \quad -125 < x < 125,$$
$$= 0 \quad x \leqslant -125,\ x \geqslant 125.$$

$M(x)$ is sampled at 1024 points with $\Delta x = 1$, $-512 \leqslant x < 512$. M_j contains pseudo-random noise uniformly distributed on $(-5, 5)$, so $\sigma_j^2 = 25/3$ for all j and σ_j is about 1.6% of the peak value of $M(x)$.

In this test F, defined in (C.9), follows the F-distribution. The continuous Fourier transforms $s(y)$ and $m(y)$ are given in fig. 6, together with $m'_k = \mathrm{Re}(m_k)$ and $\hat{s}'_k = \mathrm{Re}(m_k/r_k)$. Note that $\hat{s}_k$ starts to deviate appreciably from $s(y)$ for $k > 7$, which suggests that $K \leqslant 14$. All these functions and series oscillate around zero and from (C.7) and (C.9) it may be concluded that F could drop below 6 before a satisfactory fit to M_j is obtained, but this turns out not to be the case as can be seen

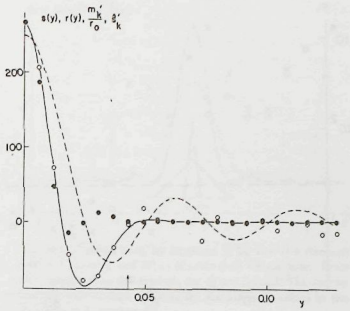

Fig. 6. Continuous Fourier transforms $s(y)$ (solid line) and $r(y)$ (dashed line) of $S(x)$, resp. $R(x)$, and the real part of the DFT $m'_k = \mathrm{Re}(m_k)$ (solid circles) of M_j for test # 4. $R(x)$ is not normalised to 1 and m_k is divided by r_0 to the same normalisation as $s(y)$ and $r(y)$. $\hat{s}'_k = \mathrm{Re}(m_k/r_k)$ is given by open circles. The arrow indicates where the Fourier series m_k and $\hat{s}_k$ are cut off (see appendix B).

in fig. 7 where F is plotted as a function of the number K of independent Fourier coefficients; the fact that $t = 0.95$ (table 3) indicates that for $K = 14$ the fit is good.

As test # 5 the simulated errors in M_j were decreased by a factor of 100, while all other parameters remained unchanged. Again F is given in fig. 7 from which the optimum value of K is determined as 24, which is confirmed by $t = 0.94$. In both tests the very distinct drop of F at that value of K, where a satisfactory fit to M_j is obtained, is rather striking and makes one confident about the general applicability of this method of determining the number of significant Fourier coefficients.

The resulting $\hat{S}_j$ are given in fig. 8 for both tests and compared with the true $S(x)$. Also $M(x)$ and $R(x)$ are given. In ref. [8] Hunt gives a table where his results $\hat{S}$ are compared with $S(x)$ for $x = -450(50)500$. In table 5 these data are given together with the results of the present method obtained as in test # 1 by means of cubic spline interpolation of $\hat{S}_j$. The spline is also given in

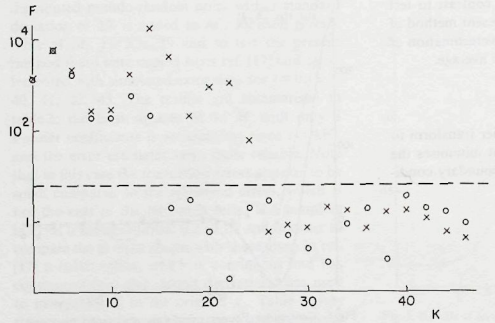

Fig. 7. Value of F, eq. (C.9), as function of K for test # 4 (circles) and # 5 (crosses). Horizontal line indicates $F=6$.

Table 5
Results for test # 4 and comparison with Hunt's method [8]

j	S_j	$\hat{S}_j$	Δ_j	$\hat{S}_j$	Δ_j
		ref. [8]		this work	
50	0.000	0.010	0.010	0.021	0.021
100	0.000	−0.022	−0.022	−0.028	−0.028
150	0.000	−0.017	−0.017	−0.023	−0.023
200	0.001	−0.006	−0.005	0.028	0.027
250	0.018	0.023	0.005	0.009	−0.009
300	0.169	0.210	0.041	0.198	0.029
350	0.641	0.612	−0.029	0.652	0.011
400	1.001	0.966	−0.035	0.927	−0.074
450	0.660	0.659	−0.001	0.689	0.029
500	0.338	0.362	0.024	0.352	0.014
550	0.660	0.688	0.028	0.701	0.041
600	1.001	0.983	−0.018	0.935	−0.066
650	0.641	0.630	−0.011	0.645	0.004
700	0.169	0.153	−0.016	0.187	0.018
750	0.018	0.029	0.011	0.006	−0.012
800	0.001	0.029	0.028	0.037	0.036
850	0.000	−0.010	−0.010	−0.013	−0.013
900	0.000	−0.025	−0.025	−0.029	−0.029
950	0.000	−0.017	−0.017	0.010	0.010
1000	0.000	−0.010	−0.010	0.018	0.018

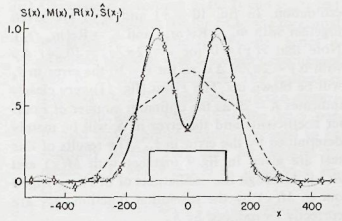

Fig. 8. Results of test # 4 and # 5. The true $S(x)$ is given by the solid line, the estimates $\hat{S}_j$ are given by circles for $\sigma_j^2 = 25/3$ (test # 4) and by crosses for $\sigma_j^2 = 25\times10^{-4}/3$ (test # 5). Estimated error bars ($2e_j$) smaller than the symbols are deleted. $M(x)$ (without noise) is indicated by the dashed line, the spline interpolation for test # 4 by the dotted line and the rectangle is the resolution function.

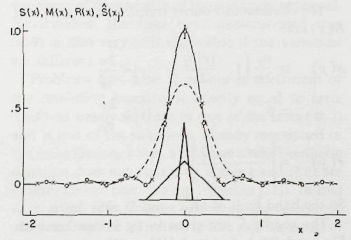

Fig. 9. $S(x)$ (solid line), its estimates $\hat{S}_j$ for test # 6 (crosses) and # 7 (circles), and $M(x)$ (dashed line) for the latter. Error bars smaller than the symbols for $\hat{S}_j$ are deleted. The narrow and the wide triangle indicate the resolution functions in test # 6 and # 7, respectively.

fig. 8. The overall error as defined by (24) and calculated for the data in table 5 is 2.1% for Hunt's method and 3.1% for the present one.

From table 3 it is concluded that in test # 4 and # 5 the error estimates improve by taking into account the estimates of the truncation errors.

4.4. Tests # 6 and # 7

Beniaminy and Deutsch [19] present an incorrect method to solve eq. (3) which may lead to erroneous solutions $\hat{S}$, as demonstrated by Fredrikze and Verkerk [20]. But their numerical test is interesting, since the $S(x)$ they use for the simulation, is band limited (consequently $M(x)$ too), whereas in the present method it is implicitly assumed that $S(x)$ is not band limited.

In ref. [19]

$$S(x) = \left[\frac{\sin \pi x/\sigma_S}{\pi x/\sigma_S}\right]^2$$

$$R(x) = \frac{1}{\sigma_R}\left(1-\frac{|x|}{\sigma_R}\right) \quad |x|<\sigma_R$$
$$= 0 \quad |x|>\sigma_R$$

with $\sigma_S = 0.5$ and $\sigma_R = 0.1$. $M(x)$ is sampled at 250 points $x_j = (j-1)\,\Delta x$ with $\Delta x = 0.01$. Uniformly distributed pseudo-random noise with 1% maximum amplitude ($\sigma_j^2 = 0.0001 M_j^2/3$) is added to M_j and then the M_j are extended to 499 points by symmetrising with respect to $x=0$. This means that the M_j are pairwise correlated which is in disagreement with the assumptions in the present method. As test # 6 $S(x)$ and $R(x)$, and simulated noise with the same parameters as given above are used with $M(x)$ sampled at 512 points $x_j = j\,\Delta x - 2.56$, $\Delta x = 0.01$, so all M_j are uncorrelated.

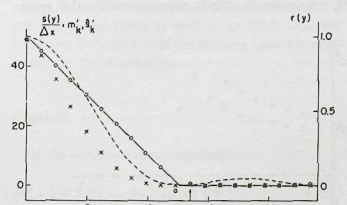

Fig. 10. Continuous Fourier transforms $s(y)$ divided by Δx (solid line) and $r(y)$ (dashed line) of $S(x)$ resp. $R(x)$ in test # 7. The real part of the DFT $m_k' = \mathrm{Re}(m_k)$ of M_j is indicated by crosses and $s_k' = \mathrm{Re}(m_k/\Delta x r_k)$ by circles. The arrow indicates where the Fourier series m_k and s_k are cut off.

The continuous Fourier transforms of $S(x)$ and $R(x)$ are:

$$s(y) = \frac{\sigma_S}{2\pi}\left(1-\frac{|y|\sigma_S}{2\pi}\right) \quad |y|<\frac{2\pi}{\sigma_S}$$
$$= 0 \quad |y|>\frac{2\pi}{\sigma_S}$$

$$r(y) = \left[\frac{\sin x\sigma_R/2}{x\sigma_R/2}\right]^2$$

So the band limit of $M(x)$ and $S(x)$ is $2\pi/\sigma_S$.

The results $\hat{S}_j$ are given in fig. 9 together with $S(x)$ and $R(x)$. As in ref. [19] excellent results are obtained, however, it is clear from table 3 that the error estimates are not as good as in the previous tests. The estimates of the truncation error are negligible as compared to the standard deviations of the random errors since the Fourier series is cut off beyond the band limit. If the five $\hat{S}_j$'s with largest $|x|$ are left out of consideration, the averages of the error estimates improve considerably, so the underestimation of the errors is worst where they are relatively small.

As the resolution function in this case is rather narrow and has little effect on $S(x)$, test # 7 used the above $S(x)$ and $R(x)$, however with σ_R equal to $\sigma_S = 0.5$. In ref. [20] it is demonstrated that even without simulated noise the method by Beniaminy and Deutsch yields a wrong solution $\hat{S}$. In the present test uniformly distributed noise of maximum amplitude 10^{-4} ($\sigma_j^2 = 10^{-8}/3$) was added to M_j in order to check simultaneously the error

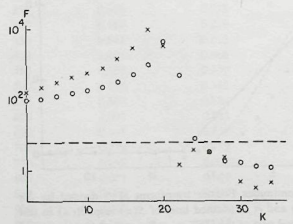

Fig. 11. Value of F as function of K for test # 6 (circles) and # 7 (crosses). Horizontal line indicates $F=6$.

estimation. In fig. 10 $s(y)$ and $r(y)$ are given together with $m'_k = \mathrm{Re}(m_k)$ and $\hat{s}'_k = \mathrm{Re}(m_k/r_k)$. Note that $r(y)=0$ for $y = j2\pi/\sigma_R = 10.24j\ \Delta y$ with $\Delta y = 2\pi/N\ \Delta x$, so for $k=10$ the error in $\hat{s}_k$ will be blown up. The F-test (fig. 11) very clearly indicates $K=20$ as the optimum number of Fourier coefficients and the error in $\hat{S}_j$ will be mainly determined by the error in $\hat{s}_{10}$. The results of this test are given in fig. 9 together with $M(x)$ and $R(x)$. Although the oscillations of $S(x)$ are wiped out in $M(x)$ by the resolution function they are correctly reproduced by $\hat{S}_j$.

From table 3 it can be seen, that $K=20$ yields a satisfactory fit. The errors are underestimated but not as badly as in the previous test.

In test # 6 the σ_j^2 are different for different j and consequently F does not follow the F-distribution, in contrast to test # 7 where all σ_j^2 are equal. However, the general behaviour of F as function of K is the same for both cases with a sharp decrease at the optimum value of K, as in the previous tests. This demonstrates the general applicability of F defined by (C.9).

5. Discussion

An algorithm is described to solve the Fredholm integral equation of the first kind with the kernel restricted to be translation invariant: $f(x) = \int K(x-y)\, g(y)\, \mathrm{d}y$. It has been tested under various conditions regarding statistics and form of function g and kernel K. The estimated solution was satisfactory in all tests, and except for some individual points the error was estimated correctly within a factor 3.

Because the algorithm is simple and every computer program library contains its own different variants of routines for calculating fast Fourier transforms, it seems unnecessary to include the computer program in the CPC library.

The resulting algorithm is summarised as follows:

(i) Apply the fast Fourier transform to the measured spectrum, the resolution function (also measured or known in some other way) and the variances. For convenience series should be arranged according to appendix B.

(ii) Calculate F according to (C.7) and (C.9) and the sum of squares for the fit to the measured spectrum (C.5), while the Fourier series is extended stepwise with a complex conjugated pair of Fourier coefficients. The process is stopped when F drops below some empirically determined value. For the tests performed in the present paper 6 proved to be generally useful. This may be checked by means of t, which should be close to 1, eq. (18).

(iii) Calculate the estimated Fourier coefficients of the deconvolved spectrum (5a) and its variance–covariance matrix (D.4). Apply the fast Fourier transform to calculate the deconvolved spectrum and its variance–covariance matrix (D.7) and (D.6), or if the error in the resolution function is negligible (8) and (9). Estimate the truncation error by means of (17). The total error may be estimated by taking the square root of the sum of the variance and the squared truncation error.

This algorithm lacks a firm statistical basis, since formally incorrectly it uses the unweighted least squared regression, but in practice it gives very useful results at high speed. For instance the processing of the 1024 high accuracy data in test 5 takes only about 3 s (including complete error analysis) on an IBM 370/158. A large reduction of computer time is obtained because two-dimensional Fourier transform of the variance–covariance matrix of the Fourier coefficients of the corrected spectrum needs only to be done after truncation. It turns out in the tests that even for high accuracy measurements the number of independent relevant Fourier coefficients does not exceed 24. This means that the two-dimensional Fourier transform must be calculated only for (24×24) matrices instead of the full $(N\times N)$ ones where N is the number of samples.

The quantity F defined by eq. (C.9) is used to determine the necessary and sufficient number of Fourier coefficients of the measured, resolution broadened spectrum, which is a crucial step in the algorithm. Definition (C.9) is equal to the usual F-test in regression analysis, but the present F follows the F-distribution only in the case that all variances of the samples of the spectrum are equal. Nevertheless, the tests have demonstrated that (C.9) is also very well applicable if the variances are different.

Problems may arise if a Fourier coefficient of the resolution function is exactly equal to zero. This was nearly the case in one of the tests (# 7) and is one of the situations, already mentioned in the introduction, where a solution of the Fredholm equation does not exist even if $K(x)$ and $f(x)$ are exactly known (see also e.g. Seidman [21]). In that case either the Fourier series of the measured spectrum will be truncated before this happens, or one or several Fourier coefficients of the deconvolved spectrum will be indeterminate, contain very large errors, and cause oscillations in the estimated deconvolved spectrum.

Estimation of the errors due to truncating the Fourier series does not always improve the estimates of the total error, but may be useful mainly around peaks, which are liable to underestimation because of deletion of higher order Fourier coefficients.

It is believed that the present method is a valuable supplement to the many already in use, especially when speed of computation or adequate error estimates are needed.

Acknowledgements

The many useful discussions with H. Fredrikze and A.A. van Well are gratefully acknowledged. I am obliged to them as well as to Profs. J.J. van Loef and L.A. de Graaf for making valuable comments on the manuscript.

Appendix A

If the continuous convolution

$$M(x_j) = \int R(x_j - y)\, S_0(y)\, \mathrm{d}y \qquad (A.1)$$

is approximated by a discrete one

$$M(x_j) = \sum_k R(x_j - x_k)\, S(x_k)\, \Delta x, \qquad (A.2)$$

our aim is to find a relation between S_0 and S. In fact $S(x_k)$ is defined through eq. (A.2). Discrete Fourier Transform of (A.2) yields:

$$s_k = m_k / r_k \Delta x = \sum_j e^{ijk2\pi/N} M(x_j)/r_k \Delta x. \quad (A.3)$$

Substitution of (A.1) in (A.3) gives:

$$s_k = \int dx S_0(x) \sum_j e^{ijk2\pi/N} R(x_j - x)/r_k \Delta x. \quad (A.4)$$

Now

$$\sum_j e^{ijk2\pi/N} R(x_j - x) = r'_k e^{ikx2\pi/N\Delta x}, \quad (A.5)$$

where r'_k is the DFT of $R(x)$, with the latter sampled at a set x'_j shifted over x with respect to the original set x_j. Clearly, $r'_k \approx r_k$ to a good approximation and

$$S(x_j) \approx \frac{1}{N} \sum_k e^{-ijk2\pi/N} \frac{1}{\Delta x} \int dx S_0(x)\, e^{ixk2\pi/N\Delta x},$$

or

$$S(x_j) \approx \frac{1}{\Delta x} \int_{x_j - \frac{1}{2}\Delta x}^{x_j + \frac{1}{2}\Delta x} S_0(x)\, dx. \quad (A.6)$$

Appendix B

If Fast Fourier Transform techniques are used, it is most convenient to restrict N to even numbers. To avoid the appearance of complex phase factors in the Fourier series one should arrange the samples $F(x_j)$ such, that $x_j = j\ \Delta x$ for $j = 0,\ldots, N/2$ and $x_j = (j-N)\ \Delta x$ for $j = N/2+1,\ldots, N-1$. If $x=0$ does not coincide with one of the x_j, interpolation can be avoided by multiplying the DFT f_k with the complex phase factor

$$\phi_k = \exp\left(ik \frac{x_0}{\Delta x} \frac{2\pi}{N}\right), \quad (B.1)$$

where Δx is the sampling interval and x_0 is the value of x, where the first sampling point of $F(x)$ was chosen.

Now f_k is arranged such, that $y_k = k\ \Delta_y$ for $k = 0,\ldots, N/2$ and $y_k = (k-N)\ \Delta y$ for $k = N/2+1,\ldots, N-1$, with $\Delta y = 2\pi/(N\ \Delta x)$. In general f_k is complex: $f_k = f'_k + i f''_k$. If $F(x)$ is real, f'_k is even or $f'_k = f'_{N-k}$ and f''_k is uneven or $f''_k = -f''_{N-k}$ with $f''_0 = f''_{N/2} = 0$.

If the Fourier series is to be truncated to K terms ($K < N$ and even) and the inverse DFT is still to remain real, terms f_k, $k = 0,\ldots, K/2$ and $k = N-K/2+1,\ldots, N-1$ should be retained and $f''_{K/2}$ should be set to zero. If the series f_k is not truncated but set to zero for $k = K/2+1,\ldots, N-K/2$, it is convenient to replace $f_{K/2}$ by $\frac{1}{2}f_{K/2}$ and $f_{N-K/2}$ by $\frac{1}{2}f_{N-K/2}$, because then the requirements of even f'_k and uneven f''_k are fulfilled and inverse DFT yields the same results at $x_j = jN\ \Delta x/K$ as inverse DFT of the truncated Fourier series.

Appendix C

By means of the least squares method we want to fit the model

$$F(x) = \sum_{k=0}^{K-1} f_k \Psi_k(x) \quad (C.1)$$

with

$$\Psi_k(x) = \frac{1}{N} \exp\left\{-il \frac{x-c}{\Delta x} \frac{2\pi}{N}\right\} \quad (C.2)$$

to the data $M(x_j)$, $j = 0,\ldots, N-1$, with $x_j = j\ \Delta x + c$ and $l = k$ for $k = 0,\ldots, K/2$ and $l = n-K+k$ for $k = K/2+1,\ldots, K-1$. The functions $\Psi_k(x)$ are orthogonal on the set x_j:

$$\sum_{j=0}^{N-1} \Psi_k(x_j)\, \Psi^*_m(x_j) = \frac{\delta_{km}}{N}, \quad (C.3)$$

where $\Psi^*_m(x_j)$ is the complex conjugate of $\Psi_m(x_j)$.

Minimising the sum of squares

$$T^2 = \sum_{j=0}^{N-1} |M_j - F(x_j)|^2$$

yields

$$f_k = \sum_{j=0}^{N-1} M_j \exp(i\, jk2\pi/N) \quad (C.4)$$

for $k = 0,\ldots, K/2,\ N-K/2+1,\ldots, N-1$. The least squares coefficients f_k are equal to the DFT of M_j. With (C.4) the sum of squares is:

$$T^2 = \sum_{j=0}^{N-1} M_j^2 - \frac{1}{N} \sum_{k=0}^{K/2} |f_k|^2 - \frac{1}{N} \sum_{k=N-K/2+1}^{N-1} |f_k|^2. \quad (C.5)$$

Note that since M_j is real for $j = 0,\ldots, N-1$, $f_k = f^*_{N-k+1}$ and Im $f_0 = 0$. To ensure that $F(x)$ has real values at the set of points x_j with the increased sampling distance $N\ \Delta x/K$, Im $f_{K/2}$ is set to zero, or in disagreement with (C.2):

$$\Psi_{k/2}(x) = \frac{1}{N} \cos\left[\frac{K}{N} \frac{(x-c)}{\Delta x} \pi\right].$$

Thus (C.1) contains K independent coefficients and (C.5) reduces to

$$T^2 = \sum_{j=0}^{N-1} M_j^2 - \frac{1}{N}\left(f_0^2 + \mathrm{Re}\, f_{K/2}^2\right) - \frac{2}{N} \sum_{K=1}^{K/2-1} |f_k|^2. \quad (C.6)$$

Stepwise regression is conveniently performed by increasing K in each step from $2m$ to $2(m+1)$, adding two independent regression coefficients and decreasing the sum of squares with

$$T_K^2 - T_{K+2}^2 = \frac{1}{N}\left\{Re\left(f_{K/2}\right)^2 + 2\left(\mathrm{Im}\, f_{K/2}\right)^2 + \left(\mathrm{Re}\, f_{K/2+1}\right)^2\right\}. \quad (C.7)$$

This procedure can be continued until T_K^2 is sufficiently small. If all variances σ_j^2 of M_j are equal to σ^2, then $\chi^2 = T_K^2/\sigma^2$ follows a chi-squared distribution with $N-K$ degrees of freedom and T_K^2 would be small enough if $\chi^2 \approx N-K$. For the general case, with all σ_j^2 different, the criterion could be

$$\frac{T_K^2}{N-K} \lesssim \frac{1}{N} \sum_{j=0}^{N-1} \sigma_j^2. \quad (C.8)$$

The χ^2-test is often supplemented with the F-test. Again, if all σ_j^2 are equal,

$$F = \frac{(T_K^2 - T_{K+2}^2)/2}{T_{K+2}^2/(N-K-2)} \quad (C.9)$$

follows the F-distribution with 2 and $N-K-2$ degrees of freedom. K is increased until F drops below some value corresponding to a preset confidence limit. In the general case, when all σ_j^2 are different, F does not obey an F-distribution, but nevertheless (C.9) could be used with the threshold for F not taken from the F-distribution but from experience. When F is judged to be small enough, (C.8) can be used as a check for the sum of squares T_K^2. More about this is said in section 4 on applications.

Appendix D

If m_k, $k = 0,\ldots, N-1$ is the DFT of M_j, $j = 0,\ldots, N-1$ and if M_j has a random error Z_j with variance σ_j^2 and zero covariances a straightforward application of the law of propagation of errors [15] yields for the variance-covariance matrix of $m_k = m'_k + im''_k$ (m'_k and m''_k both real):

$$\begin{aligned} \mathrm{var}(m'_k, m'_l) &= \sum_j \cos\left(\frac{jk2\pi}{N}\right) \cos\left(\frac{jl2\pi}{N}\right) \sigma_j^2, \\ \mathrm{var}(m'_k, m''_l) &= \sum_j \cos\left(\frac{jk2\pi}{N}\right) \sin\left(\frac{jl2\pi}{N}\right) \sigma_j^2, \\ \mathrm{var}(m''_k, m''_l) &= \sum_j \sin\left(\frac{jk2\pi}{N}\right) \sin\left(\frac{jl2\pi}{N}\right) \sigma_j^2. \end{aligned} \quad (D.1)$$

Making use of

$$\cos a \cos b = \tfrac{1}{2}\,\mathrm{Re}\left[\exp\{\mathrm{i}(a+b)\} + \exp\{\mathrm{i}(a-b)\}\right]$$

the required effort to compute $\mathrm{var}(m'_k, m'_l)$ can be reduced considerably:

$$\mathrm{var}(m'_k, m'_l) = \tfrac{1}{2}\,\mathrm{Re}\left[\sum_j \exp\left\{\mathrm{i}(k_j + l_j)\frac{2\pi}{N}\right\}\sigma_j^2 + \sum_j \exp\left\{\mathrm{i}(k_j - l_j)\frac{2\pi}{N}\right\}\sigma_j^2\right]$$

$$= \tfrac{1}{2}\,\mathrm{Re}\left[(\tilde{\sigma}^2)_{k+l} + (\tilde{\sigma}^2)_{k-l}\right], \qquad \text{(D.2a)}$$

where the DFT of σ_j^2 is defined as:

$$(\tilde{\sigma}^2)_k = \sum_{j=0}^{N-1} \sigma_j^2 \exp(\mathrm{i}\,jk2\pi/N). \qquad \text{(D.3)}$$

In a similar way

$$\mathrm{var}(m'_k, m''_l) = \tfrac{1}{2}\,\mathrm{Im}\left[(\tilde{\sigma}^2)_{k+l} - (\tilde{\sigma}^2)_{k-l}\right] \quad \text{and} \qquad \text{(D.2b)}$$

$$\mathrm{var}(m''_k, m''_l) = \tfrac{1}{2}\,\mathrm{Re}\left[(\tilde{\sigma}^2)_{k-l} - (\tilde{\sigma}^2)_{k+l}\right] \qquad \text{(D.2c)}$$

is obtained. Note that Wild et al. [12] give the same expressions for $\mathrm{var}(m'_k, m'_k)$ and $\mathrm{var}(m''_k, m''_l)$, but these authors neglect all covariances. Since $(\tilde{\sigma}^2)_k$ is periodic in k, $k+l > N-1$ can be replaced by $k+l-N$ and $k-l<0$ by $k-1+\mathrm{N}$.

If $\hat{s}'_k = m_k/(r_k\,\Delta x)$, and if M_j and R_j are both the result of a measurement with random errors, the law of propagation of errors yields:

$$\begin{aligned}\mathrm{var}(\hat{s}'_k, \hat{s}'_l) = {} & \left[r'_k r'_l\,\mathrm{var}(m'_k, m'_l) + r''_k r''_l\,\mathrm{var}(m''_k, m''_l) + r'_k r''_l\,\mathrm{var}(m'_k, m''_l) + r''_k r'_l\,\mathrm{var}(m''_k, m'_l)\right.\\ & + (m'_k - 2\,\Delta x r'_k \hat{s}'_k)(m'_l - 2\,\Delta x r'_l \hat{s}'_l)\,\mathrm{var}(r'_k, r'_l) + (m''_k - 2\,\Delta x r''_k \hat{s}'_k)\\ & \times (m'_l - 2\,\Delta x r'_l \hat{s}'_l)\,\mathrm{var}(r''_k, r'_l) + (m'_k - 2\,\Delta x r'_k \hat{s}'_k)(m''_l - 2\Delta x r''_l \hat{s}'_l)\,\mathrm{var}(r'_k, r''_l)\\ & \left. + (m''_k - 2\,\Delta x r''_k \hat{s}'_k)(m''_l - 2\,\Delta x r''_l \hat{s}'_l)\,\mathrm{var}(r''_k, r'_l)\right] / (\Delta x\,|r_k| \cdot |r_l|)^2 \end{aligned} \qquad \text{(D.4)}$$

and similar expressions for $\mathrm{var}(\hat{s}'_k, \hat{s}''_l)$ and $\mathrm{var}(\hat{s}''_k, \hat{s}''_l)$, where $r'_k = \mathrm{Re}(r_k)$, $r''_k = \mathrm{Im}(r_k)$, $s'_k = \mathrm{Re}(s_k)$, and $s''_k = \mathrm{Im}(s_k)$.

If the Fourier series $\hat{s}_k$ is truncated to $K(<N)$ terms, deleting all $\hat{s}_k$ for $k = K/2+1, \ldots, N-K/2$, the three $N \times N$ variance–covariance matrices of $\hat{s}_k$ are reduced to $K \times K$ matrices by deleting all elements with one of its indices $\in [K/2+1,\ N-K/2]$. If $\hat{s}''_{K/2}$ is set to zero, then $\mathrm{var}(\hat{s}'_k, \hat{s}''_{K/2}) = \mathrm{var}(\hat{s}''_{K/2}, \hat{s}'_l) = \mathrm{var}(\hat{s}''_k, \hat{s}''_{K/2}) = 0$.

If the inverse FFT of the truncated series $\hat{s}_k$ is written as:

$$\hat{S}_j = \frac{1}{N}\sum_{k=0}^{K-1}\left\{\hat{s}'_k \cos\left(\frac{jk2\pi}{K}\right) + \hat{s}''_k \sin\left(\frac{jk2\pi}{K}\right)\right\}$$

the variance–covariance matrix of $\hat{S}_j$ becomes:

$$\begin{aligned}\mathrm{var}(\hat{S}_j, \hat{S}_m) = {} & \frac{1}{N^2}\sum_{k=0}^{K-1}\left\{\mathrm{var}(\hat{s}'_k, \hat{s}'_l)\cos\left(\frac{jk2\pi}{K}\right)\cos\left(\frac{ml2\pi}{K}\right) + \mathrm{var}(\hat{s}'_k, \hat{s}''_l)\cos\left(\frac{jk2\pi}{K}\right)\sin\left(\frac{ml2\pi}{K}\right)\right.\\ & \left. + \mathrm{var}(\hat{s}''_k, \hat{s}'_l)\sin\left(\frac{jk2\pi}{K}\right)\cos\left(\frac{ml2\pi}{K}\right) + \mathrm{var}(\hat{s}''_k, \hat{s}''_l)\sin\left(\frac{jk2\pi}{K}\right)\sin\left(\frac{ml2\pi}{K}\right)\right\}. \end{aligned} \qquad \text{(D.5)}$$

This sum of four 2-dimensional real DFT's can be reduced to a single 2-dimensional complex DFT by

introducing the complex matrix $c_{kl} = c'_{kl} + \mathrm{i}c''_{kl}$ with

$$c'_{kl} = \mathrm{var}(\hat{s}'_k, \hat{s}'_l) - \mathrm{var}(\hat{s}''_k, \hat{s}''_l), \quad c''_{kl} = \mathrm{var}(\hat{s}'_k, \hat{s}''_l) + \mathrm{var}(\hat{s}''_k, \hat{s}'_l). \qquad \text{(D.6)}$$

Because the sine transform of an even function and the cosine transform of an uneven function are zero, it can be shown that:

$$\mathrm{var}(\hat{S}_j, \hat{S}_m) = \frac{1}{N^2}\sum_{k,l=0}^{K-1}\exp\left(-\frac{\mathrm{i}\,jk2\pi}{K}\right) c_{kl}\exp\left(-\frac{\mathrm{i}ml2\pi}{K}\right). \qquad \text{(D.7)}$$

References

[1] V.F. Turchin, V.P. Kozlov and M.S. Malkevich, Usp. Fiz. Nauk 13 (1971) 681, translated in Sov. Phys. Usp. 13 (1971) 681.

[2] B.R. Frieden, in: Topics in applied physics, ed. T.S. Huang (Springer, New York, 1975) p. 177.

[3] Y.G. Biraud, Rev. Phys. Appl. 11 (1976) 203.

[4] T.J. Kennett, W.V. Prestwich and A. Robertson, Nucl. Instr. and Meth. 151 (1978) 285, 293.
T.J. Kennett, P.M. Brewster, W.V. Prestwich and A. Robertson, Nucl. Instr. and Meth. 153 (1978) 125.

[5] J.T. Routti and J.V. Sandberg, Comput. Phys. Commun. 21 (1980) 119.

[6] E. Oran Brigham, The Fast Fourier Transform (Prentice-Hall, Englewood Cliffs, NJ, 1974).

[7] V.F. Turchin, Zh. Vychisl. Mat. Mat. Fiz. 7 (1967) 1270, 8 (1968) 230.

[8] B.R. Hunt, Los Alamos report LA-4515-MS (1970).

[9] J.D. Bregman and F.F.M. de Mul, Nucl. Instr. and Meth. 93 (1971) 109.

[10] F.F.M. de Mul and J.D. Bregman, Nucl. Instr. and Meth. 98 (1972) 53.

[11] A. Rotondi, Nucl. Instr. and Meth. 142 (1977) 499.

[12] U.P. Wild, A.R. Holzwarth and H.P. Good, Rev. Sci. Instr. 48 (1977) 1621.

[13] V. Cantoni, J. De Lotto and A. Ghirardi, Nucl. Instr. and Meth. 153 (1978) 199.

[14] H. Hühnermann and N. Menzel, Z. Naturf. 34a (1979) 399.

[15] B.R. Martin, *Statistics for physicists* (Academic Press, London, 1971).

[16] N.R. Draper and H. Smith, Applied regression analysis (Wiley, New York, 1966) p. 81.

[17] M.W. Johnson, Report RL-77-095/A, Rutherford Laboratory, Chilton, Didcot, Oxon, England (1977).

[18] F. Hossfeld, K. Mika and E. Plesser-Walk, Report Jül 1249, Institut für Festkörperforschung der Kernforschungsanlage Jülich GmbH, Jülich (1975).

[19] I. Beniaminy and M. Deutsch, Comput. Phys. Commun. 21 (1980) 271.

[20] H. Fredrikze and P. Verkerk, Comput. Phys. Commun. 24 (1981) 5.

[21] T.I. Seidman, J. Optimiz. Theor. Appl. 30 (1980) 535.

DICHTHEIDS- EN TEMPERATUUR-AFHANKELIJKHEID VAN DE STATISCHE EN DE DYNAMISCHE STRUCTUURFACTOR IN VLOEIBAAR ARGON GEMETEN MET THERMISCHE NEUTRONENVERSTROOIING

Samenvatting

Dit proefschrift beschrijft een experiment om de dynamische structuurfactor in een vloeistof bij drie dichtheden langs een isotherm te bepalen. De structuurfactor is de Fourier-getransformeerde van de twee-deeltjes correlatiefunctie, die informatie bevat over de structuur en de dynamica op atomaire schaal. Het experiment is uitgevoerd bij de Hoger Onderwijs Reactor van het Interuniversitair Reactor Instituut te Delft met behulp van thermische neutronenverstrooiing. Het preparaat bestond uit vloeibaar argon (^{36}Ar) bij 120 K onder een druk van achtereenvolgens 20, 270 en 844 bar, waarbij de dichtheden respectievelijk 17.6, 19.5 en 21.6 atomen/nm^3 zijn. De temperatuur-afhankelijkheid langs een isochoor kon bepaald worden uit een vergelijking van de resultaten voor 844 bar met de resultaten van Sköld et al.(1972) [3] voor argon bij het tripelpunt (85.2 K en 21.2 atomen/nm^3).

De uitwerking van de meetgegevens van een neutronen-experiment als hier beschreven vereist dat aanzienlijke correcties op de data worden toegepast en het is daarom dat een belangrijk gedeelte van dit proefschrift aan deze correcties is gewijd. Verder wordt op basis van de verkregen resultaten aandacht besteed aan de dispersie van geluidsgolven met een golflengte van de orde van de atoomdiameter, aan de drie-deeltjes correlatiefunctie, die gerelateerd is aan de dichtheidsafgeleide van de structuurfactor, en aan de invloed van de vorm van de potentiaal op de atomaire dynamica.

Een deel van het proefschrift bestaat uit drie reeds gepubliceerde artikelen (verder aangeduid met I, II en III). Na de inleiding in hoofdstuk 1 volgt een samenvatting van de theorie, waarop de interpretatie van de metingen is gebaseerd. In hoofdstuk 3 worden de spectrometer, het preparaat en de metingen beschreven. De in het experiment gebruikte preparaathouder wordt in artikel I beschreven.

Hoofdstuk 4 laat zien hoe groot de diverse correcties zijn en geeft schattingen van de nauwkeurigheid waarmee deze uitgevoerd konden worden. De wijze waarop de correcties worden uitgevoerd wordt uitvoerig in artikel II behandeld, terwijl artikel III een beschrijving geeft van de methode, die hier is toegepast om de experimentele data voor resolutie te corrigeren.

Hoofdstuk 5 geeft de volledig gecorrigeerde resultaten voor de dynamische structuurfactor. Ook de statische structuurfactor, die wordt verkregen door de dynamische structuurfactor over de frequentie-variabele te integreren, wordt gegeven. Op grond van voorlopige resultaten verkregen uit de hier beschreven metingen, is het experiment voortgezet bij de Hoge Flux Reactor van

het Institut Laue-Langevin (ILL) te Grenoble. Deze tweede serie metingen, die nauwkeuriger zijn door de hoge neutronenflux en waarop dezelfde correctie-procedure is toegepast, overlapt in een beperkt gebied de Delftse metingen. Uit de consistentie van de twee experimenten blijkt hoe betrouwbaar de volledig gecorrigeerde data zijn. Het experiment in het ILL wordt elders beschreven. De Delfste meting bij 844 bar valt buiten het gebied van overlap met de metingen in het ILL en in het vervolg van dit proefschrift wordt alleen de meting bij 844 bar verder geanalyseerd en gecombineerd met de vier ILL-metingen bij 120 K en 20, 115, 270 en 400 bar om de dichtheidsafhankelijkheid te bepalen.

In hoofdstuk 6 wordt de dynamische structuurfactor bij 844 bar geanalyseerd met behulp van drie modellen. Een opmerkelijk resultaat is dat er bij deze hoge dichtheid geen aanwijzingen gevonden worden voor het optreden van overgedempte geluidsgolven, hetgeen wel werd waargenomen in de ILL-metingen bij lagere dichtheden en bij een golflengte van ongeveer één atoomdiameter.

De dichtheids- en temperatuur-afhankelijkheid van de dynamische zowel als de statische structuurfactor worden bestudeerd in hoofdstuk 7. Enkele eenvoudige benaderingen voor de tijdsonafhankelijke drie-deeltjes correlatiefunctie worden getoetst en verworpen. De dichtheidsafgeleide van de dynamische structuurfactor stemt kwalitatief overeen met eerder gepubliceerde berekeningen op grond van een kinetische theorie van Groome et al. [46]. De temperatuurafhankelijkheid kan grotendeels beschreven worden met een schaling van de tijdsvariabele met de wortel uit de temperatuur, gebaseerd op de lineaire temperatuurafhankelijkheid van de gemiddelde kinetische energie der atomen. Een vergelijking met computer-simulaties bevestigt de aanname, dat de aantrekkende krachten tussen de atomen bij hogere temperatuur een kleinere rol spelen.

Hoofdstuk 8 bevat enige conclusies en suggesties voor toekomstig onderzoek.

Curriculum vitae

Na het behalen van het diploma gymnasium β aan het Cartesius lyceum te Amsterdam begon ik in 1961 de studie natuurkunde aan de Universiteit van Amsterdam. Na een onderbreking van enkele jaren, waarin ik o.a. mijn militaire dienstplicht vervulde, legde ik het kandidaatsexamen in 1968 af en studeerde ik in 1971 af in de experimentele natuurkunde. Voor het doctoraalexamen heb ik twee jaar in het Van der Waals-laboratorium onder leiding van prof.N.J.Trappeniers en dr.J.H.Kuyt gewerkt aan het meten van de levensduur van ladingsdragers in halfgeleiders. Sinds 1971 ben ik werkzaam in het IRI bij prof.J.J.van Loef en prof.L.A.de Graaf in de vakgroep Stralingsfysica, onderzoekgroep Molecuulfysica, waar ik o.a. aan de onderwerpen beschreven in dit proefschrift heb gewerkt.

P.Verkerk

Stellingen bij het proefschrift van P.Verkerk

1. Om de aanwezigheid van "Mode-Coupling" effecten in een gas of vloeistof met behulp van incoherente neutronenverstrooiïng te verifiëren, is het noodzakelijk dat de zelfdiffusiecoefficient in een onafhankelijk experiment wordt bepaald.
P.Verkerk, J.H.Builtjes and I.M.de Schepper, Phys.Rev.A (in druk).

2. De toename van de neutronenflux in bundels voor neutronenverstrooïngsexperimenten bij geavanceerde bronnen zoals de Spallation Neutron Source in Groot-Brittannië biedt de mogelijkheid om de nauwkeurigheid van de huidige experimentele data voor de dynamische structuurfactor in vloeistoffen verder te vergroten. Daartoe zou niet de statistiek van de meting verder verbeterd moeten worden, maar zou men het experiment zo moeten inrichten, dat op de meetgegevens toe te passen correcties aanzienlijk kleiner zijn dan nu meestal het geval is.

3. Een nauwkeurige bepaling van de asymmetrie van de Brillouin lijnen in lichtverstrooïngsexperimenten aan atomaire vloeistoffen zou de interpretatie van neutronenverstrooïngsspectra als een triplet kunnen ondersteunen.
V.Ghaem-Maghami and A.D.May, Phys.Rev.A **22** (1980) 698;
L.Letamendia, J.P.Chabrat, G.Nouchi, J.Rouch, C.Vaucamps and S.-H.Chen, Phys.Rev.A **24** (1981) 1574;
I.M.de Schepper, P.Verkerk, A.A.van Well and L.A.de Graaf, Phys.Rev.Lett. **50** (1983) 974.

4. Om de betrouwbaarheid te bepalen van een steekproefgemiddelde als schatting van het gemiddelde van een populatie met onbekende verdeling en variantie wordt door een aantal auteurs de steekproef verdeeld in een aantal kleinere steekproeven, waarvan de gemiddelden en hun spreiding worden gebruikt. Deze methode leidt tot onnodig onnauwkeurige resultaten.
G.Goertzel and M.H.Kalos in: Progress in Nuclear Energy, Series I, vol.2, editors D.J.Hughes, J.E. Sanders and J.Horowitz (Pergamon, London, 1958) p.315;
F.G.Bischoff, Thesis (Rensselaer Polytechnic, 1970);
J.R.D.Copley, Comput.Phys.Commun. **7** (1974) 289.

5. In veel gevallen wordt de waarde van kleinste-kwadraten aanpassingen van modellen

aan Mössbauer spectra overschat en worden de conclusies daarom twijfelachtig.
S.Gübbels, Q.Wu, J.Ladriere, F.Delannay and B.Delmon, Bull.Soc.Chim.Belg. **93** (1984);
H.Onodera, Y.Yamaguchi, H.Yamamoto, M.Sagawa, Y.Matsuura and H.Yamamoto, J.Magn.Magn.Mat. **46** (1984) 151;
H.M.van Noort, D.B.de Mooij and K.H.J.Buschow, J.Appl.Phys. (in druk).

6. De visco-elastische theorie, die Lovesey toepast om dichtheidsfluctuaties in vloeistoffen te beschrijven, is mede gebaseerd op een verkeerd argument, terwijl de benaming visco-elastisch verwarrend is.
N.K.Ailawadi, A.Rahman and R.Zwanzig, Phys.Rev.A **4** (1971) 1616;
S.W.Lovesey, Z.Phys.B **58** (1985) 79.

7. Met de nu beschikbare technieken is het niet mogelijk om het vierde moment van de dynamische structuurfactor in vloeistoffen zo nauwkeurig te meten, dat Rahman's methode om de effectieve paarpotentiaal te bepalen tot zinvolle resultaten leidt.
A.Rahman, Phys.Rev.A **11** (1975) 2191;
N.K.Ailawadi, Phys.Rep. **57** (1980) 241.

8. Bij het bepalen van de statische structuurfactor in gassen of vloeistoffen met behulp van neutronenverstrooiing biedt de multi-detector vliegtijdspectrometer een aantal voordelen boven de diffractometer.

9. De meest effectieve ontwikkelingshulp bestaat uit het afbreken van de tariefbarrieres voor producten uit de ontwikkelingslanden en uit het stimuleren van winstgerichte activiteiten in die landen.

10. De muzikale kwaliteiten van Mozart's clarinetkwintet of clarinetconcert komen het meest tot hun recht wanneer deze op een moderne clarinet ten gehore worden gebracht.